

Microstructural and textural analysis of naturally deformed granulites in the Mount Hay block of central Australia: Implications for the rheology of polyphase lower crustal materials

Author: Lauren Shea

Persistent link: <http://hdl.handle.net/2345/bc-ir:108578>

This work is posted on [eScholarship@BC](#),
Boston College University Libraries.

Boston College Electronic Thesis or Dissertation, 2019

Copyright is held by the author, with all rights reserved, unless otherwise noted.

Microstructural and textural analysis of naturally deformed granulites in the Mount Hay block of central Australia: implications for the rheology of polyphase lower crustal materials

Lauren Shea

A thesis

submitted to the Faculty of

the department of Earth and Environmental Sciences

in partial fulfillment

of the requirements for the degree of

Master of Science

Boston College
Morrissey College of Arts and Sciences
Graduate School

August 2019

Microstructural and textural analysis of naturally deformed granulites in the Mount Hay block of central Australia: implications for the rheology of polyphase lower crustal materials

Lauren Shea

Advisor: Professor Seth C. Kruckenberg

Abstract

Quantitatively describing the deformational behavior (i.e. the rheology) of lower crustal materials has proven challenging due to the highly variable nature of structural and compositional fabrics in the lower crust. Further, many flow laws describing the rheology of monophase aggregates are experimentally derived and do not necessarily apply to polyphase materials, such as gabbro, that dominate the lower crust. Here, we present the results of integrated microstructural analysis and electron backscatter diffraction (EBSD) textural analysis from exhumed lower crustal granulites in the Mount Hay block of central Australia. The preservation of heterogeneous mafic and felsic granulites containing monophase and/or polyphase mixtures of anorthite, pyroxene, and quartz (interlayered on the mm- to m-scale) make this region uniquely suited for advancing our knowledge of the processes that affect deformation and the rheology of the lower crust.

Forty-two samples from distinct structural and compositional domains were chosen to compare the microstructural record of deformation, the development of crystallographic textures, and to provide estimates of lower crustal rheology and deformation conditions. Full thin-section maps of crystallographic texture were produced using EBSD methods. The resultant orientation maps were processed to characterize crystallographic textures in all constituent phases, and all other quantifiable aspects of the

rock microstructure (e.g., grain size, grain shape, misorientation axes). The EBSD analysis reveals the presence of strong crystallographic preferred orientations (CPO) in nearly all constituent phases, suggesting deformation dominated by dislocation creep. Differential stresses during deformation are calculated using grain size piezometry for all major phases, and range between 34-54 MPa in quartz within monophase layers. Two-pyroxene geothermometry was used to constrain deformation temperatures to ca. 780-810 °C. Based on the estimated CPO patterns, stress, and temperature, we quantify strain rates and effective viscosities of all major phases through application of monophase flow laws. Monophase strain rates range from $2.10 \times 10^{-12} \text{ s}^{-1}$ to $1.56 \times 10^{-11} \text{ s}^{-1}$ for quartz, $4.68 \times 10^{-15} \text{ s}^{-1}$ to $2.48 \times 10^{-13} \text{ s}^{-1}$ for plagioclase feldspar, $1.56 \times 10^{-18} \text{ s}^{-1}$ to $1.64 \times 10^{-16} \text{ s}^{-1}$ for enstatite, and $5.66 \times 10^{-16} \text{ s}^{-1}$ to $1.00 \times 10^{-14} \text{ s}^{-1}$ for diopside. The determined flow law variables used for monophase calculations were subsequently applied to two different models – the Minimized Power Geometric model of *Huet et al.* (2014) and the Asymptotic Expansion Homogenization (AEH) method of *Cook* (2006) – in order to calculate a bulk aggregate viscosity of the polyphase material. At a strain rate of 10^{-14} s^{-1} , polyphase effective viscosities for our samples range from 3.07×10^{20} to $2.74 \times 10^{21} \text{ Pa}\cdot\text{s}$. We find that the bulk viscosity of heterogeneous, gabbroic lower crust in the Mount Hay region lies between that of monophase plagioclase and monophase quartz, and varies as a function of composition. These results are consistent with past modeling studies and geophysical estimates.

TABLE OF CONTENTS

Table of Contents.....	iv
List of Figures.....	v
List of Tables.....	vi
List of Appendices.....	vii
Acknowledgments.....	viii
Preface to the Thesis	x
1. Introduction.....	1
2. Geological Setting.....	5
3. Quantifying Polyphase Rheology.....	7
4. Materials and Methods.....	9
4.1 Electron Backscatter Diffraction Analysis.....	9
4.2 Electron Microprobe Analysis.....	12
5. Results.....	12
5.1 Microstructures.....	12
5.2 Grain Size Analysis and Paleostress Calculations.....	13
5.2.1 Quartz.....	14
5.2.2 Plagioclase.....	14
5.2.3 Enstatite.....	15
5.2.4 Diopside.....	15
5.3 Textural Analysis.....	15
5.3.1 Quartz.....	16
5.3.2 Plagioclase.....	17
5.3.3 Enstatite.....	17
5.3.4 Diopside.....	18
5.4 Compositional Analysis and Geothermometry.....	18
6. Discussion.....	19
6.1 Textural Analysis.....	20
6.2 Monophase Flow Laws.....	20
6.3 Polyphase Mixing.....	23
6.4 Power-Law Creep Polyphase Rheology.....	24
6.5 Implications for Lower Crustal Rheology.....	25
7. Conclusions.....	27
References.....	29
Figures.....	34
Tables.....	43
Appendices.....	49

LIST OF FIGURES

Figure 1. Location Map of and Field Photos of the Mount Hay Region.....	34
Figure 2. Select Electron Backscatter Diffraction (EBSD) Texture Maps.....	35
Figure 3. Select EBSD Phase Maps.....	36
Figure 4. Grain Size Distributions of Major Phases.....	37
Figure 5. Crystallographic Preferred Orientations (CPOs) of Major Phases.....	38
Figure 6. Plots of Polyphase Rheology Results.....	41

LIST OF TABLES

Table 1. Flow Law Variables Used for Rheology Calculations.....	43
Table 2. Equivalent Diameter and Differential Stress for Each Major Phase.....	44
Table 3. Average Equilibrium Temperatures in °C Calculated from 2-Pyroxene Geothermometry.....	45
Table 4. Monophase Strain Rates and Effective Viscosities for Each Major Phase.....	46
Table 5. Polyphase Effective Viscosities for Every Sample from $\dot{\epsilon}=10^{-18}$ - 10^{-10} s ⁻¹	47
Table 6. Polyphase Effective Viscosities for Select Sample from $\dot{\epsilon}=10^{-18}$ - 10^{-10} s ⁻¹	48

LIST OF APPENDICES

Appendix A. Sample Localities.....	49
Appendix B. Analytical Methods.....	51
1. Electron Backscatter Diffraction Collection and Processing.....	52
2. Electron Microprobe Collection and Processing.....	55
3. Huet et al. Mixing Model Rheology Calculations.....	56
4. Power-Law Creep Toolbox Rheology Calculations.....	57
Appendix C. Electron Backscatter Diffraction Maps.....	59
Appendix D. Average Grain Size Histograms.....	102
Appendix E. Crystallographic Preferred Orientations and Misorientation Axes.....	119
Appendix F. Electron Microprobe Raw Data and Temperatures.....	132
Appendix G. Polyphase Rheology Graphs Calculated through the Mixing Model.....	137
Appendix H. Polyphase Rheology Graphs Generated through the PLC Toolbox.....	141

ACKNOWLEDGMENTS

I would like to give a huge thank you to my advisor, Dr. Seth Kruckenberg, for his constant support and encouragement, and for always being more than willing to make time to answer questions and to help out. Thanks for providing me with countless opportunities to improve my analytical skills, teaching skills, and presentation skills, and also for allowing me to grow as a researcher. Thank you for your enthusiasm about doing research and for making it so fun, but also for always supporting taking breaks and enjoying life outside of the office. I couldn't imagine a better advisor to work with.

I'd also like to thank my committee members Mark Behn and Ethan Baxter for taking the time out of their schedules to be on my committee and to meet with me to discuss my project. Their feedback and distinct areas of expertise has made me more aware of ways to improve my study by making it more robust and has helped me become a better scientist.

Thank you to Gail Kineke for being a constant source of support and inspiration throughout my time at Boston College, and additionally for teaching me proper scientific formatting for papers and presentations during my first semester at graduate school. I wouldn't be able to effectively communicate my science without you.

Thanks to my fellow graduate students for always being willing to write on the board to work through problems together, for providing constructive criticism when I

needed it, for their collective efforts to make this department the best that it can be, and for laughing through graduate school with me.

I'd like to also thank my undergraduate professors for providing me with a strong foundation of geologic knowledge — namely Dr. Gordana Garapic, the person who ignited my interest in mineralogy and in doing microstructural research, and who continues to visit my presentations and support me today, and Dr. Fredrick Vollmer, the person who consistently encouraged me to continue my education.

Thank you to my parents for all of the opportunities they have provided me with, for emphasizing the importance of school, for always supporting my decisions, and for not laughing at me (too much) for wanting to look at rocks for the rest of my life.

This research wouldn't be possible without the generous support from the National Science Foundation (NSF) grant EAR-1808117 to Kruckenberg. Support from the Geological Society of America (GSA) graduate student research grant program is also greatly acknowledged. William Shinevar (MIT/WHOI) and Mark Behn (Boston College) are credited for writing and providing the mixing script used for polyphase viscosity calculations, based on Huet et al. (2014). Additional thanks to Prof. Basil Tikoff, Max Heckenberg, and the rest of the staff at the Northern Territory Geological Survey (NTGS) for field support. I'd also like to thank the various landowners of the Amburla, Hamilton Downs, Milton Park, and Narwietooma Stations in central Australia for making this work possible.

PREFACE TO THE THESIS

Understanding how deformation is distributed in the lower crust, and in particular being able to put quantitative constraints on the processes governing this deformation in a naturally deformed system, directly advances our understanding of the strength of the lower crust and its potential consequences to geodynamic processes that are governed by the strength of the lithosphere. The primary goal of this research is to unravel patterns of structural and compositional heterogeneity in the deep crust and to investigate the tectonic and microphysical processes that govern dynamic strain localization in the lower crust. This is done through quantification of the viscous flow laws for compositionally and structurally heterogeneous lower crustal materials. Extensive exposures of exhumed, naturally deformed deep crustal granulites located throughout in the Mount Hay block of central Australia provide a unique opportunity for advancing studies of lower crustal deformation due to the preservation of variably deformed, interlayered felsic and mafic granulites (mm- to m- scale) with abundant strain markers. These rocks are dominantly composed of varying percentages of plagioclase feldspar, quartz, and pyroxene. Because strain markers are typically rare in the lower crust, the presence of such markers in this region makes it uniquely suited to assess the patterns of compositional and structural heterogeneity in the lower crust.

The current configuration of the Australian continent was established through the suturing of three smaller cratons: the North Australian Craton, West Australian Craton, and the South Australian Craton. The cratons were formed through continued accretion of crustal fragments in the Paleoproterozoic, approximately 1860-1800 Ma (*Myers et al.*, 1996). These collisions formed the basis of the North Australian Craton, which continued as an active tectonic region along its southern border. The Arunta Block, currently located in central Australia, is located on the southern margin of the North Australian Craton and experienced prolonged tectonic activity during the Precambrian, when the Australian continent was being assembled (*Betts et al.*, 2016). Two of the earliest events indicating a transition from a passive tectonic margin to an active margin in the Arunta Block are the Yambah and Strangways orogenic events, dating from 1780-1770 Ma and 1740-1690 Ma, respectively. The lower crustal granulites investigated in this study were metamorphosed and deformed during these two orogenic events.

The shift to an active setting coincides with the Stafford Event, a pulse of magmatism from 1810-1790 Ma that produced large amounts of felsic magmatism and minor amounts of mafic magmatism (*Howlett et al.*, 2015). The Yambah Event, which occurred from 1790-1770 Ma, is characterized by bimodal magmatism (*Howlett et al.*, 2015) and associated low-pressure, high-temperature metamorphism. This event emplaced large volumes of granite and gabbro and produced amphibolite to granulite facies metamorphic rocks (*Waters-Tormey et al.*, 2016). The Yambah Event also produced a number of deformational fabrics associated with southwest-directed thrusting. Folds oriented in the N-S and NW-SE directions were developed in the late stages of the orogeny (*Betts and Giles* 2006) and a gneissic foliation was developed in the granulites

(*Lafrance et al.*, 1993). Most of the deformational features of the Yambah Event were subsequently overprinted by other orogenic events.

Based on their geochemical signatures, magmas from the Stafford Event and Yambah Event are reflective of an extensional back-arc regime (*Maidment et al.*, 2005; *Howlett et al.*, 2015), despite the fact that the overall tectonic environment associated with the Yambah Event does was compressional in nature (*Cawood and Korsch*, 2008). This shift from the extension, which produced magmas associated with the Stafford Event, to the more compressional setting of the Yambah Orogeny may have occurred due to a change in the geometry of the plate boundary, which also could have affected the stress regime in the backarc (*Cawood and Korsch*, 2008). It is possible that slab rollback during the Stafford Event led to the progressive subduction of younger oceanic crust (*Cawood and Korsch*, 2008); this configuration would have resulted in more buoyant crust that was more difficult to subduct, resulting in less slab rollback and thus more compression in the backarc during the Yambah Event than during the Stafford Event. The Yambah Event demonstrates that there was a north-dipping subduction zone along the southern margin of the North Australian Craton such that close to, or slightly south of, the southern margin was a magmatic arc and north of the margin was a backarc setting (*Howlett et al.*, 2015).

Following the Yambah Event was another large granitic magmatic event, known as the Tanami Event that occurred from 1760-1740 Ma and produced rocks with geochemical signatures similar to arc-type magmas in a continental margin subduction zone (*Maidment et al.*, 2005; *Betts and Giles*, 2006). Further, a sedimentary sequence, named the Ledan Package, was deposited between 1770-1730 Ma (*Maidment et al.*,

2005), which reflects basin formation (*Maidment et al.*, 2005) and illustrates a divide between the tectonic pulses of the Yambah Event and the Strangways event.

The Strangways Orogeny occurred from 1740-1690 Ma (*Betts and Giles*, 2006). The dominant lithologies within the Strangways Metamorphic Complex in the Mount Hay region of the Arunta Block are high-grade metamorphic granulites that have mafic and felsic igneous protoliths (*Waters-Tormey et al.*, 2016). Surrounding the complex are intermediate-grade metamorphic amphibolite facies, granites, and migmatites. Minor metasedimentary rocks are also present (*Claoue-Long et al.*, 2008). The granulites were most likely derived from the mafic and felsic bimodal magmatism of the Stafford Event (*Warren*, 1983). The main rock types present include gabbroic granulites, charnockites, anorthosite, and felsic segregations (*Claoue-Long et al.*, 2008), in addition to some garnet-bearing granitic granulites. On the meter-scale, the granulites are heterogeneous. Interlayered gneissic foliations are common and the rocks are uniformly fine-grained (*Lafrance et al.*, 1993). Plagioclase is the dominant phase but quartz and pyroxene are also abundant. Granulite facies metamorphism in these lower crustal rocks occurred under pressure and temperature conditions of approximately 8-9 kilobars and 800-900°C, respectively (*Waters-Tormey and Tikoff*, 2007).

The Strangways Metamorphic Complex trends SE and is fault-bound. The Strangways Orogeny can be broken up into two main structural domains: The Mount Hay Ridge sheath fold and the Capricorn Ridge shear zone. The Mount Hay Ridge sheath fold is greater than 8 km thick, records NE-SW subhorizontal shear (*Waters-Tormey et al.*, 2016), and is doubly plunging to the north and south (*Lafrance et al.*, 1993). Strain markers, such as stretched felsic segregation ‘blebs’, are present and illustrate both oblate

and prolate strains (*Bonamici et al.*, 2011). The Capricorn Ridge shear zone is greater than 6 km thick and has a 30-50° dip (*Waters-Tormey and Tikoff*, 2007). Extension shear bands and boudinage are present. Within the shear zone, the foliation fabrics are the strongest next to lithologic boundaries, suggesting that the largest strain localization is at those boundaries (*Waters-Tormey and Tikoff*, 2007). Structural fabrics switch directions between these two domains; lineations plunge NE in the Mount Hay Ridge sheath fold to SSE-SE in the Capricorn Ridge shear zone. Similarly, foliations dip NE in the sheath fold to SSW in the shear zone (*Waters-Tormey and Tikoff*, 2007). The Capricorn Ridge shear zone crosscuts the Mount Hay sheath fold (*Waters-Tormey and Tikoff*, 2007).

The thrust faults produced during the Strangways Orogeny are evident of a convergent tectonic setting in which the convergence was oblique (*Myers et al.*, 1996). The sheath folds are evidence of crustal thickening, shortening, and crustal flow (*Betts and Giles*, 2006). Its orientation records NE-SW subhorizontal shear (*Waters-Tormey et al.*, 2016). The sheath folds demonstrate both pure shear and simple shear components and provide evidence for a transpressional environment (*Bonamici et al.*, 2011). The Strangways Orogeny was a compressional event that occurred at the plate margin (*Maidment et al.*, 2005), suggesting that the plate boundary and subduction zone migrated south over time (*Betts and Giles*, 2006). The age of the Strangways Orogeny is bounded by a 50-million-year period over which high-grade metamorphic conditions persisted in the Strangways Metamorphic Complex (*Claoue-Long et al.*, 2008).

The assembly of the North Australian Craton through accretion of crustal fragments resulted in zones of crustal weakness (*Myers et al.*, 1996). Through continued tectonic activity, some of these weak zones reactivated, including the Redbank thrust

fault — a Mesoproterozoic suture that likely extended to the crust-mantle boundary (*Fishwick and Reading, 2008*). The reactivation of the Redbank thrust fault occurred during the Devonian-aged Alice Springs Orogeny, approximately 400-350 Ma, and resulted in the exhumation of the Strangways-formed lower crustal granulites (*Lafrance et al., 1993*).

The complex tectonic history of the Arunta block that allowed for the deformation and exhumation of structurally and compositionally heterogeneous, natural lower crustal rocks, makes this region uniquely suited to study the controls of different variables on the rheology of the lower crust and on the processes accommodating strain localization in lower crustal lithologies.

MICROSTRUCTURAL AND TEXTURAL ANALYSIS OF NATURALLY DEFORMED GRANULITES IN THE MOUNT HAY BLOCK OF CENTRAL AUSTRALIA: IMPLICATIONS FOR THE RHEOLOGY OF POLYPHASE LOWER CRUSTAL MATERIALS

1. Introduction

The rheology of the lithosphere influences all aspects of the plate tectonic system. For example, numerous studies have shown the effects of lithospheric and mantle viscosity structure on patterns of isostatic rebound and sea level rise (*Wdowinski and Axen, 1992; Lambeck et al., 1998; Beaumont et al., 2001*). As such, accurately predicting the societal effects of global and local sea level change is, in part, dependent upon our understanding of the conditions and microphysical processes that control the viscous rheologies of materials in the lithosphere. Moreover, the rheology of the lower crust is an important variable in models that predict stress loading in the crust, the spatial and temporal scales of post-seismic deformation, and zones of increased seismic risk (*Hetzel and Hampel, 2005*). The extent of structural and compositional heterogeneity in the lower crust, and the processes that affect deformation partitioning, are still poorly constrained. Thus, our ability to quantify the processes governing the deformation of materials comprising the lithosphere remains central to advancing our understanding of a range of interconnected geodynamic processes.

To the first order, the continental lithosphere can be divided into three distinct rheological layers. The shallowest is the upper crust wherein deformation is described by Byerlee's law of brittle, pressure-dependent deformation, defining the seismogenic zone. This rheologic layer extends to the brittle-ductile transition in the mid-crust. Below this transition, deformation is predominately governed by the temperature-dependent strength of materials (typically quartz and feldspar) resulting in ductile (viscous) deformation in the mid- to- lower crust, which follows an Arrhenius relationship. The strength of the lowermost lithosphere is governed by the rheology of olivine-dominated upper mantle materials (*Ord and Hobbs, 1989; Hirth and Kohlstedt, 1996; Burgmann and Dresen, 2008*).

This first order description of the rheology of the lithosphere has been useful for describing many aspects of lithospheric deformation. However, the relative strength of each of these three layers is still debated and many models have been proposed to describe the rheological layering of the lithosphere (e.g., "Jelly Sandwich" versus "Crème Brulee" cf. *Burgmann and Dresen, 2008*; and references therein). To complicate matters further, a number of extrinsic and intrinsic variables are known to affect rock deformation, including temperature, pressure, differential stress, water content, chemical composition, and crystal structure, all of which undoubtedly give rise to a more complex, and transient, lithospheric strength profile in natural systems.

Another barrier in understanding the deformational behavior of the lower crust lies in the fact that rocks from these crustal depths are rarely exhumed to the surface without subsequent tectonic overprinting, commonly obscuring structural and compositional fabrics that formed in the deep crust. A quantitative description of lower

crustal rheology, therefore, relies on the extrapolation of rock deformation experiments to geologically relevant conditions of temperature, pressure, water fugacity, and, notably, stress and strain rate. However, these experimental studies cannot account for the heterogeneity and structural complexity of the natural Earth system. For example, many of the flow laws that have been derived in the laboratory have focused on monophase aggregates of quartz, plagioclase, pyroxene, or olivine (e.g., *Hirth et al.*, 2001; *Rybacki and Dresen*, 2000; *Lawlis*, 1998, *Hansen et al.*, 2011) as these materials are thought to dominate the deformational behavior of the upper and lower crust and mantle, respectively.

The rheology of the lower crust – the focus of this study – is commonly modeled using the flow law behavior of plagioclase feldspar. Experimental models of monophase plagioclase deformation match predictions of flow laws for geologically relevant conditions of strain rate (*Stunitz et al.*, 2003). However, this rheological description of the lower crust represents a significant oversimplification of the mineralogy and deformational behavior of the polyphase materials that dominate the lower crust, such as gabbroic rocks composed of plagioclase, orthopyroxene, and clinopyroxene in varying abundance. Experimental rock deformation studies have attempted to overcome this limitation by quantifying the flow law behavior of some polyphase aggregates, such as anorthite and diopside (*Dimanov and Dresen*, 2005). Other studies have used a complementary approach that leverages thermodynamic modeling to predict equilibrium mineral assemblages appropriate for the lower crust based on its composition, pressure, and temperature. These mineral assemblages are then used calculate the aggregate viscosity of the lower crust through mixing models that integrate the respective

(monophase) flow laws of constituent minerals (*Shinevar et al.*, 2015; 2018). These models, however, are intended for a homogeneous distribution of phases and thus do not account for the fabric development that occurs in naturally deformed lower crustal rocks. Additionally, other studies focusing on naturally-deformed systems suggest that strain rates may still be underestimated in polyphase rocks based on the observed deformation mechanisms and microstructures preserved in these polyphase lithologies (*Cross et al.*, 2017).

The complex mineral distribution in the lower crust also influences how strain is accommodated and distributed. In this regard, gabbroic rocks situated in the lower crust and exposed to the same external conditions may differ in strength based on their mineralogy, such as their relative percentage of minerals like plagioclase feldspar, quartz, and pyroxene. In summary, how deformation is distributed in the lower crust, what factors affect it, and the processes that result in strain localization are still not fully understood. This indicates the need to increase our understanding of lower crustal rheology on the basis of natural compositional heterogeneity, which can be done through calculations of strain rates and effective viscosities in exhumed, naturally deformed lower crustal materials.

Highly deformed lower crustal granulites exposed on Ceilidh Hill, central Australia, provide an excellent opportunity for furthering our understanding of natural lower crustal rheology on the basis of compositional and structural heterogeneity, as they show a range of mineral assemblages and contain abundant strain markers. In the sections that follow, we develop a methodology that leverages the unique rock record exposed on Ceilidh Hill to provide new constraints on the rheology of polyphase lower crustal

material. Integrated microstructural and EBSD textural analyses are used to quantify all aspects of the rock microstructure and the deformation conditions, such as differential stress, temperature, and deformation mechanisms in all mineral assemblages, providing a more complete description of the variables affecting rheology. These are subsequently applied to known flow laws and proposed mixing equations in order to assess the rheology of naturally deformed, polyphase lower crustal rocks in terms of strain rate and effective viscosity.

2. Geological Setting

The Mount Hay block, which comprises Mount Hay ridge, Capricorn Ridge, Ceilidh Hill, and Hamilton Downs (e.g., Glikson, 1984; Watt, 1992; Hoatson and Stewart, 2001; Meixner and Hoatson, 2003; Waters-Tormey and Tikoff, 2007; Waters-Tormey et al., 2009; Bonamici et al., 2011), is a granulite massif that outcrops in the Arunta Region of central Australia (Fig. 1a-b). It is located just north of the crustal-scale Redbank Thrust Zone (Shaw et al., 1984; Stewart et al., 1984) and represents a slice of the deep crust that was rotated and exhumed to the surface when the Redbank Thrust Fault was reactivated during the Devonian Alice Springs Orogeny (Bonamici et al., 2011). Previous work concluded that these rocks were buried at approximately 25-30 km depth (*Waters-Tormey et al.*, 2009), based on geothermobarometric analyses constraining the deformation temperature and pressure conditions to 700-900°C and 700-800 MPa, respectively (*Collins and Shaw*, 1994; *Staffier*, 2007). Rocks belonging to the Mount Hay block were originally emplaced during the Stafford Event from 1810-1790 Ma, which produced bimodal mafic and felsic magmatism (*Warren*, 1983; *Waters-Tormey et al.*,

2016). They were later metamorphosed to granulite-facies conditions during the Proterozoic Yambah and Strangways orogenies, which occurred from 1780-1770 Ma and 1740-1690 Ma, respectively (*Hoatson et al., 2005, Betts and Giles, 2006; Howlett et al., 2015*).

The lower crustal rocks exposed on Ceilidh Hill offer a unique opportunity to constrain the rheology of naturally deformed lower crustal materials as this region contains compositionally and structurally heterogeneous mafic and felsic granulites interlayered on the mm- to m- scale (Fig 1c-d). The main lithological units include metamorphosed gabbro, charnockite, and anorthosite (*Bonamici et al., 2011*), all of which contain varying modal percentages of plagioclase feldspar, enstatite, diopside, \pm quartz, \pm potassium feldspar. Quartz typically occurs in segregated monophase layers within felsic ribbons, as interconnected compositional bands within charnockite layers, or as minor isolated compositional domains within gabbro layers. Feldspar and pyroxene are typically interspersed, forming relatively uniform (i.e., isotropic) polyphase domains in both charnockite and gabbro layers. This preserved compositional heterogeneity allows us to explore the compositional control on lower crustal rheology with respect to specific conditions of deformation.

Rocks in this region also preserve a highly variable record of deformation expressed by variations in the mesoscopic structural fabric (e.g., $S \gg L$, $S=L$, and L -tectonites are present, based on the relative foliation and lineation intensity) and patterns of finite strain as evident from deformed ellipsoids of quartz and feldspar aggregates contained within gabbroic granulites (*Bonamici et al., 2011*). These fabrics define large-

scale sheath folds adjacent to a network of shear zones, implying high shear strains (Tikoff *et al.*, 2001) (Fig. 1d).

3. Quantifying Polyphase Rheology

For a non-Newtonian fluid undergoing viscous deformation, such as for the lower continental crust, there exists a power-law relationship between strain rate, viscosity, and differential stress:

$$\dot{\epsilon} = \eta \sigma^n \text{ (eq. (1))}$$

where $\dot{\epsilon}$ is the strain rate, η is the effective viscosity, σ is the differential stress, n is the stress exponent, and the stress to strain rate ratio is dependent on the active deformation mechanism in the rock, which influences the n term. More generally, the steady state stress and strain rate relationship for viscous deformation is represented by a flow law with the Arrhenius form:

$$\dot{\epsilon} = A \sigma^n d^{-m} f_{H_2O}^r \exp(-Q/RT) \text{ (eq. (2))}$$

where d is the grain size, m is the grain size exponent, f_{H_2O} is water fugacity, Q is the activation enthalpy, R is the gas constant, T is temperature, and A is an empirically derived pre-exponential constant. (Burgmann and Dresen, 2008; Rybacki and Dresen, 2004; Hirth *et al.*, 2001). This equation is appropriate to describe many aspects of lithospheric deformation and experimental rock deformation studies have quantified the flow law behavior of many minerals under changing deformation conditions (Hirth and Kohlstedt, 1996; Gomez-Barreiro *et al.*, 2007; Farla *et al.*, 2013; Getsinger *et al.*, 2013; Cross *et al.*, 2017). Laboratory experiments are designed to mimic natural pressure and temperature conditions so that they can, in theory, be extrapolated to natural settings.

Amongst the abundant lower crustal mineral phases, constitutive equations of minerals undergoing viscous deformation via dislocation creep have been formulated for monophase aggregates of quartz (*Hirth et al.*, 2001), plagioclase feldspar (*Rybacki and Dresen*, 2004), orthopyroxene (enstatite) (*Lawlis*, 1998; *Bruijn and Skemer*, 2014; *Bystricky et al.*, 2016), and clinopyroxene (diopside) (*Raterron and Jaoul*, 1991) (Table 1), as well as olivine (*Hirth & Kohlstedt*, 2003) for the mantle.

One method of converting effective viscosities calculated from individual monophase flow laws into a polyphase aggregate effective viscosity for the bulk rock sample is through mixing equations. The Minimized Power Geometric mixing model from *Huet et al.* (2014) uses monophase effective viscosities and the modal percent of each mineral phase as inputs through an equation in the form:

$$\eta_{aggregate} = \sum_i \frac{\phi_i n_i}{n_i + 1} \prod_i \left(\eta_i \frac{n_i + 1}{n_i} \right)^{\frac{\phi_i a_i n_i}{\sum_i \phi_j a_j n_j}} \quad (\text{eq. (3)})$$

where η_i , ϕ_i , and n_i are the effective viscosity, volume percentage, and stress exponent of phase i , respectively, and a_i for each phase is defined as $\prod_j (n_j + 1)$, where phase j does not equal phase i .

An alternative method for converting monophase flow laws into polyphase bulk aggregate behavior is through the Asymptotic Expansion Homogenization (AEH) and Finite Mesh (FE) methods (*Cook*, 2016), which account for the heterogeneity of the material. This model requires knowledge of the temperature, stress exponent, activation energy, and pre-exponential constant of each major phase (Equation 2), as well as the modal percentage of each phase and the phase distribution. The Power-Law Creep GUI toolbox developed by *Cook* (2016) applies the AEH and FE methods to polyphase

samples and we use this as a second way to calculate effective viscosities of our naturally deformed lower crustal samples.

Variables A , n , m , and Q in the viscous flow law (Equation 2) are highly dependent on the dominant deformation mechanism that is active in the lower crust, specifically if the material is deforming by grain size-sensitive diffusion creep or grain size-insensitive dislocation creep. Knowledge of active deformation mechanisms can be determined through textural analysis, such as by using electron backscatter diffraction (EBSD) to investigate the crystallographic preferred orientations (CPO) of each major phase. Experimentally derived flow law variables used in this study were chosen based on analysis of the rock microstructure.

4. Materials and Methods

Forty-two samples of varying modal compositions were collected throughout the Ceilidh Hill region of the Mount Hay block to compare the microstructural record of deformation in distinct structural and compositional domains. Thin sections were cut perpendicular to the macroscopic foliation and parallel to lineation in samples with varying structural fabrics (e.g., S- versus L-tectonites). In all samples, major phases include plagioclase feldspar, quartz, enstatite, diopside, +/- potassium feldspar, corresponding to samples of gabbroic to charnockitic composition.

4.1 Electron Backscatter Diffraction Analysis

Electron backscatter diffraction was used to provide quantitative constraints on a number of important properties resulting from deformation, including patterns of

crystallographic preferred orientation, mineral mode, grain shape, grain size, and internal crystallographic misorientation.

Full thin-section maps of crystallographic texture in all constituent phases were acquired for all forty-two samples using a Tescan Mira3 variable-pressure field emission scanning electron microscope equipped with an Oxford Instruments Symmetry EBSD detector housed within the Department of Earth and Environmental Sciences at Boston College. Operating conditions for sample analysis utilized a beam current of 50 nA and an accelerating voltage of 25 kV. Textural maps were acquired using the Oxford Instruments AZtecHKL acquisition software (version 4.0) using a step size of 5 μm in order to produce high resolution data sets containing a large number of crystallographic orientations. (Fig. 2).

EBSD textural maps were processed using version 5.1.1 of the freely available MTEX toolbox for MATLAB. EBSD solutions with a mean angular deviation (MAD) > 0.8, nonindexed pixels, and single pixel grains without any common neighboring grains were omitted. Within the remaining dataset, grains were defined as any collection of solutions that have a misorientation angle greater than 10° relative to its neighbors. The grainsets produced with these criteria were further smoothed using a Voronoi decomposition grain reconstruction algorithm. Following the grain reconstruction, grains with diameters smaller than 3 times the step size (e.g., the minimum grain size is 15 μm for a step size of 5 μm) were removed to ensure accurate estimates of grain size statistics, and to not bias the determination of crystallographic fabrics due to the over-representation of grains defined by only a few pixels. Subgrains were then calculated

from the resultant reconstructed grain set for solutions with an average misorientation angle between 2° and 10° relative to neighboring pixels.

Crystallographic orientations for each major phase were calculated using processed grain sets by calculating the mean orientation of individual grains such that each grain in the dataset is defined by a single (mean) orientation (i.e., one point per grain). In order to correct for the fact that some crystallographic orientations are statistically favored over others, crystallographic preferred orientations were plotted as orientation distribution functions (ODFs), which recontour the data based on crystal symmetry (*Prior et al.*, 1999). The strength of the crystallographic preferred orientations within a sample is calculated using the M-index of Skemer et al. (2005). Assessment of CPO type was quantified using the BA-index (*Mainprice et al.*, 2014) – for example, in plagioclase a BA-index of 0 is indicative of B-type fabric, whereas a BA-index of 1 is indicative of axial-A fabric (*Satsukawa et al.*, 2013). Histograms of grain size distributions were plotted for all samples based on the equivalent-area grain size diameter to calculate a geometric mean of the grain size distribution for each major phase. A correction factor of 1.2 was applied to the mean grain in order to account for the inaccurate representation of assuming each grain was cut to show its maximum diameter, and as required by recrystallized grain size piezometers as we discuss in a subsequent section. Internal misorientation axes of grains were calculated as inverse pole figures within the crystal reference frame in order to assess patterns of intracrystalline distortion reflecting the activation of distinct crystallographic slip systems in minerals. Additional aspects of the EBSD method are described in Appendix B.

4.2 Electron Microprobe Analysis

Eight samples of gabbro from spatially distinct regions were selected for electron microprobe microanalysis. Compositional data were acquired using a Cameca SX50 housed in the Department of Geoscience at the University of Wisconsin-Madison at operating conditions of 20 nA for beam currents and an accelerating voltage of 15 kV. Compositional data were obtained for a minimum of nine distinct orthopyroxene-clinopyroxene pairs located in at least three different areas in each thin section. Three points per orthopyroxene grain and clinopyroxene grain per pair were analyzed. To ensure the pyroxene compositions analyzed were in textural equilibrium, the compositions of each pyroxene pair were measured near the edges of neighboring grains that were free of retrograde metamorphic textures, such as the presence of hornblende rims. At least six different areas of plagioclase in each thin section were also analyzed. Weight totals that were not between 98.5-101% were removed from further analytical characterization to avoid erroneous calculation of mineral compositions.

5. Results

5.1 Microstructures

Charnockite and gabbro samples taken from the same geographic location differ with respect to their constituent mineralogy. While both rock types record a similar range of plagioclase composition (20-51% and 20-56% for charnockite and gabbro, respectively), the charnockite samples are characterized by a greater modal abundance of quartz, whereas gabbro samples are dominated by enstatite and diopside (Fig. 2). The modal abundance of quartz in charnockite ranges from 13-47%. In gabbro samples,

quartz has a modal abundance of ca. 8-23%. Pyroxene is present in both charnockite and gabbro, with modal abundances ranging from ca. 6-26% to 8-36%, respectively.

In both charnockite and gabbro samples, quartz grains appear as ribbons of elongate, monophase aggregates, whereas plagioclase and pyroxene grains are interspersed within polyphase domains (Fig. 3). Grains in all samples show a moderate to strong shape-preferred orientation. In many of the samples, potassium feldspar is also present (Fig. 3d), in some cases showing exsolution textures with plagioclase. In other textural settings, potassium feldspar occurs as distinct crystals separate from plagioclase grains and without evidence of exsolution. Nearly all mineral phases and grains show evidence of extensive recrystallization, although a few samples also preserve large relict feldspar porphyroclasts (Fig. 3c-d). Grain boundaries between quartz are interlobate, indicating grain boundary migration (*Hirth and Tullis, 1992*). Phase boundaries between plagioclase and pyroxene are typically more polygonal, suggesting grain boundary area reduction of plagioclase during recrystallization (*Hirth and Tullis, 1992*).

Due to the high modal abundance of quartz in charnockite, quartz typically forms interconnected ribbons that persists as distinct compositional domains parallel to the foliation across and entire thin section (Fig. 3c). In contrast, quartz in gabbro layers form small, discontinuous felsic segregations in the dominantly plagioclase-pyroxene matrix, consistent with the low modal abundance of quartz discussed previously (Fig. 3b & 3d).

5.2 Grain Size Analysis and Paleostress Calculations

Empirically derived paleopiezometers that relate recrystallized grain size to the amount of differential stress that a material has experienced have been experimentally determined for many lithospheric minerals (*Twiss, 1977*), with the general formula:

$$d=K\sigma^p \text{ (eq. (4))}$$

where d is the crystallized grain size, σ is the differential stress, and K and p are constants that are calibrated for different minerals and different recrystallization mechanisms (*Stipp and Tullis, 2003*). To calculate the differential stress experienced by each major mineral, the mean recrystallized grain size was determined for each major phase (Table 2; Fig. 4) using MTEX, as described in Section 4.1. Most grain size distributions follow a log-normal pattern. However, some grain size distributions follow a bimodal arrangement, in which case we use the smaller grain size peak to calculate the differential stress of recrystallized grains. In doing so, we define the minimum stress that each sample must have experienced during the final stages of deformation.

5.2.1 Quartz

For quartz undergoing dislocation creep, as is consistent with the observed microstructures, differential stresses were determined using the recrystallized grain size piezometer for quartz from *Stipp and Tullis (2003)*:

$$d=10^{3.56\pm0.27}\sigma^{1.26\pm0.13} \text{ (eq. (5))}$$

where d is the recrystallized grain size in μm and σ is the differential stress in MPa. Mean quartz grain sizes range from 24.0 μm to 41.6 μm , corresponding to differential stresses of 53.8 MPa to 34.7 MPa, respectively.

5.2.2 Plagioclase

Plagioclase differential stresses were determined using the high temperature anorthite recrystallized grain size paleopiezometer of *Twiss (1977)*:

$$\sigma=7.8d^{0.68} \text{ (eq. (6))}$$

where d is the recrystallized grain size in mm and σ is the differential stress in MPa. Mean grain sizes determined for the plagioclase in our samples range from 22.4 μm to 59.8 μm , corresponding to differential stresses of 103.3 MPa to 53.0 MPa, respectively.

5.2.3 Enstatite

The differential stresses experienced by the enstatite in our samples was determined using the temperature-dependent, power-law grain size piezometer for orthopyroxene (Linckens *et al.*, 2014; Bruijn and Skemer, 2014);

$$\sigma = 2939^{+1673/-1066} d^{1.308 \pm 0.01} \text{ (eq. (7))}$$

where d is the recrystallized grain size in μm and σ is the differential stress in MPa. Mean equivalent diameters of enstatite grains range from 19.6 μm to 74.9 μm , corresponding to differential stresses of 60.0 MPa to 10.4 MPa, respectively.

5.2.4 Diopside

Average diopside grain sizes range from 15.4 to 48.7 microns. To the best of our knowledge, there is no diopside paleopiezometer currently available to calculate differential stress based on grain size. The differential stress values used in the diopside flow law calculations are assumed to be the same as those of quartz, as explained in the Discussion section.

5.3 Textural Analysis

During viscous deformation, rocks accommodate strain through a variety of deformation mechanisms such as diffusion and dislocation creep. Grain size, temperature, and differential stress are some of the key controls on which of these deformation mechanisms is the most favorable (Rybacki and Dresen, 2004; Mehl and Hirth, 2008; Czaplinska *et al.*, 2015; Miranda *et al.*, 2016). Generally speaking, higher differential

stresses favor dislocation creep over diffusion creep, and smaller grain sizes favor grain size-sensitive diffusion creep over grain size-insensitive dislocation creep. Evidence of which deformation mechanism was active at the time of deformation can be inferred by characterization of rock microstructure, notably by determination of grain size and interrogation of crystallographic orientations within minerals, determined by electron backscatter diffraction methods (*Prior et al.*, 1999). Strong crystallographic preferred orientations are evident of dislocation creep, while weak to absent crystallographic preferred orientations are consistent with a predominance of diffusion creep (*Prior et al.*, 1999). Determination of the dominant deformation mechanism acting in a phase is crucial in selecting the correct constitutive equation variables A , Q , n , and m in equation (2).

Misorientation axes can also help constrain the activation of distinct slip systems during dislocation creep. Misorientation axes are defined as changes in the internal grain orientation between 2-10° that cause the crystal structure to bend producing subgrains. Crystallographic orientations and misorientation axes are reported for quartz, plagioclase, enstatite, and diopside in the subsections below to aid in the determination of deformation processes.

5.3.1 Quartz

Nearly all samples preserve a strong crystallographic preferred orientation (CPO) in quartz. CPO patterns show a predominance of c -axis ([0001]) point maxima aligned within the foliation plane perpendicular to lineation and a -axes that form girdles at high angle to the foliation. These observations are consistent with the pattern expected for prism $\langle a \rangle$ slip in quartz. In a few samples (e.g., CH09-16fs), c -axes form girdle or cross-girdle distributions, possibly representing combined rhomb $\langle a \rangle$ slip and prism $\langle a \rangle$ slip

(Fig. 5a). The misorientation axes for quartz in the majority of samples show the strongest maximum in the [0001] direction, with a weaker maximum girdled between the two *a*-axes, further suggesting a predominance prism $\langle a \rangle$ slip in quartz.

5.3.2 Plagioclase

In the sample suite, plagioclase primarily records three CPO textures: (1) “axial-A” textures based on [100] point maximum parallel to the lineation and (010) girdles perpendicular to the foliation (*Satsukawa et al.*, 2013), consistent with (010)[100] slip, (2) “type P” textures, where all three crystallographic axes are characterized by point maximum distributions (*Satsukawa et al.*, 2013), and (3) “axial-B” textures defined by [100] girdles perpendicular to the foliation and with a strong point maxima of (010) planes perpendicular to the foliation (*Satsukawa et al.*, 2013) (Fig. 5b). Among these different CPO patterns, active slip systems range from (001)[100] to (010)[100], and to a lesser degree activation of (010)[001] slip. Despite the apparent range of CPO types recorded in plagioclase, misorientation axes consistently record dominant (010)[001] slip system. These observations are consistent with the findings of past studies of crystallographic textural formation in lower crustal plagioclase (*Gomez-Barrero et al.*, 2007; *Mehl and Hirth*, 2008).

5.3.3 Enstatite

Enstatite in gabbro and charnockite samples similarly show strong crystallographic textures defined by [001] point maxima aligned parallel to the lineation, with the majority of samples also showing weakly girdled [100] perpendicular to the foliation, indicative of slip on the (100)[001] system (*Bystricky et al.*, 2016) (Fig. 5c). Enstatite misorientation axes yield the strongest point maxima centered on either the *c*-

axis ([001]) or girdled between the c -axis and the a -axis ([100]), further suggesting slip along the a -plane in the c -direction.

5.3.4 Diopside

Diopside consistently show strong fiber crystallographic textures (Mauler *et al.*, 2000) in the sample suite, with girdled c -axis alignment parallel to the lineation and b -axis point maxima aligned perpendicular to the plane of foliation (Fig. 5d). This textural pattern in clinopyroxene is described as an “S-type” CPO, which indicates combined slip on the $\{110\}[001]$, $\{110\}1/2<110>$, and $(100)[001]$ systems (Mauler *et al.*, 2000; Zhang *et al.*, 2006). Diopside misorientation axes show girdles perpendicular to the c -axis, with higher concentrations centered on the a -axis. These results are consistent with CPOs observed on experimental clinopyroxene samples (Mauler *et al.*, 2000; Zhang *et al.*, 2006).

5.4 Compositional Analysis and Geothermometry

Plagioclase compositions within gabbro samples contain little to no potassium feldspar and have two to three times more calcium than sodium, classifying them as bytownite. Between different samples, all plagioclase compositions lie between An₈₁₋₆₇. Some samples show very little variation in mineralogy between plagioclase grains, with compositions between An₇₀₋₇₂. Other samples do show a range of compositions between different grains, with differences as large as An₈₀₋₆₉ in a single sample.

Pyroxene grains show no zoning between cores and rims. Enstatite shows little chemical variation between grains in all samples and has Mg concentrations of $X_{\text{Mg}} = 0.44\text{-}0.50$. Diopside similarly has little chemical variation and is comprised of an even lesser amount of magnesium ($X_{\text{Mg}} = 0.28\text{-}0.36$). While enstatite has minimal Ca ($X_{\text{Ca}} =$

0.01-0.02) and considerably high Fe concentrations ($X_{\text{Fe}} = 0.44\text{-}0.50$), diopside has relatively high calcium concentrations ($X_{\text{Ca}} = 0.44\text{-}0.46$) and much lower Fe concentrations ($X_{\text{Fe}} = 0.28\text{-}0.36$).

Equilibrium temperatures were calculated for the eight spatially distinct gabbro samples using two-pyroxene geothermometry based on the exchange of iron and magnesium. For each sample, a minimum of nine different temperatures were calculated for nine separate orthopyroxene-clinopyroxene pairs based on the geothermometers calibrated by Brey and Kohler (1990), Taylor (1998), and Putirka (2008). Temperatures were calculated assuming that all samples were subjected to pressures of 0.8 GPa, based on previous studies conducted in the region (*Collins and Shaw*, 1994; *Staffier*, 2007; *Waters-Tormey et al.*, 2009).

Calculated temperatures range from ca. 690-730°C, 800-850°C, and 830-850°C based on the geothermometers of Brey and Kohler (1990), Taylor (1998), and Putirka (2008), respectively. The average temperatures from these three thermometers vary within error of the respective calibrations, ranging from ca. 780-810 °C and implying little variation in temperature throughout the Ceilidh Hill massif (Table 3).

6. Discussion

The results obtained from microstructural analysis, namely EBSD and electron microprobe analysis, suggest that all of the major mineral phases in these samples are deforming by dislocation creep under anhydrous conditions with temperatures of ca. 800°C and differential stress conditions of 34-54 MPa. This information is applied to the constitutive equations for a non-Newtonian material undergoing viscous deformation

(Equation 2) in order to quantify the monophase rheologies for each major phase, in terms of strain rate and effective viscosity. These results are subsequently used to quantify the rheology of these naturally deformed, polyphase samples by applying the Minimized Power Geometric model proposed by Huet et al. (2014) and the AEH and FE methods proposed by Cook (2006). The aggregate viscosities determined from this study provide insight on lithospheric strength in natural systems, as discussed below.

6.1 Textural Analysis

Patterns of crystallographic preferred orientation and microstructures preserved within quartz grains are indicative of medium to high temperature (500° to >700°C) deformation (*Tullis et al.*, 1973; *Hirth and Tullis*, 1992). Further, the slip systems active in diopside crystals, as revealed by their CPO patterns, are similarly characteristic of high temperature (>500°C) deformation based on extrapolation from laboratory experiments (*Mauler et al.*, 2000). The presence of strongly developed crystallographic textures in all major phases (i.e., quartz, plagioclase, enstatite, and diopside) suggests that all phases are deforming dominantly by dislocation creep. This implies that the active deformation recorded in these rocks is grain size-insensitive, and that there exists a power law relationship between differential stress and strain rate (i.e., the stress exponent, n , is greater than 1). Using the flow law parameters for each phase deforming in dislocation creep given in Table 1, we are able to quantify the strain rate and effective viscosity of the naturally deformed lower crustal rocks exhumed in the Mount Hay region.

6.2 Monophase Flow Laws

To determine the rheology of naturally deformed lower crustal material in terms of strain rate and effective viscosity, the constitutive equations for viscous deformation

(Equation 2) requires knowledge of differential stress, temperature and pressure, water content, and the dominant deformation mechanisms acting in the rock. All of these unknowns are preserved within the microstructural record of the rock and were quantified using the advanced microstructural analytical techniques described above. Using the microstructural results and geothermometry, we calculated monophasic strain rates and effective viscosities for quartz, plagioclase, enstatite, and diopside (Table 4). Because these rocks are granulites and contain no hydrous minerals, we assume they are dry (i.e., the water content is negligible). Based on patterns of CPO and misorientation axes, we also assume that all grains are deforming predominantly by dislocation creep, eliminating the need to account for the potential effects of grain boundary sliding.

For the flow law calculations, we use the differential stress determined from the quartz paleopiezometer. We assume that differential stresses calculated based on the quartz recrystallized grain size are most likely to reflect the conditions experienced by the rocks in the sample suite. It is likely that the stress values recorded by plagioclase grains are too high due to Zener pinning (*Farla et al., 2013*), wherein the presence of a secondary phase (e.g., enstatite or diopside) can inhibit plagioclase growth due to grain boundary kinetics on non-like phase boundaries. If this is the case, then the plagioclase grains are likely smaller than predicted in a monophasic aggregate and thus would record a higher apparent differential stress than the true stress state experienced by the sample at the time of deformation. Quartz, on the other hand, is likely not affected by secondary mineral pinning because the quartz grew in segregated, monophasic bands in both charnockite and gabbro, and so its grain boundary kinetics are controlled by other neighboring quartz grains, which are not expected to hinder mineral growth. This implies

that the quartz is more likely to record the true differential stress as opposed to the plagioclase, which grew in polyphase domains with pyroxene. In contrast to plagioclase, enstatite grain sizes are likely to record lower differential stresses than quartz. Many of the grain size distribution plots of enstatite grains illustrate two peaks (Fig. 4c); a peak corresponding to larger grain diameters suggests the presence of relict grains that did not fully recrystallize, whereas a second peak centered on smaller diameters most likely corresponds to the average grain size of recrystallized enstatite grains. For samples with an obvious second peak, differential stresses were calculated based on the geometric mean of the smaller grain size peak that represents the recrystallized grains. However, the second peak may still include some relict grain diameters, thus introducing the possibility of a false differential stress based not only on the recrystallized enstatite grains, but also on the relict enstatite grains.

Monophase effective viscosities were also calculated for all major phases at constant strain rates of 10^{-18} s^{-1} , 10^{-16} s^{-1} , 10^{-14} s^{-1} , 10^{-12} s^{-1} , and 10^{-10} s^{-1} (Fig. 6). Over this range, monophase enstatite is typically the strongest phase (i.e., highest effective viscosity) and monophase quartz is consistently the weakest phase (i.e., lowest effective viscosity). The strength of plagioclase feldspar and diopside fall between these two endmembers. One exception to this generalized behavior occurs at a strain rate of 10^{-18} s^{-1} , where monophase diopside has a slightly higher effective viscosity than monophase enstatite. Plagioclase feldspar is weaker than diopside at lower strain rates ($<10^{-14} \text{ s}^{-1}$), whereas it is stronger at higher strain rates ($>10^{-14} \text{ s}^{-1}$) (Fig. 6). The difference in effective viscosity between the strongest phase and weakest phase ranges by approximately 1-2 orders of magnitude, depending on the strain rate.

6.3 Polyphase Mixing

Aggregate viscosities for each sample were calculated using the Minimized Power Geometric model of Huet et al. (2014) following the approach of Shinevar et al. (2015) (Table 5). All variables used are given in Table 1, assuming deformation by dislocation creep. Modal percentages of phases in each sample were normalized relative to quartz, plagioclase, enstatite, and diopside. Effective viscosities for each polyphase sample were calculated using the temperature determined through geothermometry. Effective viscosities were calculated over a range of strain rates from 10^{-18} s^{-1} to 10^{-10} s^{-1} and compared to predicted monophase effective viscosities under the same conditions (Fig. 6a & b).

For a constant strain rate, the effective aggregate viscosity of our natural samples varies by up to one order of magnitude, based solely on differences in the modal percentage of the dominant mineral phases. The magnitude of effective viscosity for gabbro samples, which have a low modal abundance of quartz and high modal abundances of pyroxene, generally falls within the range of values for monophase plagioclase (Fig. 6b). In contrast, charnockite samples containing higher modal abundances of quartz tend to have lower effective viscosities falling closer to the effective viscosity expected calculated for monophase quartz, approximately halfway between the monophase plagioclase and monophase quartz values (Fig. 6a).

It is important to note that in order to meet the criteria for using the Minimized Power Geometric model, the distribution of phases in the material of interest must be homogeneous and isotropic (Huet et al., 2014). While the microstructure of gabbro samples more or less fit this requirement, caution should be used while calculating the

bulk viscosities of some charnockite samples. Given the fact that many of the charnockite samples contain interlocking layers of quartz, this mixing model may be over-estimating the aggregate viscosity by assuming that the weakest phase (i.e. quartz) is dispersed evenly throughout the rock, as opposed to forming a connected network that dominates the behavior of the bulk rock. Additionally, in order to avoid potential problems relating to anisotropic viscosity, the Minimized Power Geometric model assumes that phases do not preserve a CPO (*Huet et al.*, 2014), which is not the case for our sample suite. Thus, we emphasize that our results using this mixing model should only be taken as an estimate and that there are still many factors that require future work to better understand how they will affect the rheology of polyphase lower crustal materials.

6.4 Power-Law Creep Polyphase Rheology

A second approach to determining the aggregate polyphase viscosity of our samples relies upon a numerical solution of effective viscosity made possible by the Power-Law Creep (PLC) GUI toolbox of Cook (2016), which calculates bulk rheology using AEH and FE methods. Representative subsections of fifteen EBSD phase maps were traced in Adobe Illustrator and uploaded into the software toolbox for numerical analysis. Similar to the previous method, all samples were normalized to include only quartz, plagioclase, enstatite, and diopside. The modal percentage of each phase was computed by the program based on the uploaded image. Input parameters for the PLC toolbox include the flow law variables for each phase, the temperature, and strain rate values of interest. As in the previous calculations, flow law variables for dislocation creep are assumed (Table 1) and the range of temperature and strain rates follow those used in the earlier mixing calculations.

With these inputs, the PLC toolbox calculates the bulk aggregate rheology in terms of log stress and log strain rate, which was then converted into an effective viscosity (Table 6). For each sample, the range of bulk effective viscosities determined for strain rates of 10^{-18} s^{-1} to 10^{-10} s^{-1} were plotted alongside the expected monophase viscosities for each major phase for comparison (Fig. 6c & d). As seen in the previous model, the effective viscosities predicted for the polyphase samples lie either very close to those expected for monophase plagioclase or in between that of monophase quartz and monophase plagioclase. The model derived from AEH and FE methods does not show a significant variation in rheology between samples, as suggested by the fact that all viscosities at a single strain rate are within a half an order of magnitude of each other. For the most part, the bulk viscosity of gabbro samples closely resembles that of plagioclase (Fig. 6d), while the bulk viscosity of charnockite samples is slightly lower than that of plagioclase (Fig. 6c). The variation in rheology between the natural samples is a function of the modal percentages of major phases, as well as the distribution of phases. These results show, on average, slightly higher aggregate viscosities than those obtained from the Minimized Power Geometric model of Huet et al. (2014), but the overall trend of these two models shows remarkable consistency.

6.5 Implications for Lower Crustal Rheology

Effective viscosities of naturally deformed polyphase lower crustal granulites calculated by means of the applied mixing model and PLC toolbox yield similar results. These results also support conclusions found in past studies. For example, Thatcher and Pollitz (2007) estimated the rheology of the lower crust based on geophysical estimates, such as glacio-isostatic adjustment, lithosphere isostatic adjustment, and postseismic

relaxation geodetic data and concluded that at strain rates between 10^{-13} s^{-1} to 10^{-14} s^{-1} , the effective viscosity of the lower crust is between 10^{19} to 10^{21} Pa.s (i.e., the range of effective viscosities determined in our sample suite). These results are also consistent with a more recent study that modeled possible lower crustal compositions and applied polyphase mixing theory to different mineral assemblages as a means of calculating the rheology of the lower crust (*Shinevar et al.*, 2015).

There are variations in the rheology of the lower crust based on modal percentage and distribution, with the gabbro samples on average showing a higher viscosity than the charnockite samples. On Ceilidh Hill, gabbroic granulites are the dominant lithology, though smaller layers (i.e., the charnockitic granulites) and felsic segregations (i.e. blebs of quartzofeldspathic material within gabbro) are also present. If the connectivity of the felsic segregations and charnockite layers was abundant enough to form an interconnected network, then it is possible that the deformational behavior of these phases would dominate the rheology of the lower crust. However, because the felsic segregations are not interconnected at the decimeter to km-scales, and because gabbroic granulites are by far the most volumetrically significant unit exposed throughout Ceilidh Hill, the bulk rheology of the lower crust in this region is likely better described by the deformational behavior of the naturally deformed gabbroic samples analyzed in this study.

Quantifying the rheology of the lower crust is imperative to understanding the strength of the lithosphere as a whole. One common model of lithospheric rheology proposes that its strength profile is similar to that of a jelly sandwich where a weak lower crust is sandwiched between a stronger upper crust and a strong upper mantle (cf.

Burgmann and Dresen, 2008; and references therein). An alternative model suggests that the strength of the lithosphere is instead analogous to crème brûlée, characterized by a strong upper crust underlain by both a weak lower crust and a weaker upper mantle (cf. *Burgmann and Dresen, 2008; and references therein*). As a crude test to see which of these lithospheric strength models our region may more closely resemble, we applied the dry olivine flow law parameters of Hirth and Kohlstedt (1996) to our samples assuming the same extrinsic conditions (e.g. the same temperature, water content, and differential stress, as if the olivine was immediately below the Moho). The effective viscosities of the hypothetical mantle samples in this region were calculated to be between 5.35×10^{22} Pa.s to 1.60×10^{23} Pa.s, which is higher than what we see at geologically relevant strain rates for our polyphase lower crustal samples (Table 5 & 6). This suggests that the lithospheric strength in the Mount Hay region may be predominantly held in the brittle upper crust and in the upper mantle, whereas the lower crust is a comparatively weak rheological layer.

7. Conclusions

Microstructural techniques, including electron backscatter diffraction and two-pyroxene geothermometry, were used to directly constrain the rheology of the lower crust in naturally deformed, polyphase samples from the Mount Hay block of central Australia. Differential stresses, strain rates, and effective viscosities were calculated for all major phases using grain-size piezometry and experimentally-derived constitutive equations of different minerals. The temperatures used for the calculations ranged from ca. 780-810°C, as determined through Fe-Mg exchange thermometry. Differential stresses were

calculated to range from 34-54 MPa. Resulting monophase strain rates range from $2.10 \times 10^{-12} \text{ s}^{-1}$ to $1.56 \times 10^{-11} \text{ s}^{-1}$ for quartz, $4.68 \times 10^{-15} \text{ s}^{-1}$ to $2.48 \times 10^{-13} \text{ s}^{-1}$ for plagioclase feldspar, $1.56 \times 10^{-18} \text{ s}^{-1}$ to $1.64 \times 10^{-16} \text{ s}^{-1}$ for enstatite, and $5.66 \times 10^{-16} \text{ s}^{-1}$ to $1.00 \times 10^{-14} \text{ s}^{-1}$ for diopside. Calculated stresses and viscosities are generally within reason for what is predicted for the rheology of monophase materials in the lower crust. The monophase strain rates determined for enstatite and diopside appear too low for natural geologic strain rates, which may suggest that the flow law variables used are not applicable to the temperature conditions of this study and that caution should be used when extrapolating these to the specific natural conditions preserved on Ceilidh Hill.

The bulk rheology (i.e., effective viscosity) of naturally deformed, polyphase lower crustal rocks were calculated using two independent methods: the mixing model proposed by Huet et al. (2014) and AEH and FE methods applied to the Power-Law Creep toolbox created by Cook (2016). These two methods produced complementary results, both suggesting that the bulk rheology of gabbroic to charnockitic lower crust likely falls between the effective viscosity expected for monophase plagioclase and monophase quartz, and that it varies as a function of composition. The effective viscosities produced by these methods agree well with those determined from other studies (*Thatcher and Pollitz, 2007; Shinevar et al., 2015*). Future studies can expand upon the results of this study by examining heterogeneous lower crustal rocks in other localities to provide estimates of lower crustal rheology under varying deformation conditions (e.g., temperature, extraction depths, water content, composition, and deformation history).

References:

- Beaumont, C., R.A. Jamieson, M.H. Nguyen, and B. Lee (2001), Himalayan tectonics explained by extrusion of a low-viscosity crustal channel coupled to focused surface denudation, *Letters to Nature*, vol. 414, 738-742
- Betts, P.G. and D. Giles (2006), The 1800-1100 Ma tectonic evolution of Australia, *Precambrian Research* 144, 92- 125, doi:10.1016/j.precamres.2005.11.006
- Bonamici, C.E., B. Tikoff, and L.B. Goodwin (2011), Anatomy of a 10 km scale sheath fold, Mount Hay ridge, Arunta Region, central Australia: The structural record of deep crustal flow, *Tectonics*, vol. 30, TC6015, doi:10.1029/2011TC002873
- Brey, G.P. and T. Kohler (1990), Geothermobarometry in Four-phase Lherzolites II. New Thermobarometers, and Practical Assessment of Existing Thermobarometers, *Journal of Petrology*, vol 31, part 6, 1353-1378
- Bruijn, R.H.C. and P. Skemer (2014), Grain-size sensitive rheology of orthopyroxene, *Geophysical Research Letters*, 41, doi:10.1002/2014GL060607
- Burgmann R. and G. Dresen (2008), Rheology of the Lower Crust and Upper Mantle: Evidence from Rock Mechanics, Geodesy, and Field Observations, *Annual Review Earth Planet. Sci.*, 36:531-67, doi:10.1146/annurev.earth.36.031207.124326
- Bystricky, M., J. Lawlis, S. Mackwell, F. Heidelbach, and P. Raterron (2016), High-temperature deformation of enstatite aggregates, *Journal of Geophysical Research Solid Earth*, 121, 6384-6400, doi:10.1002/2016JB013011
- Collins, W.J. and R.D. Shaw (1995), Geochronological constraints on orogenic events in the Arunta Inlier: a review, *Precambrian Research* 71, 315-346
- Cook, A.C. (2016), Microstructural analysis of thermoelastic response, nonlinear creep, and pervasive cracking in heterogeneous materials, *The University of Maine Graduate School*, PhD Dissertation
- Cross, A.J., G. Hirth, and D.J. Prior (2017), Effects of secondary phases on crystallographic preferred orientations in mylonites, *GEOLOGY*, doi:10.1130/G38936.1

- Czaplinska, D., S. Piazzolo, I. Zibra (2015), The influence of phase and grain size distribution on the dynamics of strain localization in polymineralic rocks, *Journal of Structural Geology*, 72, 15-32, doi:10.1016/j.jsg.2015.01.001
- Dimanov, A. and G. Dresen (2005), Rheology of synthetic anorthite-diopside aggregates: Implications for ductile shear zones, *Journal of Geophysical Research: Solid Earth*, 110, B07203, doi:10.1029/2004JB003431
- Farla R.J.M., S. Karato, and Z. Cai (2013), Role of orthopyroxene in rheological weakening of the lithosphere via dynamic recrystallization, *PNAS vol. 110 no. 41*, 16355-16360, doi:10.1073/pnas.1218335110
- Getsinger, A.J., G. Hirth, H. Stunitz, and E.T. Goergen (2013), Influence of water on rheology and strain localization in the lower continental crust, *Geochemistry Geophysics Geosystems vol. 14 no. 7*, 2247-2264, doi:10.1002/ggge.20148
- Gomez-Barreiro, J., I. Lonardelli, H.R. Wenk, G. Dresen, E. Rybacki, Y. Ren, and C.N. Tome (2007), Preferred orientation of anorthite deformed experimentally in Newtonian creep, *Earth and Planetary Science Letters*, 264, 188-207, doi:10.1016/j.epsl.2007.09.018
- Hansen, L. N., M. E. Zimmerman, and D. L. Kohlstedt (2011), Grain boundary sliding in San Carlos olivine: Flow law parameters and crystallographic-preferred orientation, *Journal of Geophysical Research*, 116, B08201, doi:10.1029/2011JB008220
- Hetzel, R. and A. Hampel (2005), Slip rate variations on normal faults during glacial-interglacial changes in surface loads, *Letters to Nature*, vol. 435, 81-84
- Hirth, G. and J. Tullis (1992), Dislocation creep regimes in quartz aggregates, *Journal of Structural Geology*, vol. 14, i. 2, 145-159, doi:10.1016/0191-8141(92)90053-Y
- Hirth, G. and D.L. Kohlstedt (1996), Water in the oceanic upper mantle: implications for rheology, melt extraction and the evolution of the lithosphere, *Earth and Planetary Science Letters*, 144, 93-108
- Hirth, G. and D.L. Kohlstedt (2003), Rheology of the upper mantle and the mantle wedge: A view from the experimentalists, *Geophysical Monograph Series*, 138, 83-105, doi:10.1029/138GM06
- Hirth, G., C. Teyssier, and W.J. Dunlap (2001), An evaluation of quartzite flow laws based on comparisons between experimentally and naturally deformed rocks, *Int J Earth Sciences (Geol Rundsch)* 90:

- Hoatson, D.M, S. Sun, and J.C. Claoue-Long (2005), Proterozoic mafic-ultramafic intrusions in the Arunta Region, central Australia: Part 1: Geological setting and mineral potential, *Precambrian Research*, vol. 142, i. 3-4, 93-133, doi:10.1016/j.precamres.2005.09.004
- Howlett, D., T. Raimondo, and M. Hand (2015), Evidence for 1808-1770 Ma bimodal magmatism, sedimentation, high-temperature deformation and metamorphism in the Aileron Province, central Australia, *Australian Journal of Earth Sciences*, vol. 62 i. 7, 831-852, doi:10.1080/08120099.2015.1108364
- Huet, B., P. Yamato, and B. Hrasemann (2014), The Minimized Power Geometric model: An analytical mixing model for calculating polyphase rock viscosities consistent with experimental data, *Journal of Geophysical Research Solid Earth*, 119, 3897-3924, doi:10.1002/2013JB010453
- Lambeck, K., C. Smither, and P. Johnston (1998), Sea-level change, glacial rebound and mantle viscosity for northern Europe, *Geophysical Journal International*, vol. 134, i 1, 102-144
- Lawlis, J.D. (1998) High temperature creep of synthetic olivine-enstatite aggregates, *The Pennsylvania State University Graduate School, Department of Geosciences*, PhD Thesis
- Linckens, J., R.H.C. Bruijn, and P. Skemer (2014), Dynamic recrystallization and phase mixing in experimentally deformed peridotite, *Earth and Planetary Science Letters*, 388, 134-142, doi:10.1016/j.epsl.2013.11.037
- Mainprice, D., F. Bachmann, R. Hielscher, and H. Schaeben (2014) Descriptive tools for the analysis of texture projects with large datasets using MTEX: strength, symmetry and components, *Geological Society, London, Special Publications*, 409, 251-271, doi:10.1144/SP409.8
- Mauler, A., M. Bystricky, K. Kunze, and S. Mackwell (2000), Microstructures and lattice preferred orientations in experimentally deformed clinopyroxene aggregates, *Journal of Structural Geology*, 22, 1633-1648, doi:10.1016/S0191-8141(00)00073-0
- Mehl, L. and G. Hirth (2008), Plagioclase preferred orientation in layered mylonites: Evaluation of flow laws for the lower crust, *Journal of Geophysical Research*, 113, B05202, 1-19, doi:10.1029/2007JB005075
- Miranda, E.A., G. Hirth, and B.E. John (2016), Microstructural evidence for the transition from dislocation

- creep to dislocation-accommodated grain boundary sliding in naturally deformed plagioclase, *Journal of Structural Geology*, 92, 30-45, doi:10.1016/j.jsg.2016.09.002
- Ord, A. and B.E. Hobbs (1989), The strength of the continental crust, detachment zones, and development of plastic instabilities *Tectonophysics* 158, 269-289
- Prior D.J., A. Boyle, F. Brenker, M. Cheadle, A. Day, G. Lopez, L. Peruzzo, G. Potts, S. Reddy, R. Spiess, N. Timms, P. Trimby, J. Wheeler, and L. Zetterstrom (1999), The application of electron backscatter diffraction and orientation contrast imaging in the SEM to textural problems in rocks, *American Mineralogist*, 84, 1741-1759
- Putirka, K.D. (2008), Thermometers and Barometers for Volcanic Systems, *Reviews in Mineralogy and Geochemistry*, 69 (1), 61-120, doi.org/10.2138/rmg.2008.69.3
- Rahl, J.M. and P. Skemer (2016), Microstructural evolution and rheology of quartz in a mid-crustal shear zone, *Tectonophysics* 680, 129-139, doi:10.1016/j.tecto.2016.05.022
- Raterron, P. and O. Jaoul (1991), High-Temperature Deformation of Diopside Single Crystal 1. Mechanical Data, *Journal of Geophysical Research*, vol. 96, no. B9, 14277-14286
- Rybacki, E. and G. Dresen (2004), Deformation mechanism maps for feldspar rocks, *Tectonophysics*, 382, 173-187, doi:10.1016/j.tecto.2004.01.006
- Satsukawa, T., B. Ildefonse, D. Mainprice, L.F.G. Morales, K. Michibayashi, and F. Barou (2013), A database of plagioclase crystal preferred orientations (CPO) and microstructures- implications for CPO origin, strength, symmetry and seismic anisotropy in gabbroic rocks, *Solid Earth*, 4, 511-542, doi:10.5194/se-4-511-2013
- Shinevar, W.J., M.D. Behn, and G. Hirth (2015), Compositional dependence of lower crustal viscosity, *Geophysical Research Letters*, 42, 8333-8340, doi:10.1002/2015GL065459
- Shinevar, W.J., M.D. Behn, G. Hirth, and O. Jagoutz (2018), Inferring crustal viscosity from seismic velocity: Application to the lower crust of Southern California, *Earth and Planetary Science Letters*, 494, 83-91, doi.org/10.1016/j.epsl.2018.04.055
- Skemer, P., I. Katayama, Z. Jiang, and S. Karato (2005), The misorientation index: Development of a new method for calculating the strength of lattice-preferred orientation, *Tectonophysics*, vol. 411, i. 1-4, 157-167, doi:10.1016/j.tecto.2005.08.023

- Staffier, K. (2007), Field and Microstructural Investigation of Plagioclase Deformation Behavior in Granulite Facies Rocks, Mt. Hay, Central Australia, *University of Wisconsin—Madison*
- Stipp, M. and J. Tullis (2003), The recrystallized grain size piezometer for quartz, *Geophysical Research Letters*, vol. 30, no. 21, 2088, doi:10.1029/2003GL018444
- Taylor, W.R. (1998) An experimental test of some geothermometer and geobarometer formulations for upper mantle peridotites with application to the thermobarometry of fertile lherzolite and garnet websterite, *Neues Jahrbuch für Mineralogie, Abhandlungen*, vol. 172, i. 2-3, 381-408
- Thatcher, W. and F.F. Pollitz (2008), Temporal evolution of continental lithospheric strength in actively deforming regions, *GSA Today*, 18, 4/5, 4-11
- Tikoff B., C. Teyssier, and C. Waters (2001), Clutch tectonics and the partial attachment of lithospheric layers, *EGU Stephan Mueller Special Publication Series*, 1, 57-73
- Tullis, J., J.M. Christie, and D.T. Griggs (1973), Microstructures and Preferred Orientations of Experimentally Deformed Quartzites, *GSA Bulletin* 84, 297-314
- Twiss, R.J. (1977), Theory and Applicability of a Recrystallized Grain Size Paleopiezometer, *Pageoph*, vol. 115, 227-8
- Warren, R.G. (1983), Metamorphic and tectonic evolution of granulites, Arunta Block, central Australia, *Nature* vol. 305, i. 22, 300-303
- Waters-Tormey, C., K.T. Ashley, D. Jones, and R. Tracy (2016), The Mount Hay block, central Australia: Another puzzle piece for Paleo-Mesoproterozoic tectonic history, *Precambrian Research* 281, 537-565, doi:10.1016/j.precamres.2016.03.006
- Wdowinski, S. and G.J. Axen (1992), Isostatic rebound due to tectonic denudation: A viscous flow model of a layered lithosphere, *Tectonics* vol 11, i 2, 303-31
- Zhang, J., H.W. Green II, and K.N. Bozhilov (2006), Rheology of omphacite at high temperature and pressure and significance of its lattice preferred orientations, *Earth and Planetary Science Letters*, 246, 432-443, doi:10.1016/j.epsl.2006.04.006

Figures:

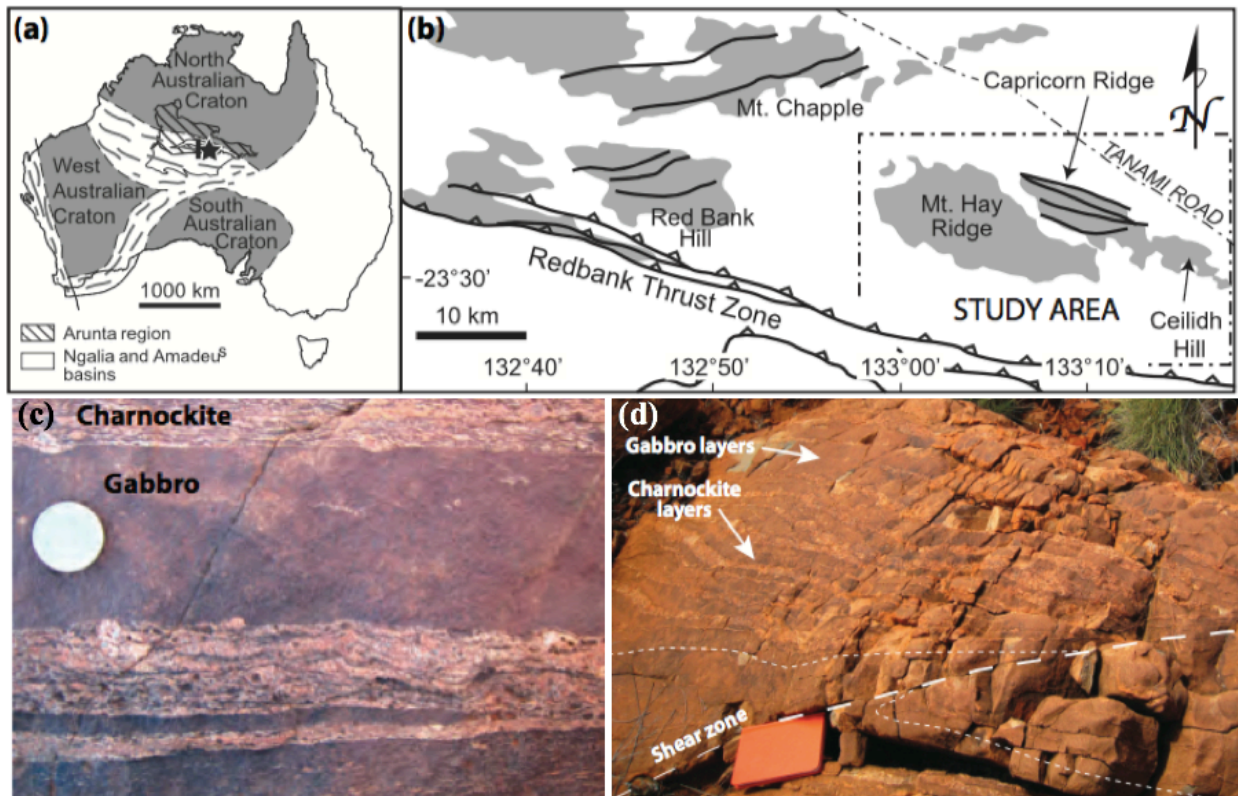


Figure 1. (a) Geological map showing the location of the Arunta Block within the Australian continent and the location of the field site denoted with a star as shown in b. (b) Detailed map of the field site in the vicinity of Mount Hay, showing the location of exhumed lower crustal granulite exposures (grey) and Ceilidh Hill (study area) with respect to the Redbank Thrust Zone to the South. (c) Outcrop photo showing interlayered mafic (gabbro) and felsic (charnockite) granulite exposures at Ceilidh Hill. (d) Mesoscale interlayering of granulites and cross-cutting shear zone present at Ceilidh Hill. Figures 1a and 1b are modified after *Waters-Tormey, 2007; Shaw & Black, 1991; Warren & Shaw, 1995; Hoatson et al., 2005.*

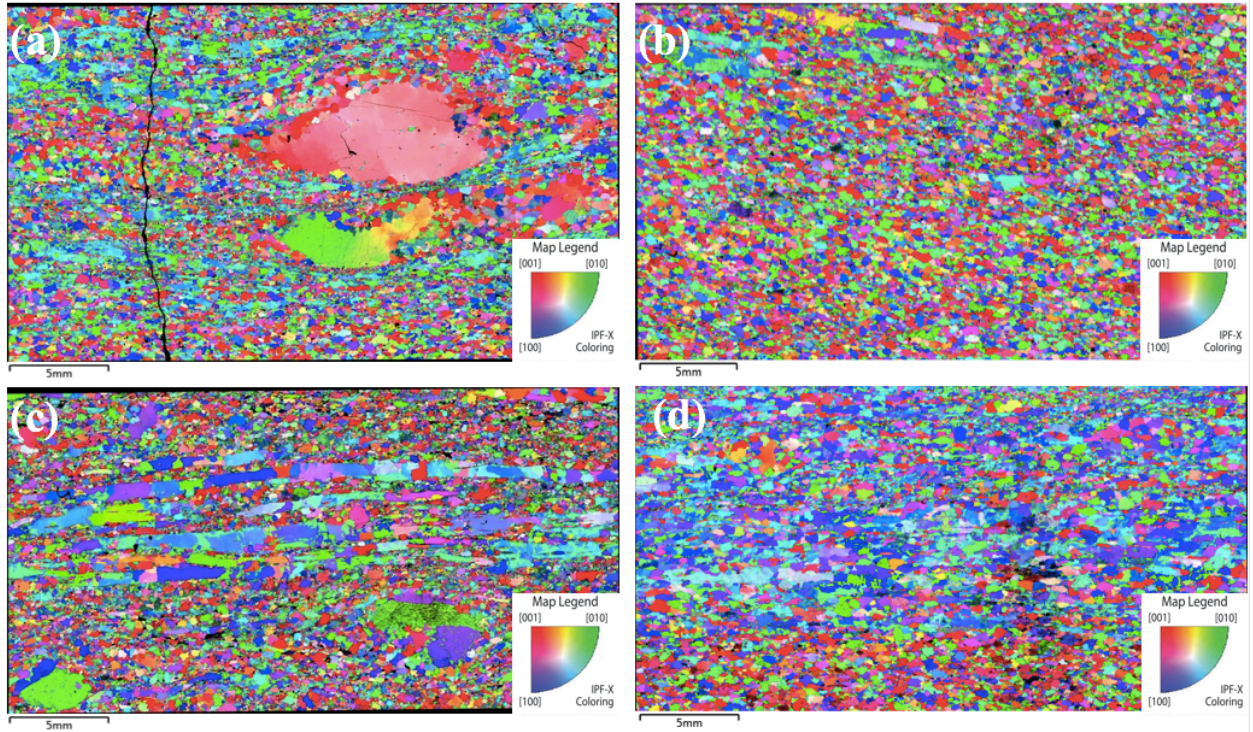


Figure 2. Full thin-section electron backscatter diffraction (EBSD) textural maps for (a) CH09-11ch, (b) CH09-57fs, (c) CH09-13ch-2, and (d) CH09-41ch. EBSD textural maps shown here are shown with inverse pole figure coloring in the x-direction (IPF-X maps), such that every color on the map indicates the distinct crystallographic axes within a grain that is aligned relative to the x-direction (right) of the thin section.

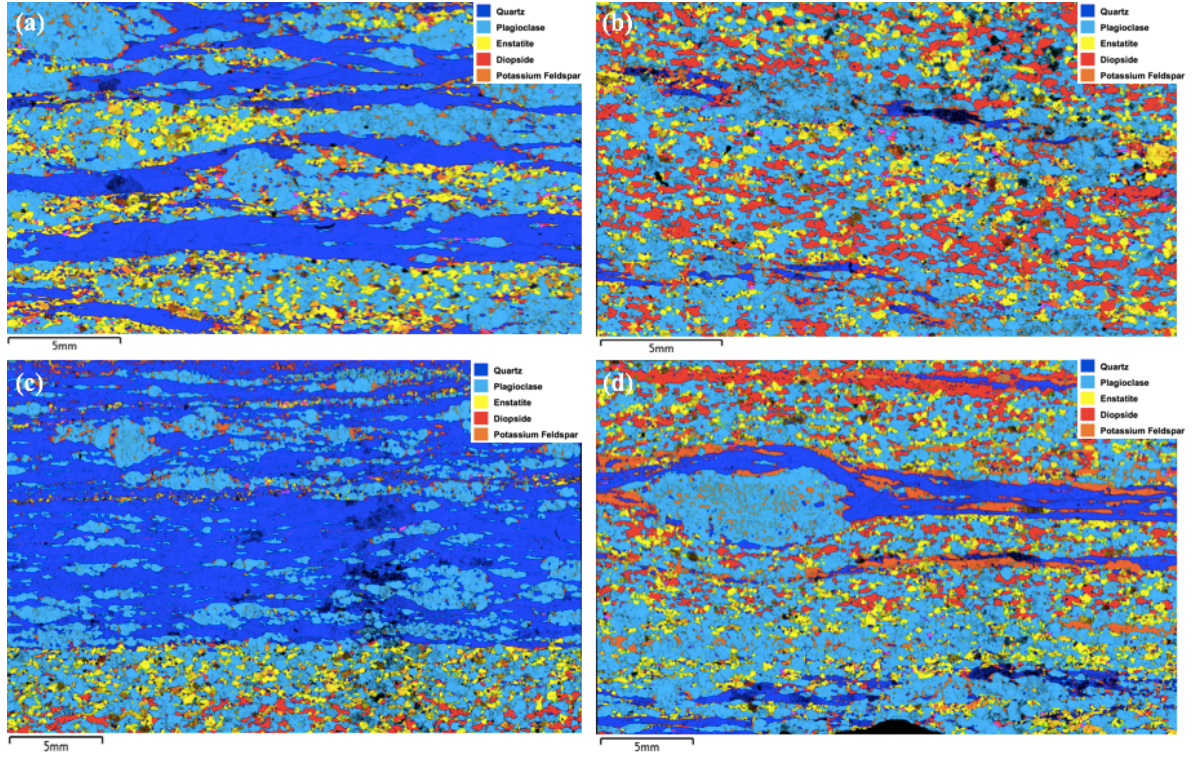


Figure 3. EBSD phase map showing compositional variation and phase distribution in representative Ceilidh Hill samples. (a) and (b) charnockite sample CH09-09A and gabbro sample CH09-09B, respectively, interlayered and sampled from the same locality at Ceilidh Hill. (a) In the charnockite, the quartz grains (dark blue) form interconnected monophasic ribbons throughout the rock, whereas plagioclase feldspar (light blue), enstatite (yellow), and diopside (red) form mixed, polyphase layers. (b) In the gabbro, plagioclase and pyroxene make up the majority of the bulk rock by mode. (c) and (d) charnockite sample CH09-41ch and gabbro sample CH09-41fs, respectively, interlayered and taken from the same field locality. (c) The charnockite also shows a network of interconnected quartz ribbons, whereas (d) the gabbro is characterized by a more homogeneous distribution of plagioclase and pyroxene in the matrix. Note also the preservation of a plagioclase porphyroclast and interspersed potassium feldspar (orange) in the gabbro shown in (d).

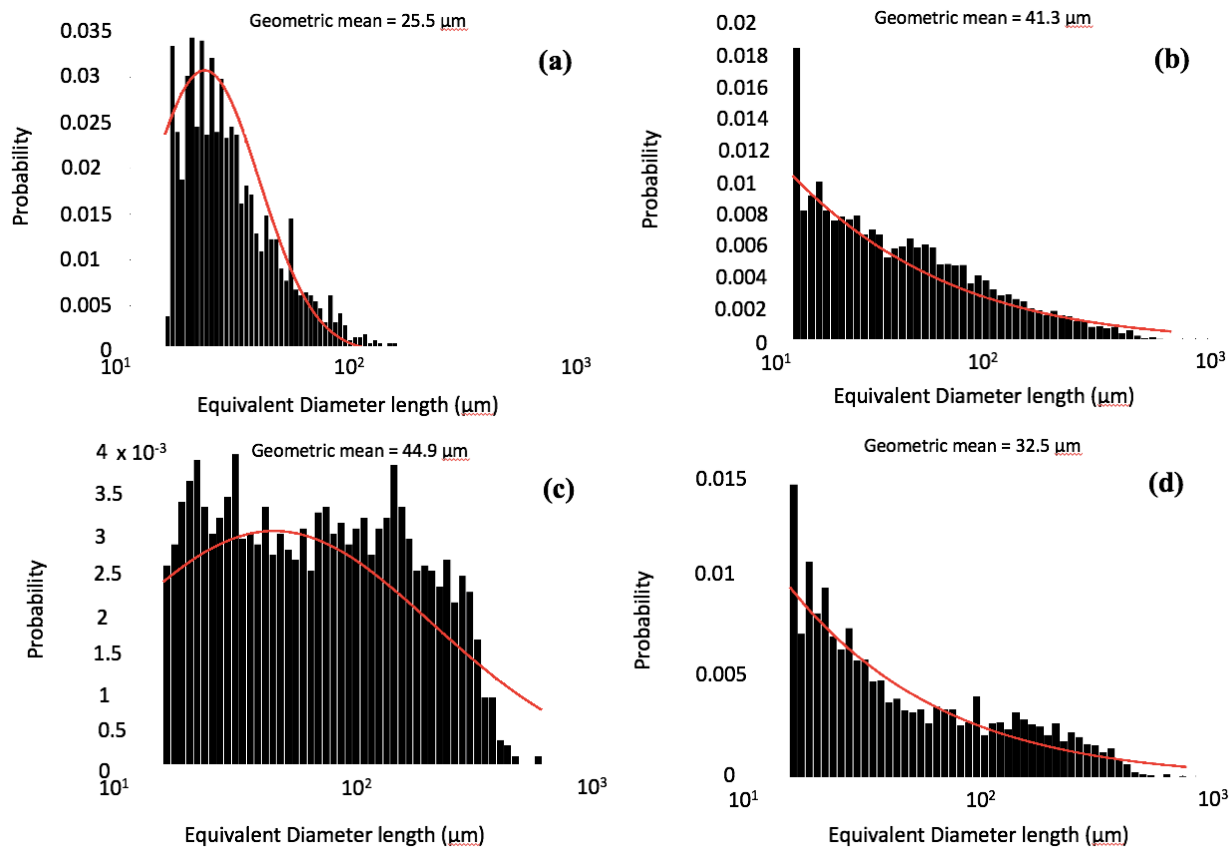
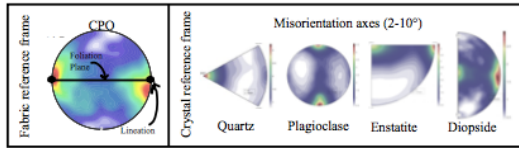
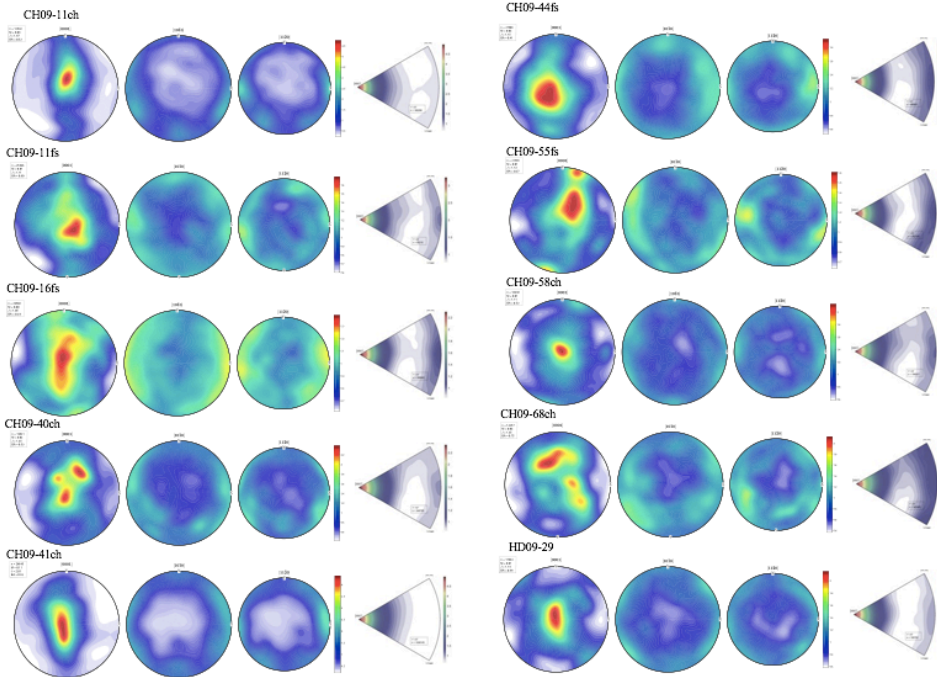


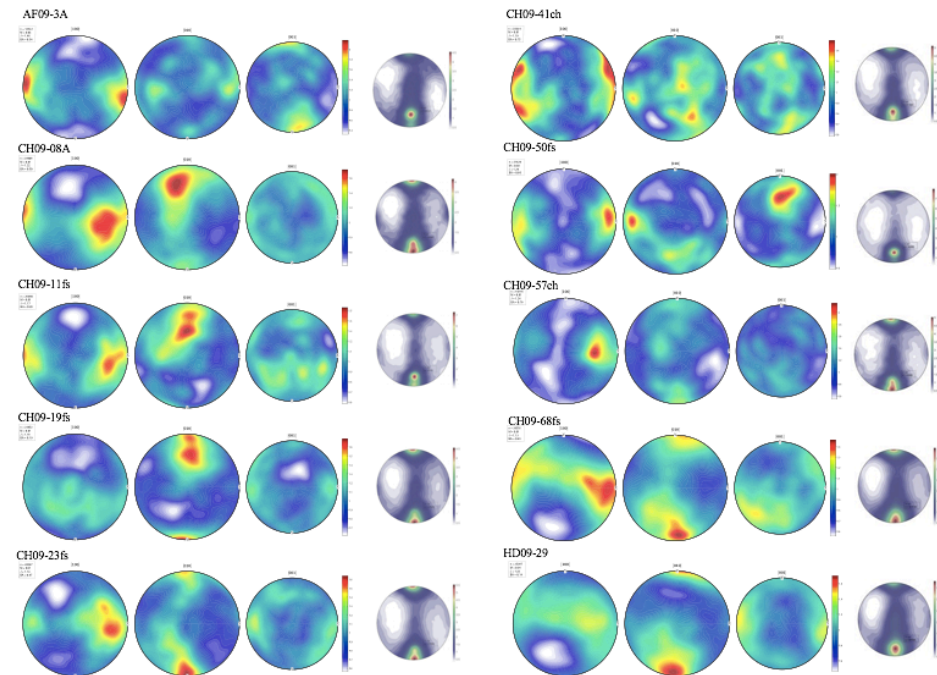
Figure 4. Grain size histograms showing the probability of the corrected equivalent-area grain diameters and their corresponding geometric mean grain size for (a) quartz, (b) plagioclase, (c) enstatite, and (d) diopside in sample CH09-08A. Note that (c) enstatite shows two prominent peaks.



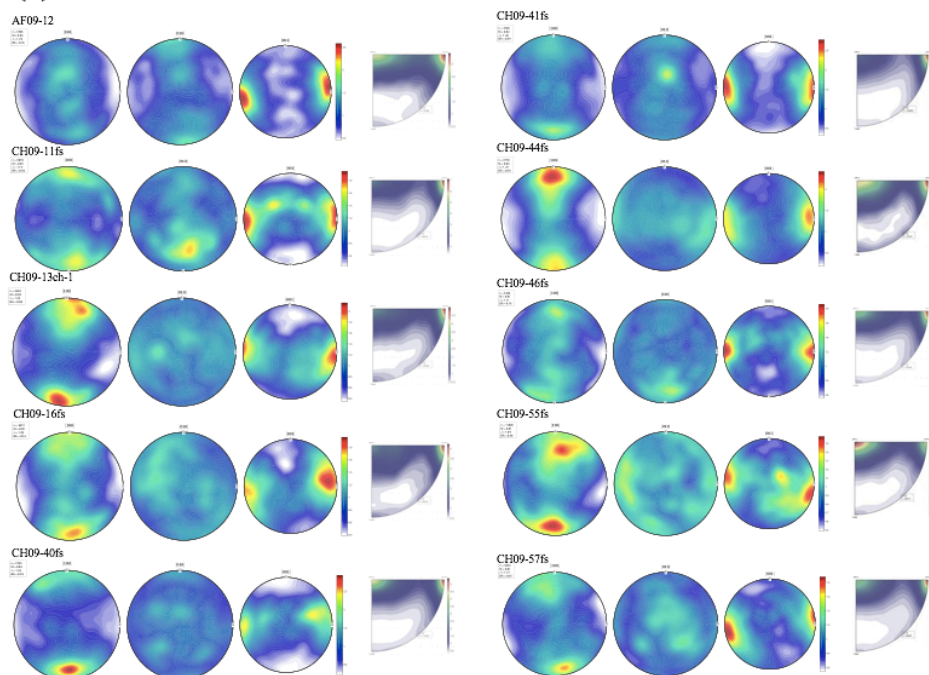
(a)



(b)



(c)



(d)

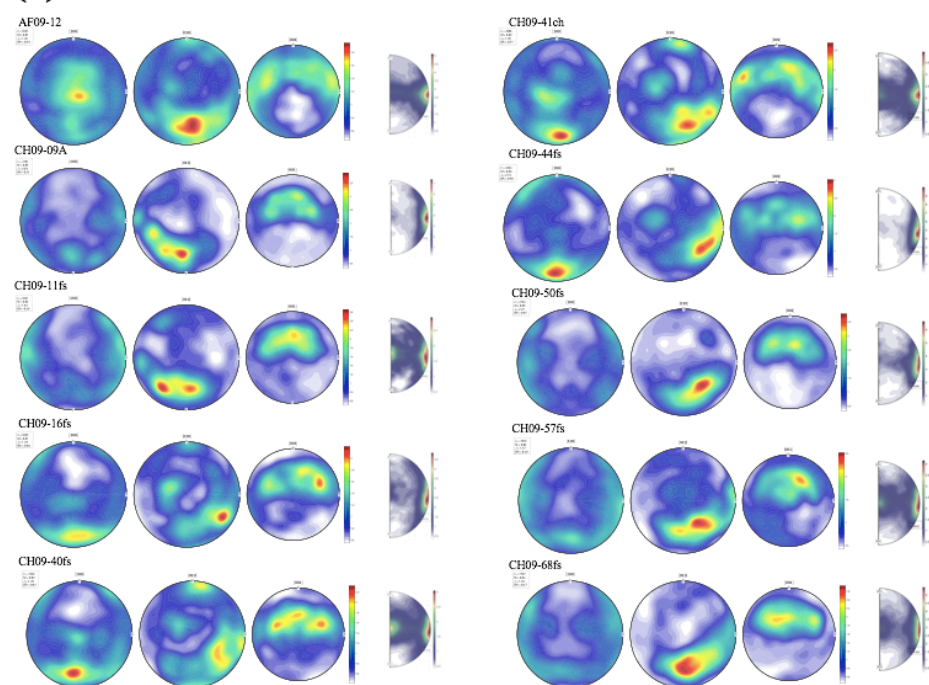


Figure 5. Lower hemisphere, equal area pole figures showing patterns of crystallographic preferred orientation (CPO) as orientation distribution functions (ODFs), and misorientation axes for (a) quartz, (b) plagioclase feldspar, (c) enstatite, and (d) diopside. The presence of strong crystallographic fabrics in all major phases is indicative of deformation dominated by dislocation creep. (a) Quartz samples show [0001] point maxima within the foliation plane perpendicular to lineation, consistent with patterns expected for prism $\langle a \rangle$ slip. (b) Plagioclase samples illustrate a range of CPO types, from axial-B, to type P, to axial-A (see text for description of each pattern). (c) Enstatite samples consistently preserve *c*-axis [001] point maximum aligned parallel to lineation. (d) Diopside samples show *c*-axes [001] girdles within the foliation plane and *b*-axes [010] with point maxima aligned sub-perpendicular to the plane of foliation.

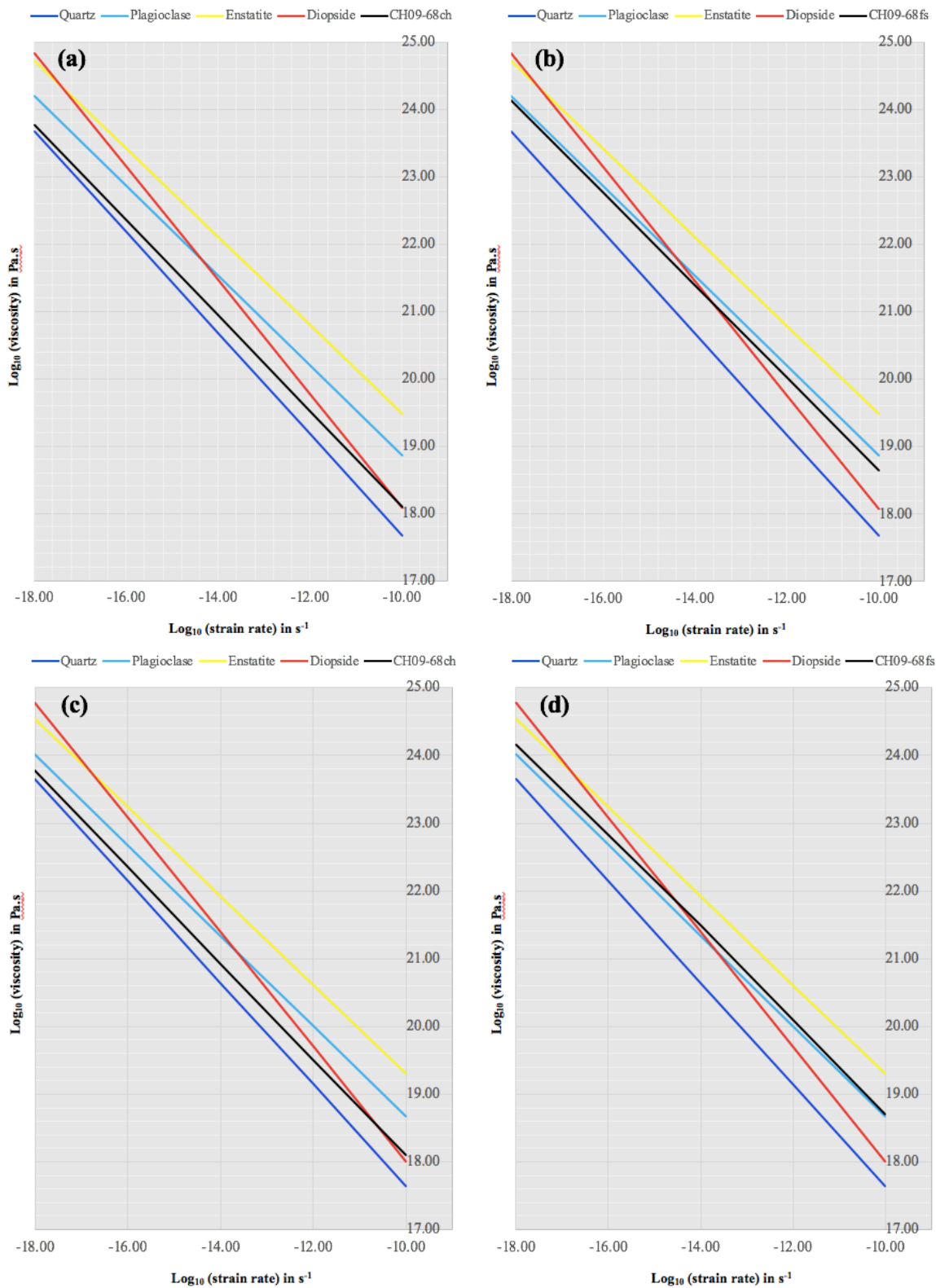


Figure 6. Plots of strain rate versus effective viscosity for monophase quartz (dark blue), plagioclase (light blue), enstatite (yellow), diopside (red), and our natural samples (black). Viscosities were calculated at 778 °C for a pair of interlayered charnockite and gabbro samples collected at the same field location. Bulk viscosities of (a) charnockite sample CH09-68ch and (b) gabbro sample CH09-68fs were calculated using the Minimized Geometric Power model. Comparatively, (c) and (d) shows the bulk viscosities calculated using the AEH and FE methods for the same charnockite and gabbro samples, respectively. The polyphase charnockite sample (a) and (c) has an effective viscosity that is between that of monophase plagioclase and monophase quartz, whereas the polyphase gabbro sample (b) and (d) has viscosity values similar to that of monophase plagioclase.

Tables:

Table 1. Flow Law Variables Used for Rheology Calculations

Phase	$\log(A)$	Q	n	m	Source
Quartz	-11.2 +/- 0.6 MPa/s	135 +/- 15 kJ/mol	4	1	<i>Hirth et al., 2001</i>
Plagioclase	12.7 +/- 0.6 MPa/s	648 +/- 20 kJ/mol	3	0	<i>Rybacki and Dresen, 2004</i>
Enstatite	8.63 +/- 0.73 MPa/s	600 kJ/mol	3	0	<i>Lawlis, 1998;</i> <i>Bruijn and Skemer, 2014;</i> <i>Bystricky et al., 2016</i>
Diopside	-7.8 +/- 2.4 ^a MPa/s	442 +/- 29 kJ/mol	6.46	0	<i>Raterron and Jaoul, 1991</i>

^athis value is $\ln(A)$

Table 2. Equivalent Diameter (D) and Differential Stress (σ) for Each Major Phase

Sample	Quartz D (μm)	Quartz σ (MPa)	Plagioclase D (μm)	Plagioclase σ (MPa)	Enstatite D (μm)	Enstatite σ (MPa)	Diopside D (μm)
AF09-3A	30.3	44.6	50.8	59.1	26.7	40.0	19.3
AF09-12	28.8	46.5	39.4	70.3	54.9	15.6	36.1
AF09-15	41.6	34.7	39.9	69.7	26.4	40.6	26.9
AF09-19	28.5	46.9	52.2	58.1	69.3	11.5	48.7
CH09-08A	25.5	51.2	41.3	68.1	22.4	50.4	32.5
CH09-08B	24.0	53.6	30.9	83.0	19.6	60.0	32.9
CH09-08C	25.4	51.3	32.9	79.5	21.7	52.5	30.5
CH09-09A	28.8	46.5	29.8	85.0	57.3	14.8	19.0
CH09-09B	24.7	52.5	31.1	82.6	66.8	12.1	31.5
CH09-11ch	29.1	46.1	22.4	103.3	36.8	26.3	17.3
CH09-11fs	27.9	47.7	27.0	90.9	54.4	15.8	28.3
CH09-13ch-1	28.4	47.0	25.0	95.7	53.2	16.3	19.9
CH09-13ch-2	35.9	39.0	24.6	97.0	53.1	16.3	19.8
CH09-13fs	30.5	44.4	30.2	84.2	53.6	16.1	32.8
CH09-16ch	31.0	43.8	24.1	98.2	54.0	15.9	15.9
CH09-16fs	32.7	42.0	28.2	88.3	55.5	15.4	28.4
CH09-19ch-1	29.2	45.9	23.6	99.6	58.6	14.3	15.4
CH09-19ch-2	28.9	46.3	29.6	85.5	54.9	15.6	15.7
CH09-19fs	30.4	44.5	28.6	87.4	53.8	16.0	27.0
CH09-23ch	27.2	48.7	22.7	102.5	53.8	16.0	18.4
CH09-23fs	24.0	53.8	26.3	92.7	25.6	42.3	29.7
CH09-40ch	40.1	35.8	42.8	66.5	59.0	14.2	24.3
CH09-40fs	25.0	52.0	34.7	76.7	51.8	16.8	25.7
CH09-41ch	39.4	36.2	43.7	65.5	56.2	15.1	31.3
CH09-41fs	34.6	40.2	43.2	66.1	62.2	13.2	34.6
CH09-43fs	36.5	38.5	45.5	63.8	23.0	48.6	48.0
CH09-44ch	38.1	37.2	41.2	68.2	24.3	45.3	33.1
CH09-44fs	40.3	35.6	40.9	68.6	57.1	14.8	29.6
CH09-46fs	25.9	50.6	30.7	83.3	51.2	17.1	24.0
CH09-50ch	39.0	36.6	41.8	67.5	74.9	10.4	43.2
CH09-50fs	39.8	36.0	46.3	63.1	68.6	11.7	36.8
CH09-55fs	37.0	38.1	47.6	61.8	57.6	14.6	37.3
CH09-57ch	35.8	39.1	39.0	70.8	63.0	13.0	26.3
CH09-57fs	38.4	37.0	50.8	59.1	72.6	10.8	37.2
CH09-58ch	39.8	36.0	39.9	69.7	61.4	13.5	26.6
CH09-58fs	39.9	35.9	41.7	67.7	59.3	14.1	32.9
CH09-68ch	30.5	44.4	30.4	83.9	41.3	22.6	21.6
CH09-68fs	34.9	39.9	46.5	62.9	56.6	15.0	31.3
HD09-11b	30.4	44.5	59.8	53.0	65.4	12.4	41.8
HD09-27	26.8	49.2	26.5	92.2	30.1	34.3	18.8
HD09-28	30.4	44.5	29.6	85.4	32.5	30.9	16.3
HD09-29	35.6	39.3	54.0	56.8	54.2	15.9	25.2

Table 3. Average Equilibrium Temperatures in °C Calculated from 2-Pyroxene Geothermometry^a

Sample	Brey and Kohler (1990)	Taylor (1998)	Putirka (2008)	Average Temperature
CH09-08A	708	825	846	793
CH09-11fs	716	833	841	797
CH09-13fs	698	823	835	785
CH09-23fs	727	848	846	807
CH09-40fs	696	809	841	782
CH09-46fs	709	821	853	794
CH09-55fs	700	819	839	786
CH09-68fs	690	803	842	778

^aCalculated using a pressure of 0.8 GPa

Table 4. Monophase Strain Rates ($\dot{\epsilon}$) and Effective Viscosities (η) for Each Major Phase

Sample	Quartz $\dot{\epsilon}$ (s^{-1})	Quartz η (Pa.s)	Plagioclase $\dot{\epsilon}$ (s^{-1})	Plagioclase η (Pa.s)	Enstatite $\dot{\epsilon}$ (s^{-1})	Enstatite η (Pa.s)	Diopside $\dot{\epsilon}$ (s^{-1})	Diopside η (Pa.s)
AF09-3A	6.4E-12	3.5E+18	2.4E-14	1.2E+21	7.0E-18	9.8E+23	4.9E-15	4.5E+21
AF09-12	7.6E-12	3.1E+18	4.1E-14	8.6E+20	1.0E-17	7.6E+23	6.4E-15	3.6E+21
AF09-15	2.4E-12	7.4E+18	4.0E-14	8.8E+20	1.6E-16	1.2E+23	9.8E-16	1.8E+22
AF09-19	7.9E-12	3.0E+18	2.3E-14	1.3E+21	4.2E-18	1.4E+24	6.8E-15	3.4E+21
CH09-08A	1.1E-11	2.4E+18	2.8E-14	1.2E+21	4.5E-18	1.4E+24	1.0E-14	2.6E+21
CH09-08B	1.3E-11	2.1E+18	5.1E-14	8.1E+20	4.9E-18	1.3E+24	1.3E-14	2.0E+21
CH09-08C	1.1E-11	2.4E+18	4.5E-14	8.9E+20	7.2E-18	1.0E+24	1.0E-14	2.5E+21
CH09-09A	7.2E-12	3.2E+18	5.5E-14	7.8E+20	6.8E-18	1.1E+24	5.4E-15	4.3E+21
CH09-09B	1.2E-11	2.3E+18	5.0E-14	8.2E+20	3.8E-18	1.6E+24	1.2E-14	2.2E+21
CH09-11ch	7.3E-12	3.2E+18	1.3E-13	4.0E+20	4.7E-17	2.8E+23	6.1E-15	3.8E+21
CH09-11fs	8.4E-12	2.8E+18	8.8E-14	5.2E+20	1.1E-17	7.4E+23	7.6E-15	3.2E+21
CH09-13ch-1	6.7E-12	3.5E+18	4.5E-14	1.1E+21	5.4E-18	1.5E+24	3.9E-15	6.0E+21
CH09-13ch-2	3.2E-12	6.1E+18	4.7E-14	1.0E+21	5.4E-18	1.5E+24	1.2E-15	1.6E+22
CH09-13fs	5.3E-12	4.2E+18	3.1E-14	1.4E+21	5.3E-18	1.5E+24	2.7E-15	8.1E+21
CH09-16ch	5.0E-12	4.4E+18	4.9E-14	1.0E+21	5.1E-18	1.6E+24	2.5E-15	8.8E+21
CH09-16fs	4.3E-12	4.9E+18	3.5E-14	1.2E+21	4.6E-18	1.7E+24	1.9E-15	1.1E+22
CH09-19ch-1	7.2E-12	3.2E+18	1.2E-13	4.3E+20	8.0E-18	8.9E+23	5.9E-15	3.9E+21
CH09-19ch-2	7.5E-12	3.1E+18	7.3E-14	5.8E+20	1.0E-17	7.6E+23	6.3E-15	3.7E+21
CH09-19fs	6.4E-12	3.5E+18	7.8E-14	5.6E+20	1.1E-17	7.2E+23	4.8E-15	4.6E+21
CH09-23ch	1.0E-11	2.3E+18	2.5E-13	2.1E+20	2.1E-17	3.9E+23	1.4E-14	1.8E+21
CH09-23fs	1.6E-11	1.7E+18	1.8E-13	2.5E+20	1.7E-17	4.3E+23	2.6E-14	1.0E+21
CH09-40ch	2.1E-12	8.4E+18	1.2E-14	2.7E+21	3.0E-18	2.4E+24	5.8E-16	3.1E+22
CH09-40fs	9.6E-12	2.7E+18	1.9E-14	2.0E+21	4.9E-18	1.7E+24	6.6E+15	4.0E+21
CH09-41ch	2.3E-12	8.0E+18	1.2E-14	2.8E+21	3.6E-18	2.1E+24	6.3E-16	2.9E+22
CH09-41fs	3.4E-12	5.9E+18	1.2E-14	2.7E+21	2.5E-18	2.7E+24	1.2E-15	1.6E+22
CH09-43fs	2.9E-12	6.7E+18	1.1E-14	2.9E+21	2.0E-18	3.0E+24	9.4E-16	2.0E+22
CH09-44ch	2.5E-12	7.4E+18	1.3E-14	2.6E+21	2.8E-18	2.5E+24	7.5E-16	2.5E+22
CH09-44fs	2.1E-12	8.5E+18	1.3E-14	2.6E+21	3.4E-18	2.2E+24	5.7E-16	3.1E+22
CH09-46fs	1.0E-11	2.5E+18	5.5E-14	7.5E+20	1.1E-17	7.7E+23	9.6E-15	2.6E+21
CH09-50ch	2.5E-12	7.4E+18	1.7E-14	2.0E+21	1.6E-18	3.3E+24	8.1E-16	2.2E+22
CH09-50fs	2.3E-12	7.8E+18	1.4E-14	2.3E+21	2.2E-18	2.7E+24	7.3E-16	2.5E+22
CH09-55fs	2.9E-12	6.5E+18	1.3E-14	2.4E+21	4.3E-18	1.7E+24	1.1E-15	1.8E+22
CH09-57ch	3.3E-12	6.0E+18	2.0E-14	1.8E+21	3.0E-18	2.0E+24	1.3E-15	1.5E+22
CH09-57fs	2.6E-12	7.1E+18	1.1E-14	2.6E+21	1.8E-18	3.1E+24	8.7E-16	2.1E+22
CH09-58ch	2.3E-12	7.8E+18	1.9E-14	1.9E+21	3.3E-18	2.0E+24	7.3E-16	2.5E+22
CH09-58fs	2.3E-12	7.8E+18	1.7E-14	2.0E+21	3.8E-18	1.9E+24	7.2E-16	2.5E+22
CH09-68ch	4.8E-12	4.6E+18	1.9E-14	2.3E+21	9.0E-18	1.3E+24	1.9E-15	1.1E+22
CH09-68fs	3.1E-12	6.4E+18	7.8E-15	4.0E+21	2.7E-18	2.8E+24	9.8E-16	2.0E+22
HD09-11b	4.8E-12	4.6E+18	4.7E-15	5.7E+21	1.6E-18	4.0E+24	2.0E-15	1.1E+22
HD09-27	7.2E-12	3.4E+18	2.5E-14	1.9E+21	3.0E-17	5.7E+23	3.8E-15	6.5E+21
HD09-28	4.8E-12	4.6E+18	2.0E-14	2.2E+21	2.2E-17	7.0E+23	2.0E-15	1.1E+22
HD09-29	2.9E-12	6.7E+18	5.8E-15	4.9E+21	3.2E-18	2.5E+24	8.8E-16	2.2E+22

Table 5. Polyphase Effective Viscosities (η) for Every Sample^{a,b} from $\dot{\epsilon} = 10^{-18}$ - 10^{-10} s^{-1}

Sample	$\dot{\epsilon} = 10^{-10} \text{ s}^{-1}$	$\dot{\epsilon} = 10^{-11} \text{ s}^{-1}$	$\dot{\epsilon} = 10^{-12} \text{ s}^{-1}$	$\dot{\epsilon} = 10^{-13} \text{ s}^{-1}$	$\dot{\epsilon} = 10^{-14} \text{ s}^{-1}$
AF09-3A	5.2E+23	2.0E+22	7.8E+20	3.0E+19	1.2E+18
AF09-12	5.2E+23	2.0E+22	7.9E+20	3.0E+19	1.2E+18
AF09-15*	2.9E+23	9.4E+21	3.1E+20	1.0E+19	3.3E+17
AF09-19	2.1E+24	7.5E+22	2.7E+21	9.4E+19	3.4E+18
CH09-08A	1.9E+24	7.2E+22	2.7E+21	1.0E+20	3.9E+18
CH09-08B	1.5E+24	5.7E+22	2.2E+21	8.1E+19	3.1E+18
CH09-08C	1.3E+24	4.9E+22	1.9E+21	6.9E+19	2.6E+18
CH09-09A	6.4E+23	2.5E+22	9.8E+20	3.8E+19	1.5E+18
CH09-09B	1.7E+24	6.6E+22	2.5E+21	9.5E+19	3.6E+18
CH09-11ch*	4.7E+22	1.8E+22	6.8E+20	2.6E+19	9.8E+19
CH09-11fs	1.1E+24	4.2E+22	1.6E+21	5.9E+19	2.2E+18
CH09-13ch-1*	7.8E+23	3.2E+22	1.3E+21	5.5E+19	2.3E+18
CH09-13ch-2	5.9E+23	2.3E+22	9.2E+20	3.6E+19	1.4E+18
CH09-13fs	1.3E+24	4.9E+22	1.9E+21	7.5E+19	2.9E+18
CH09-16ch*	6.2E+23	2.5E+22	9.8E+20	3.9E+19	1.5E+18
CH09-16fs	9.0E+23	3.6E+22	1.5E+21	5.9E+19	2.4E+18
CH09-19ch-1*	6.7E+23	2.8E+22	1.2E+21	5.2E+19	2.2E+18
CH09-19ch-2	6.7E+25	2.8E+22	1.2E+21	4.9E+19	2.1E+18
CH09-19fs	7.8E+23	3.0E+22	1.2E+21	4.4E+19	1.7E+18
CH09-23ch*	4.9E+23	1.9E+22	7.6E+20	3.0E+19	1.2E+18
CH09-23fs	1.3E+24	4.7E+22	1.7E+21	6.4E+19	2.4E+18
CH09-40ch*	5.8E+23	2.2E+22	8.6E+20	3.3E+19	1.3E+18
CH09-40fs	1.8E+24	6.9E+22	2.7E+21	1.0E+20	4.0E+18
CH09-41ch	5.9E+23	2.2E+22	8.2E+20	3.1E+19	1.1E+18
CH09-41fs	1.4E+24	5.4E+22	2.1E+21	8.4E+19	3.3E+18
CH09-43fs*	1.8E+24	6.7E+02	2.5E+21	9.2E+19	3.4E+18
CH09-44ch	1.3E+24	5.2E+22	2.1E+21	8.6E+19	3.5E+18
CH09-44fs	7.0E+23	2.8E+22	1.1E+21	4.3E+19	1.7E+18
CH09-46fs	7.8E+23	3.2E+22	1.3E+21	5.3E+19	2.2E+18
CH09-50ch*	6.4E+23	2.5E+22	9.4E+20	3.6E+19	1.4E+18
CH09-50fs	7.6E+23	3.0E+22	1.2E+21	4.8E+19	1.9E+18
CH09-55fs	9.2E+23	3.7E+22	1.5E+21	5.8E+19	2.3E+18
CH09-57ch*	6.7E+23	2.7E+22	1.1E+21	4.4E+19	1.8E+18
CH09-57fs	1.2E+24	4.8E+22	1.9E+21	7.7E+19	3.1E+18
CH09-58ch*	6.4E+23	2.5E+22	9.8E+20	3.9E+19	1.5E+18
CH09-58fs*	6.6E+23	2.4E+22	9.1E+20	3.4E+19	1.1E+18
CH09-68ch	5.9E+23	2.3E+22	8.6E+20	3.3E+19	1.3E+18
CH09-68fs	1.4E+24	5.8E+22	2.5E+21	1.1E+20	4.5E+18
HD09-11b	1.8E+24	7.6E+22	3.1E+21	1.3E+20	5.4E+18
HD09-27	3.3E+23	1.1E+22	3.6E+20	1.2E+19	3.9E+17
HD09-28	4.1E+23	1.4E+22	5.1E+20	1.8E+19	6.3E+17
HD09-29	9.0E+23	3.9E+22	1.7E+21	7.4E+19	3.2E+18

^aUsing the Minimized Geometric Power Model proposed by *Huet et al.*, (2014)

^bCalculated at a temperature of ca. 800°C

*Samples denoted with an * contain greater than 20% of potassium feldspar which could not be included in the mixing models for calculation of bulk viscosity

Table 6. Polyphase Effective Viscosities (η) for Select Samples^{a,b} from $\dot{\epsilon} = 10^{-18}$ - 10^{-10} s^{-1}

Sample	$\dot{\epsilon} = 10^{-18} \text{ s}^{-1}$	$\dot{\epsilon} = 10^{-16} \text{ s}^{-1}$	$\dot{\epsilon} = 10^{-14} \text{ s}^{-1}$	$\dot{\epsilon} = 10^{-12} \text{ s}^{-1}$	$\dot{\epsilon} = 10^{-10} \text{ s}^{-1}$
CH09-08A	9.4E+23	3.3E+22	1.1E+21	3.3E+19	1.1E+18
CH09-09A	7.9E+23	3.7E+22	1.7E+21	7.7E+19	3.3E+18
CH09-11ch*	4.7E+23	1.9E+22	8.2E+20	3.5E+19	1.5E+18
CH09-11fs	7.9E+23	3.8E+22	1.7E+21	7.5E+19	3.2E+18
CH09-13ch-1*	7.5E+23	3.3E+22	1.5E+21	7.5E+19	3.5E+18
CH09-13fs	7.5E+23	3.2E+22	1.3E+21	5.3E+19	2.1E+18
CH09-16ch*	5.6E+23	2.2E+22	1.0E+21	4.5E+19	2.0E+18
CH09-16fs	6.3E+23	2.7E+22	1.2E+21	5.0E+19	2.2E+18
CH09-19ch-1*	8.2E+23	4.0E+22	1.9E+21	9.4E+19	4.5E+18
CH09-19fs	8.0E+23	4.2E+22	1.9E+21	7.7E+19	3.1E+18
CH09-40fs	1.3E+24	6.3E+22	2.8E+21	1.2E+20	5.0E+18
CH09-41ch	1.3E+24	5.6E+22	2.5E+21	1.1E+20	4.5E+18
CH09-41fs	1.4E+24	6.0E+22	2.4E+21	8.9E+19	3.5E+18
CH09-68ch	6.0E+23	2.2E+22	8.4E+20	3.2E+19	1.3E+18
CH09-68fs	1.5E+24	6.7E+22	3.1E+21	1.3E+20	5.0E+18

^aUsing the Minimized Geometric Power Model proposed by *Huet et al.*, (2014)^bCalculated at a temperature of ca. 800°C

*Samples denoted with an * contain greater than 20% of potassium feldspar which could not be included in the mixing models for calculation of bulk viscosity

Appendix A.

Sample Localities

Table of All Sample Names and GPS Coordinates

Table A. All Sample Localities. WGS84 database, UTM, Zone 53K South

Sample	Northing	Easting
AF09-3A	7404661	317170
AF09-12	7403027	314209
AF09-15	7402906	313308
AF09-19	7403660	313713
CH09-08A	7403338	320367
CH09-08B	7403338	320367
CH09-08C	7403338	320367
CH09-09A	7403238	319981
CH09-09B	7403238	319981
CH09-11ch	7402809	318877
CH09-11fs	7402809	318877
CH09-13ch-1	7402498	324023
CH09-13ch-2	7402498	324023
CH09-13fs	7402498	324023
CH09-16ch	7402386	323602
CH09-16fs	7402386	323602
CH09-19ch-1	7402359	319565
CH09-19ch-2	7402359	319565
CH09-19fs	7402359	319565
CH09-23ch	7402707	320091
CH09-23fs	7402707	320091
CH09-40ch	7403818	321002
CH09-40fs	7403818	321002
CH09-41ch	7403786	320848
CH09-41fs	7403786	320848
CH09-43fs	7403571	320770
CH09-44ch	7403483	320616
CH09-44fs	7403483	320616
CH09-46fs	n/a	n/a
CH09-50ch	7403006	322989
CH09-50fs	7403006	322989
CH09-55fs	7402320	322381
CH09-57ch	7402471	322522
CH09-57fs	7402471	322522
CH09-58ch	7402651	322595
CH09-58fs	7402651	322595
CH09-68ch	7400779	323734
CH09-68fs	7400779	323734
HD09-11b	7399345	325335
HD09-27	7400095	324619
HD09-28	7400065	324576
HD09-29	7400104	324521

Appendix B.

Analytical Methods

Electron Backscatter Diffraction Collection and Processing,

Electron Microprobe Collection and Processing, Huet et al.

Mixing Model Rheology Calculations, Power-Law Creep

Toolbox Rheology Calculations

Electron Backscatter Diffraction Collection and Processing

Full thin-section textural maps were acquired for all samples using a Tescan Mira3 variable-pressure field emission scanning electron microscope equipped with an Oxford Instruments Symmetry electron backscatter diffraction (EBSD) detector and AZtecHKL acquisition software housed within the Department of Earth and Environmental Sciences at Boston College. Prior to textural EBSD analysis, thin sections were coated in carbon to avoid charging particles and full backscatter electron (BSE) maps were made. Samples were analyzed at operating conditions of 50 nA for beam currents and an accelerating voltage of 25 kV. Thin sections were set to a working distance of 20.5 mm and tilted to an angle of 70° for EBSD work. Minerals selected for indexing from AZtec's HKL database were plagioclase feldspar, quartz, orthoclase, enstatite, diopside, hornblende, biotite, pyrope, magnetite, and illmenite. An electron image of the sample was scanned into the AZtec software using a scan size of 1024 and a dwell time of 15. Patterns were optimized with the settings of a binning mode of 4x4, gain values of 2, and frame averaging of 2 frames. Solutions were optimized by adding a solution of a major constitute mineral that had a large number of Kikuchi bands (>8) and a low MAD (<0.8) under the setting Optimized-EBSD. Coordinates chosen for EBSD map data were selected as the uppermost and lowermost corners of the thin section such that the largest area of the thin section would be represented and all major features, such as quartz ribbons and plagioclase porphyroclasts, were included. In order to acquire high resolution data sets with a large amount of crystallographic orientation data, textural maps were produced using a field of view of 775 μm , a step size of 5 μm , a 20% overlap, were generally rectangular-shaped, and ranged between 1200-2000 fields.

Raw EBSD data for each textural map was exported using the Oxford Instruments AZtecHKL software package. CPR and CRC files, a summary doc file, PNG files of the EBSD map, and raw lower hemisphere, equal area, directional crystallographic preferred orientation (CPO) pole figures for quartz, plagioclase feldspar, enstatite, and diopside were exported for each sample. Noise reduction of the exported CPR file was processed in Channel5's Project Manager Tango to eliminate "wild-spike" single solutions.

Post-data acquisition processing was done in the freely available MTEX toolbox (version 5.1.1) (<https://mtex-toolbox.github.io>) for EBSD textural analysis in Matlab using the following steps:

1. The noise-reduced CPR file for each sample was imported into Matlab using the Import Wizard. Because the SEM coordinate system is different than the EBSD coordinate system, rotation corrections were also performed.
2. EBSD data were imported into Matlab as spatially referenced pixels of crystallographic orientations.
3. A grain reconstruction algorithm was performed to calculate a grain set from pixels of individual orientations. Grains were defined as any collection of orientation pixels that have $<10^\circ$ misorientation relative to neighboring pixels and grain diameters greater than 3x the step size used in acquisition.

4. “Bad” data, such as poor solutions, defined by having a MAD >0.8, non-indexed pixels, and one-neighbor grains, were removed from the data set in MTEX. Nonindexed regions (i.e. holes) in the dataset were filled using Voronoi decomposition functions, and the refined datasets were used to calculate and plot all quantifiable aspects of the rock microstructure and texture.

5. CPOs were plotted for each major phase (quartz, plagioclase, enstatite, and diopside) as one point per grain based on the calculated mean orientation of each unique grain. In order to correct for the fact that some orientations are statistically favored over others, crystallographic preferred orientations were plotted as orientation distribution functions (ODFs), which recontours the data based on crystal symmetry (*Prior et al.*, 1999). The M-index proposed by Skemer et al. (2005) and the BA-index proposed by Mainprice et al. (2014) were also calculated. ODF figures were exported.

6. Grain size histograms for each major phase, based on the definition stated in Step 3, were plotted and exported. Grains bordering the edge of the thin section were excluded, as their grain size does not represent the true size of phases at the border of the maps. A correction factor of 1.2 was applied to the mean grain sizes in order to account for the inaccurate representation of assuming each grain was cut to show its maximum diameter. Histograms were plotted for diameter vs frequency and for equivalent-area diameter vs frequency, which calculates the grain size based on a perfect circle of equivalent area.

7. Internal misorientation axes of all major phases were calculated, plotted, and exported as inverse pole figures within the crystal reference frame. Misorientations were defined as the angle it takes to rotate two pixels into parallelism, and lies between 2° and 10° for subgrains.

Electron Microprobe Collection and Processing

Fe-Mg two-pyroxene exchange thermometry was conducted through electron microprobe compositional analysis of neighboring enstatite and diopside grains in select gabbroic samples. Eight thin sections were chosen for electron microprobe analysis. Compositional data were acquired using a Cameca SX50 housed in the Department of Geoscience at the University of Wisconsin-Madison at operating conditions of 20 nA for beam currents and an accelerating voltage of 15 kV. Prior to probe work, samples were carbon coated. Standards were selected prior to chemical analysis for the elements Fe, Mg, Ca, Al, Si, Na, K, Ti, Cr, and Mn. Electron spot size was on the order of 1-2 μm during data acquisition.

The exchange of Fe and Mg between orthopyroxene (e.g. enstatite) and clinopyroxene (e.g. diopside) is sensitive to changes in temperature. Previously derived geothermometers work to quantify equilibrium temperatures of touching neighboring pyroxene pairs that are in equilibrium with each other, based on the relative amounts of different elements within both of the grains (presumably on their touching edges). The compositions of each pyroxene pair measured was on the edge of neighboring grains that show no signs of any retrograde metamorphism, such as the presence of hornblende rims, to ensure the pyroxene compositions are the closest to peak metamorphic conditions.

Compositional data was collected in at least three distinct locations in each thin section to check for compositional heterogeneities. For each location, at least three different neighboring enstatite and diopside pairs were analyzed. Three different spots were selected for each individual grain analysis in order to decrease error. During post-analysis processing, the spot that had the compositional values closest to the average of the three points was selected for thermometry calculations.

Raw electron microprobe data was given as an Excel spreadsheet with the oxide weight percent of all measured elements and weight totals. Any totals that were not between 98.5-101% were rejected for this analysis. Orthopyroxene and clinopyroxene compositions were normalized based on their molecular weight and mole proportions. These values were then converted to temperatures using the derived two-pyroxene geothermometers by Brey and Kohler (1990), Taylor (1998), and Putirka (2008).

Huet et al. Mixing Model Rheology Calculations

The Huet et al. mixing model (see Eq. 3 in the main text) calculates bulk viscosity for a sample from the phase proportions and flow laws of the individual phases. The monophase effective viscosities are a function of strain rate, temperature, water content, and the flow law variables A (preexponential factor), Q (activation energy), and n (stress exponent) for each phase (Table 3). The temperature used for each sample was that determined by the geothermometry calculations, the water content was ignored because the samples used in this study are assumed to be dry. The modal percentage of each phase was determined through EBSD post-processing in the MTEX toolbox of Matlab, and the mode of each major phase was normalized assuming that quartz, plagioclase, enstatite,

and diopside composed 100% of the sample. The bulk viscosity was calculated for each sample for strain rates of 10^{-18} s^{-1} , 10^{-16} s^{-1} , 10^{-14} s^{-1} , 10^{-12} s^{-1} , and 10^{-10} s^{-1} using the methodology of Shinevar et al. (2015). Once the bulk viscosity was calculated, its value was plotted against its corresponding strain rate and compared to the expected viscosities of each monophase mineral (e.g., quartz, plagioclase, etc.) at the same strain rate and temperature conditions.

Power-Law Creep Toolbox Rheology Calculations

The Power-Law Creep Toolbox takes an image of a rock microstructure and calculates its bulk rheology based on the stiffness tensors of the minerals in it and the Asymptotic Expansion Homogenization (AEH) method. To reduce the run time of the toolbox, small subsections of select EBSD phase maps were chosen for analysis. The subsections were selected based on their modal phase percentages and phase distributions to ensure they were representative of the whole thin section. The microstructure of major phases in these subsections (quartz, plagioclase, enstatite, and diopside) were traced in Adobe Illustrator and the resulting image was saved as an anti-aliased .png file. The bulk rheology was calculated by the PLC toolbox using the following steps:

1. The .png subsection file was uploaded into the toolbox. Upon loading, the program calculates the percentage of each phase based on the amount of each color in the image.
2. Each color is assigned a phase (e.g. dark blue is quartz). Rheology flow law variables for each phase are defined in SI units using the phase information panel.

3. The analysis parameters, such as the temperature (in Kelvin) and the strain rate ranges, of interest are defined in their respective places in the GUI. For this analysis, the temperature used was that determined through the geothermometry results, and the range of strain rates was 10^{-18} through 10^{-10} , based on the monophasic rheology results and the general consensus of natural geologic strain rates.

4. A finite element mesh is created for the image in order for the AEH analysis to work properly. The user has a choice of how many elements they want the mesh to contain. For this analysis, “many elements” was selected for the mesh creation.

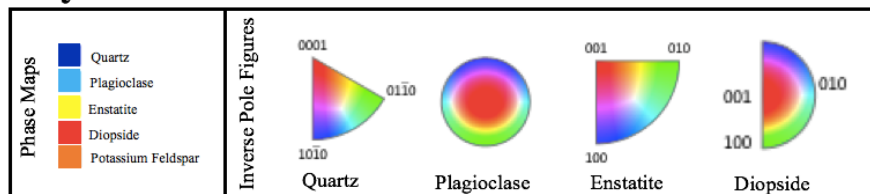
5. The AEH analysis was run. The GUI produces a plot with the bulk rheology determined for the image using AEH in terms of strain rate and differential stress. It plots this against the predicted monophasic rheology of the input phases, based on the defined flow law variables and analysis parameters.

Appendix C.

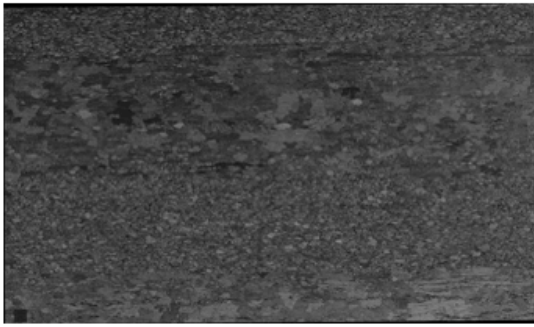
Electron Backscatter Diffraction Maps

Band Contrast, Raw Phase Maps, MATLAB Phase Maps,
IPF-X, IPF-Y, IPF-Z Maps

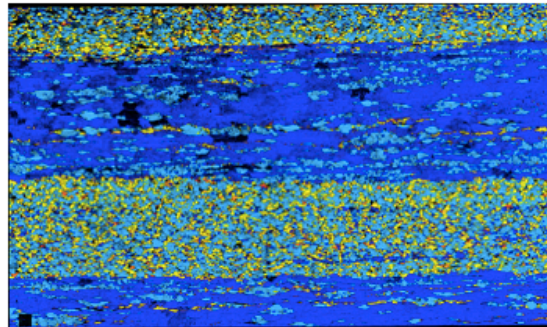
Key:



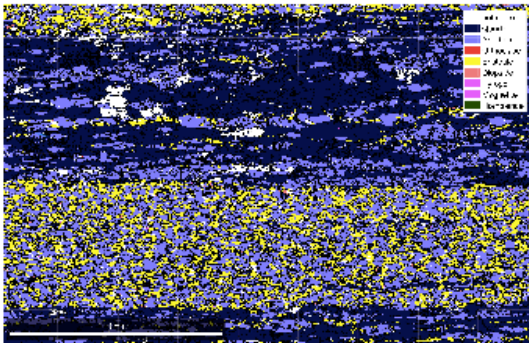
AF09-3A



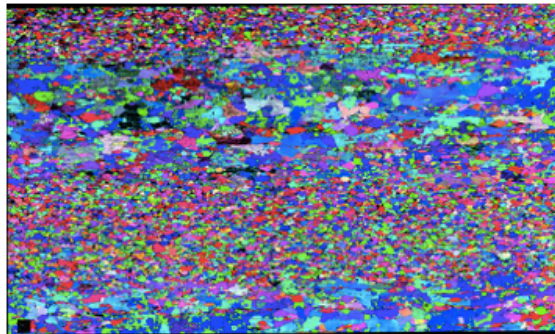
Band contrast



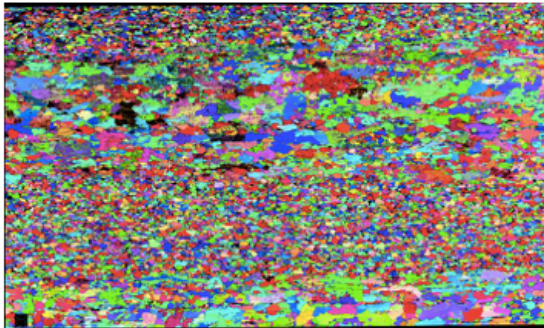
Phase map



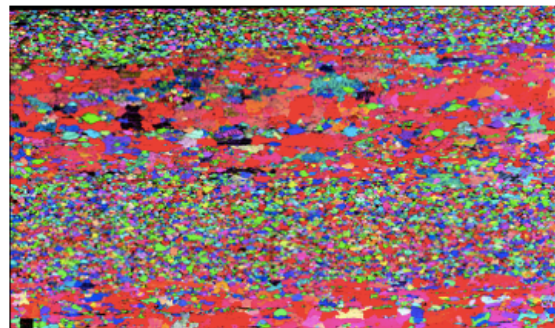
Matlab smoothed phase map



IPF-X map

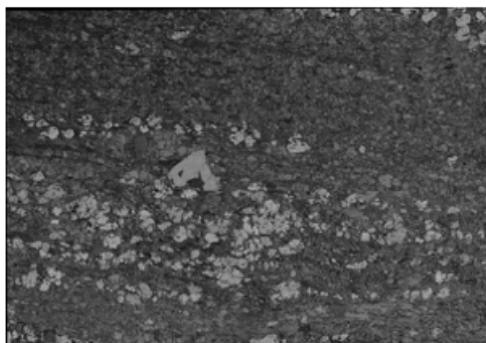


IPF-Y map

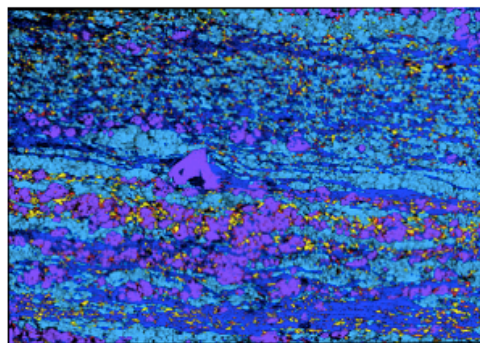


IPF-Z map

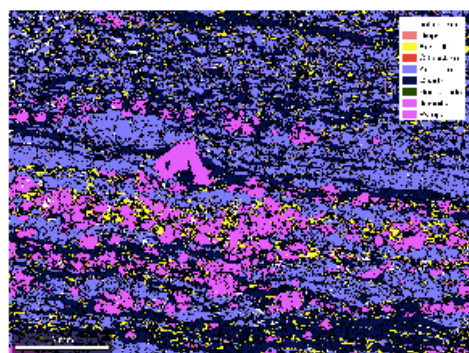
AF09-12



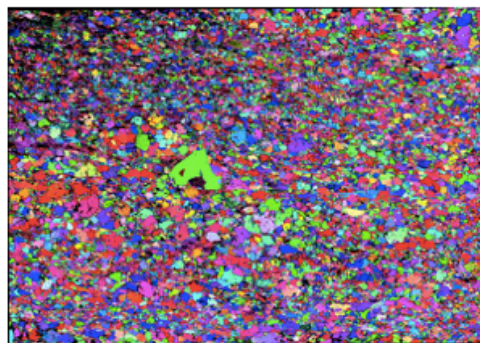
Band contrast



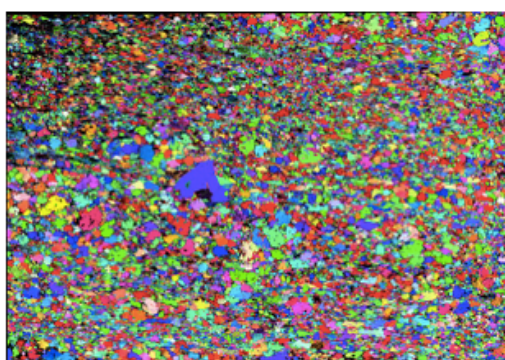
Phase map



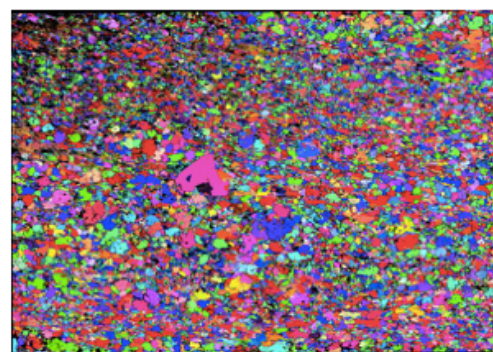
Matlab smoothed phase map



IPF-X map

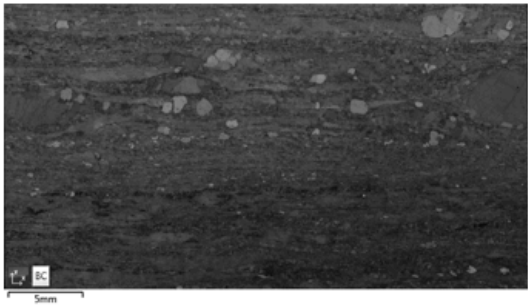


IPF-Y map

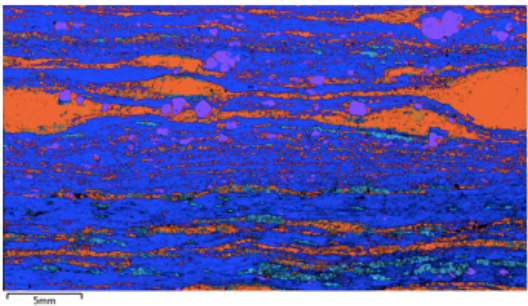


IPF-Z map

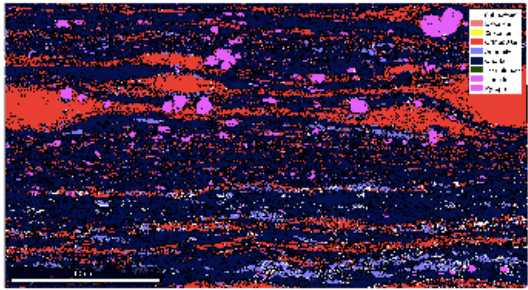
AF09-15



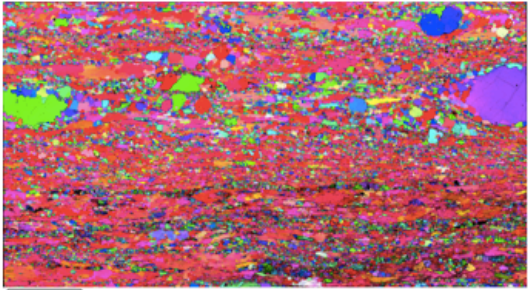
Band contrast



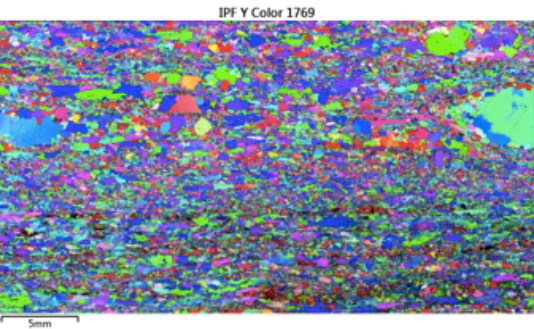
Phase map



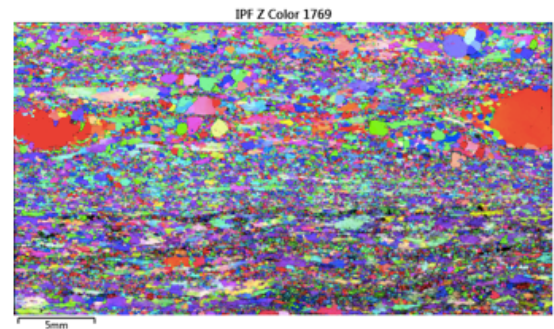
Matlab smoothed phase map



IPF-X map

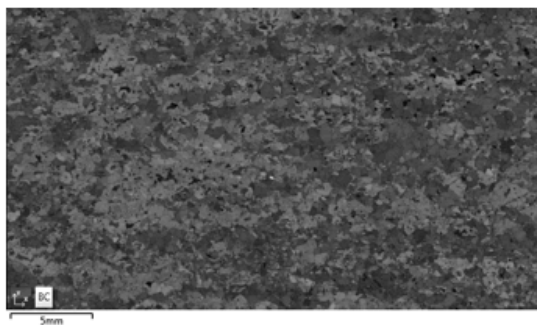


IPF-Y map

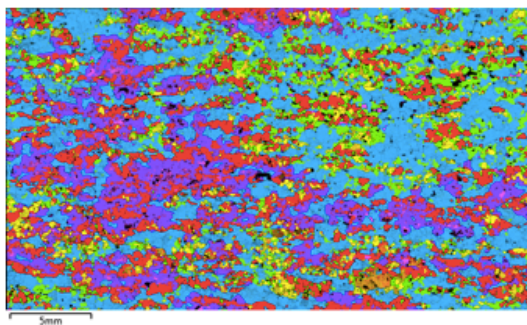


IPF-Z map

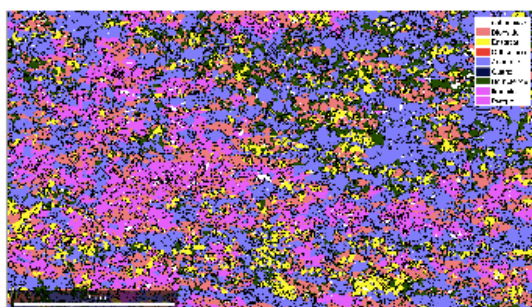
AF09-19



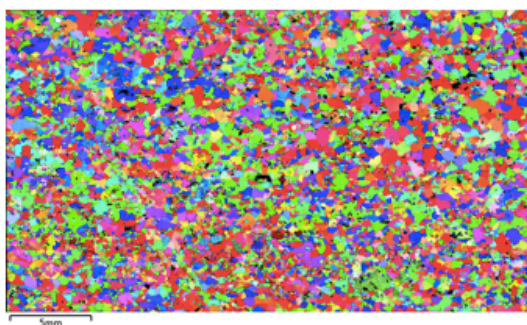
Band contrast



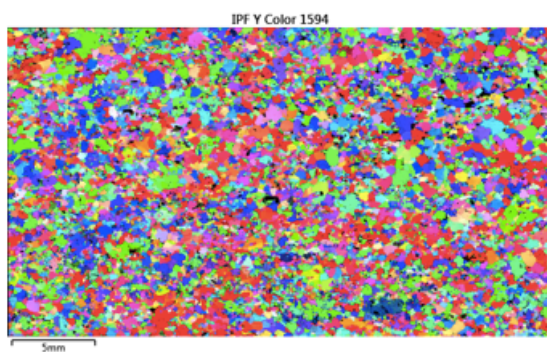
Phase map



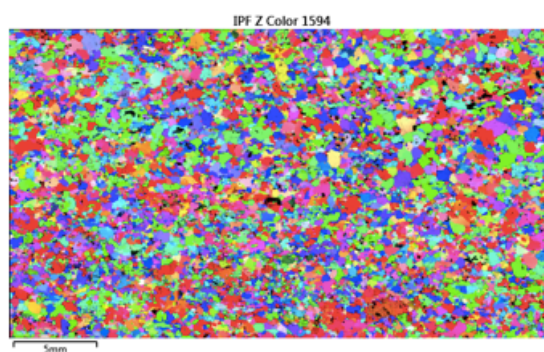
Matlab smoothed phase map



IPF-X map

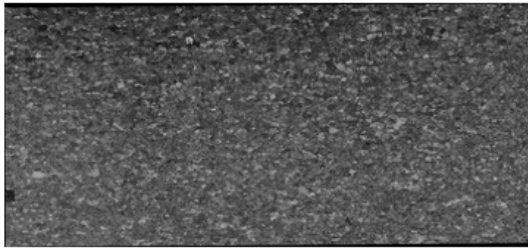


IPF-Y map

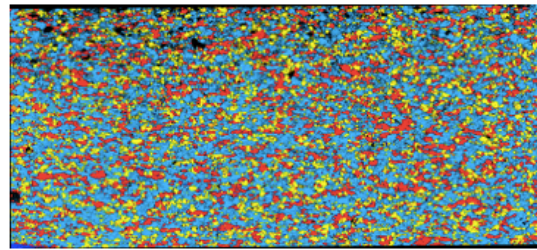


IPF-Z map

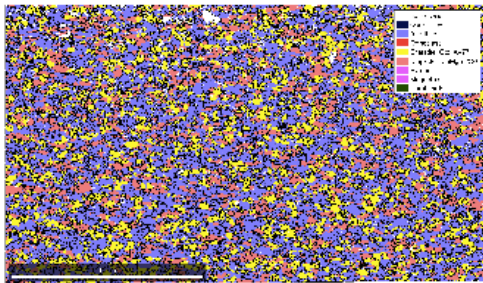
CH09-08A



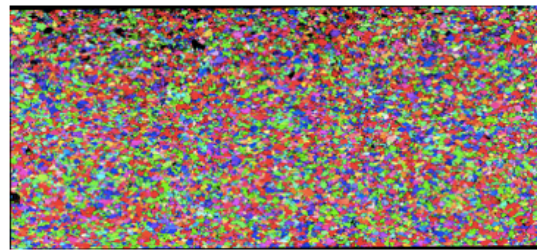
Band contrast



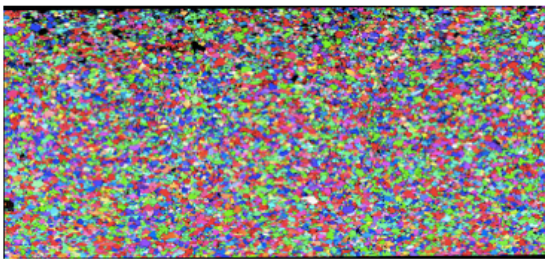
Phase map



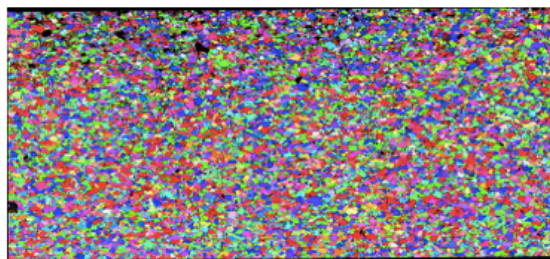
Matlab smoothed phase map



IPF-X map

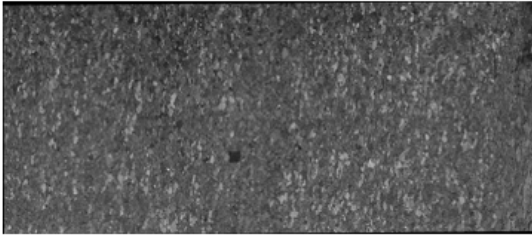


IPF-Y map

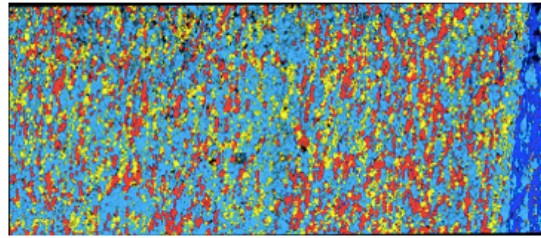


IPF-Z map

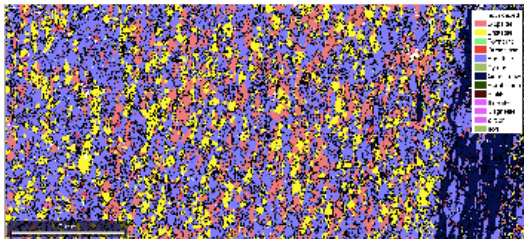
CH09-08B



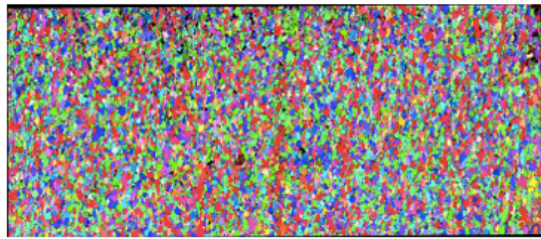
Band contrast



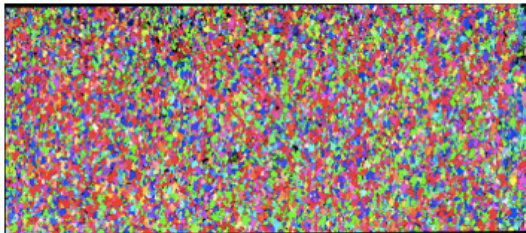
Phase map



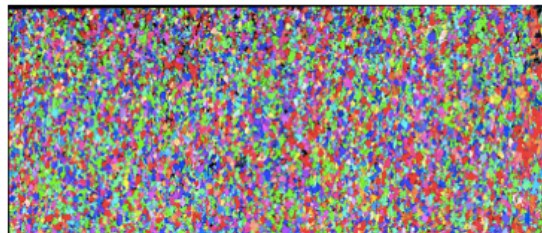
Matlab smoothed phase map



IPF-X map

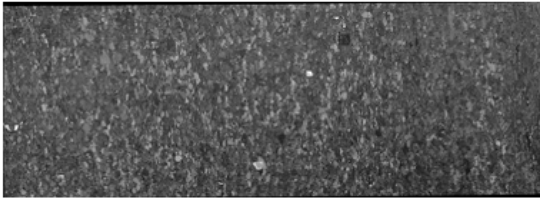


IPF-Y map

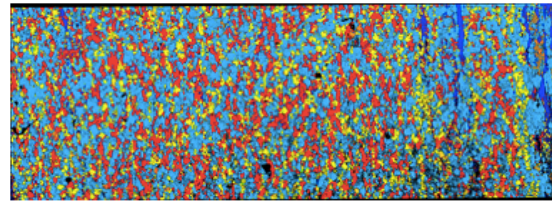


IPF-Z map

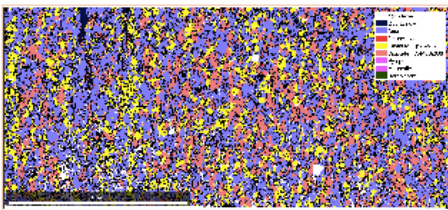
CH09-08C



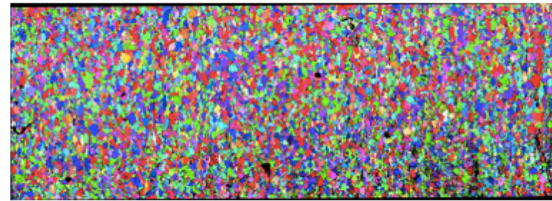
Band contrast



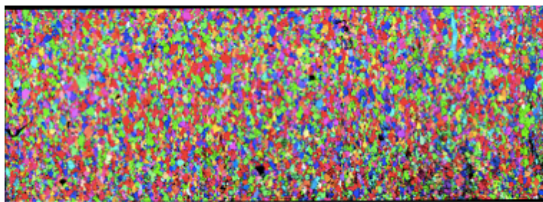
Phase map



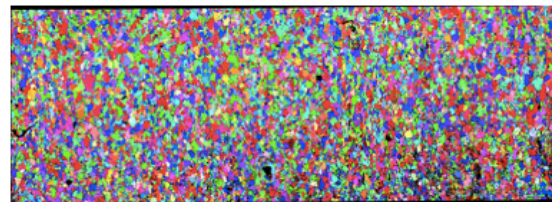
Matlab smoothed phase map



IPF-X map

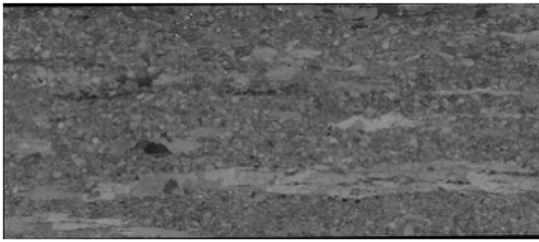


IPF-Y map

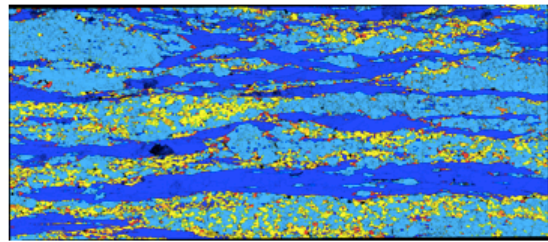


IPF-Z map

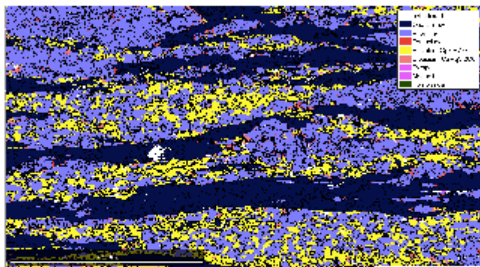
CH09-09A



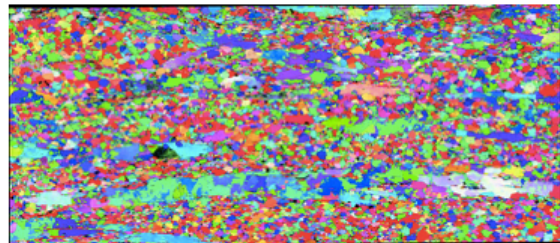
Band contrast



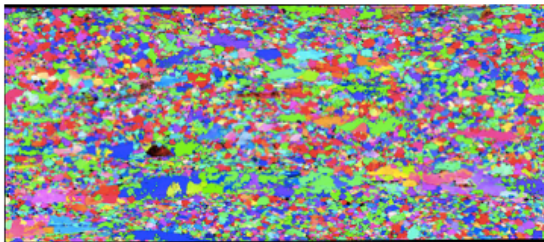
Phase map



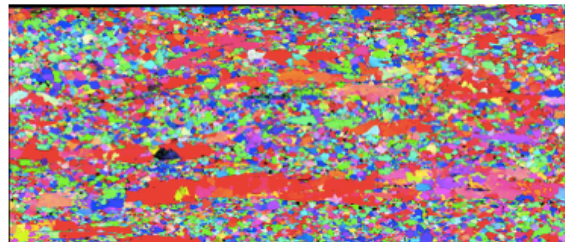
Matlab smoothed phase map



IPF-X map

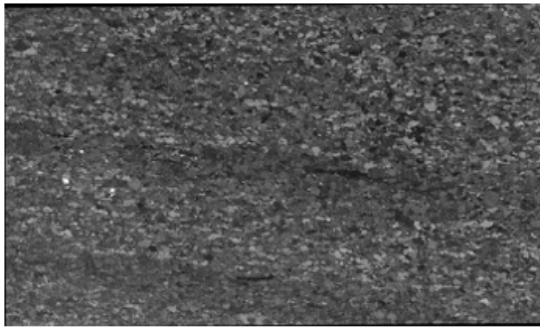


IPF-Y map

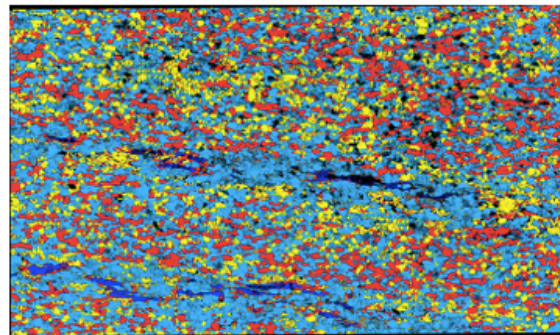


IPF-Z map

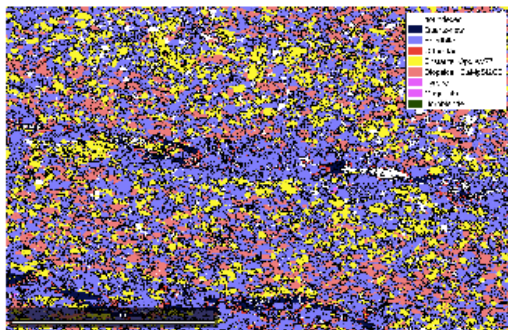
CH09-09B



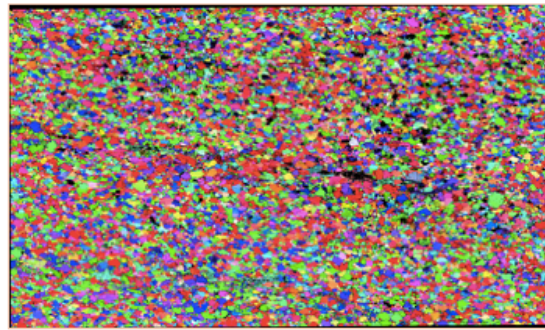
Band contrast



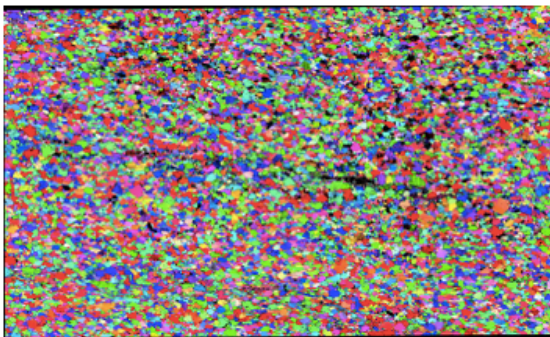
Phase map



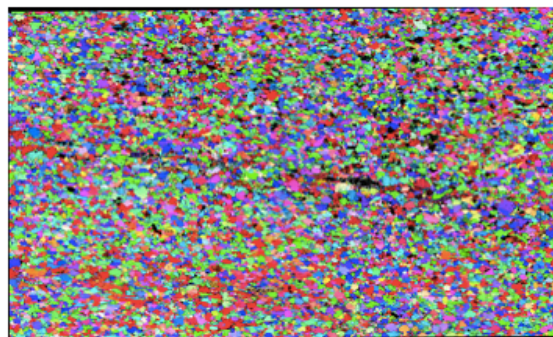
Matlab smoothed phase map



IPF-X map

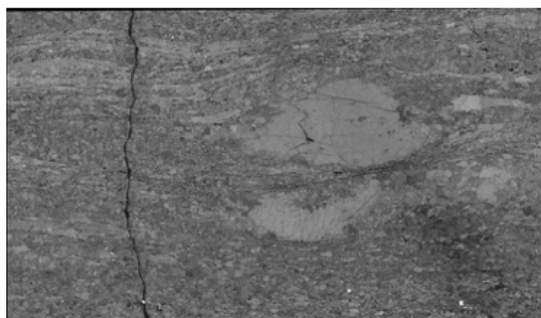


IPF-Y map

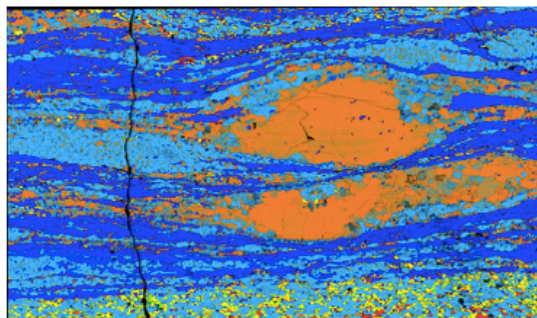


IPF-Z map

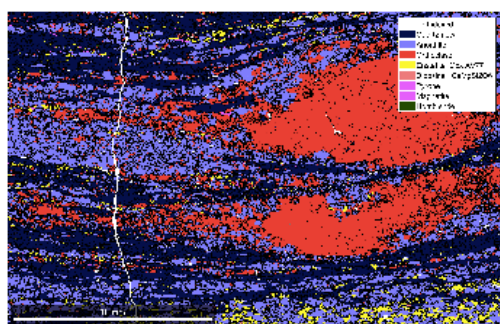
CH09-11ch



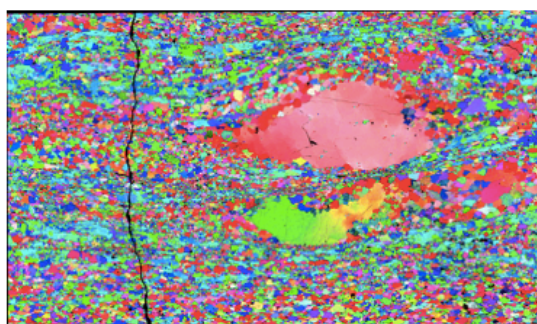
Band contrast



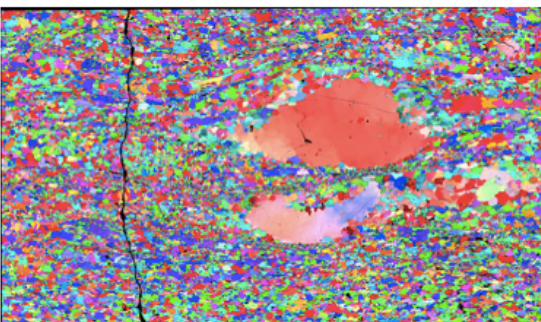
Phase map



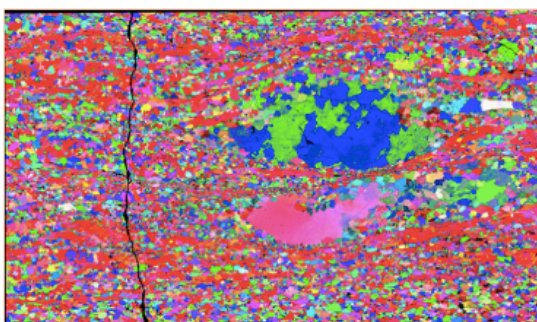
Matlab smoothed phase map



IPF-X map

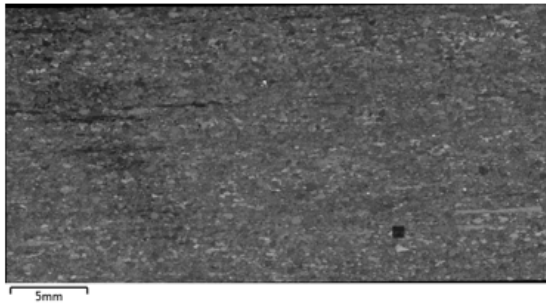


IPF-Y map

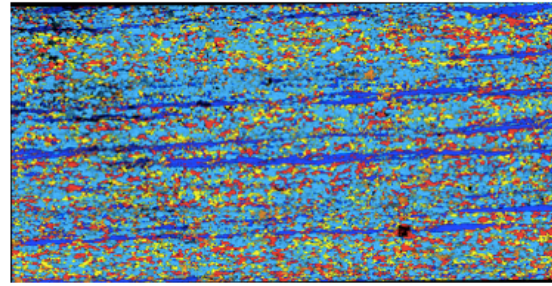


IPF-Z map

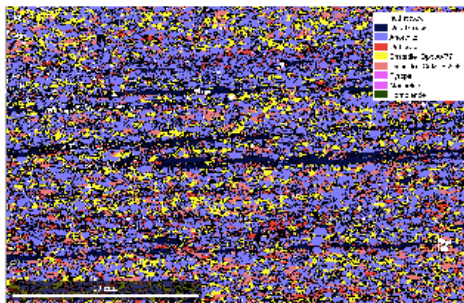
CH09-11fs



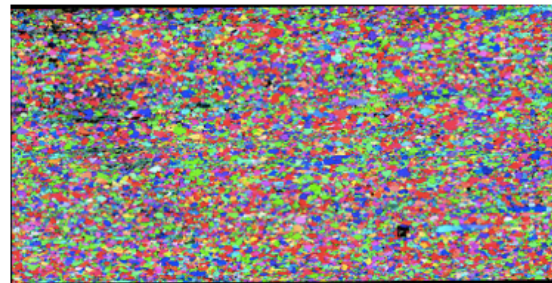
Band contrast



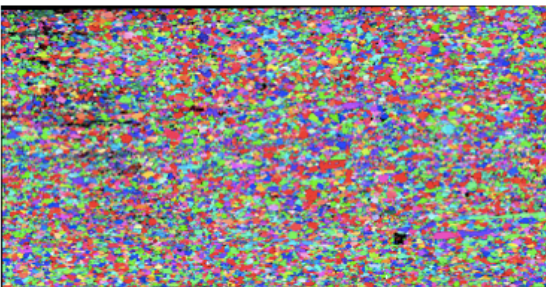
Phase map



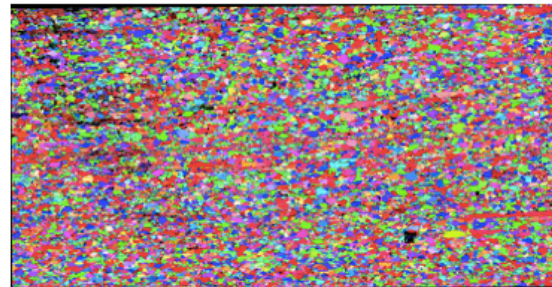
Matlab smoothed phase map



IPF-X map

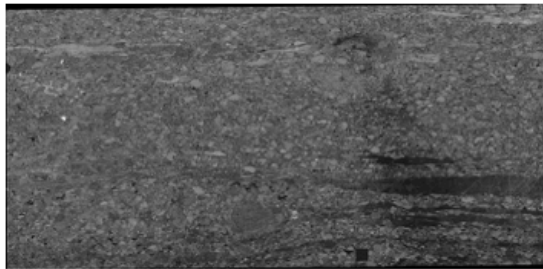


IPF-Y map

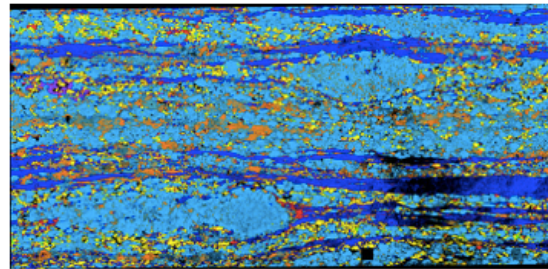


IPF-Z map

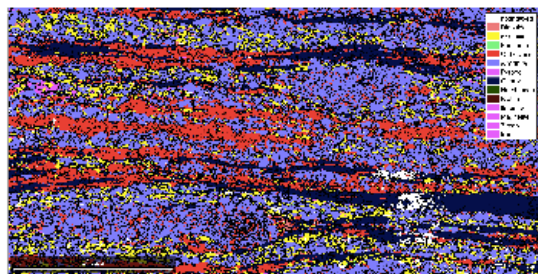
CH09-13ch-1



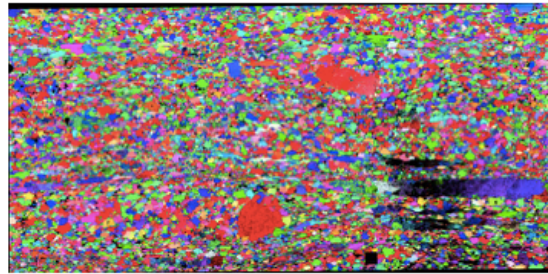
Band contrast



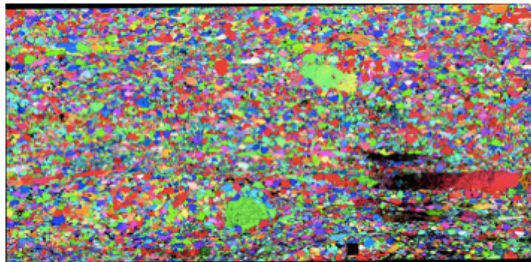
Phase map



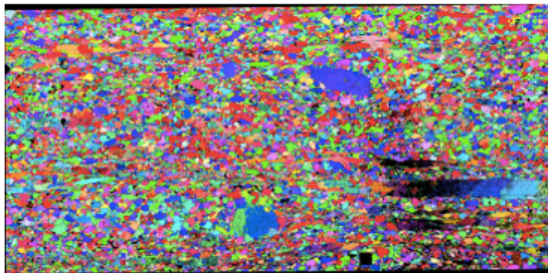
Matlab smoothed phase map



IPF-X map

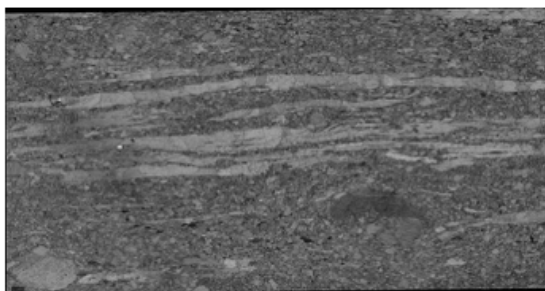


IPF-Y map

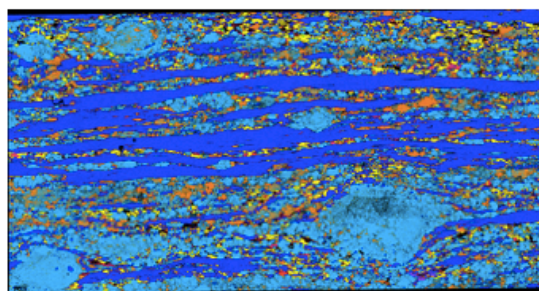


IPF-Z map

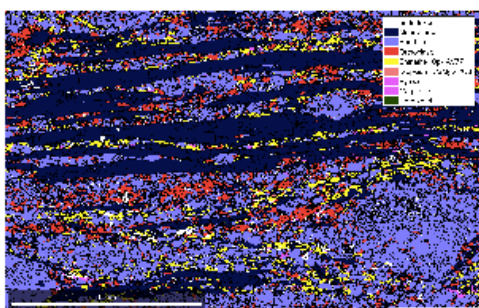
CH09-13ch-2



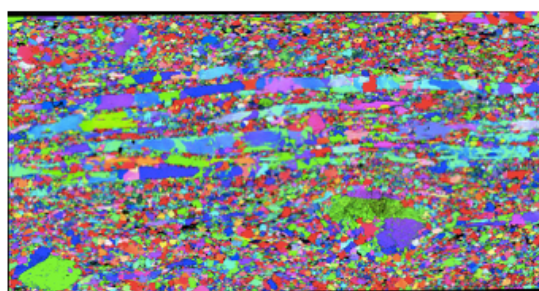
Band contrast



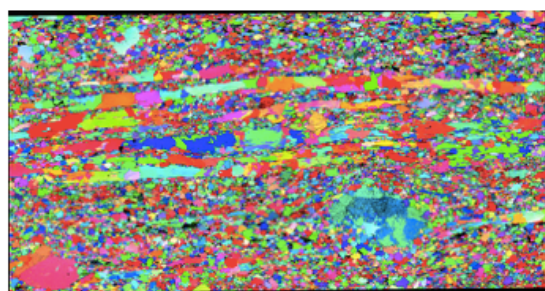
Phase map



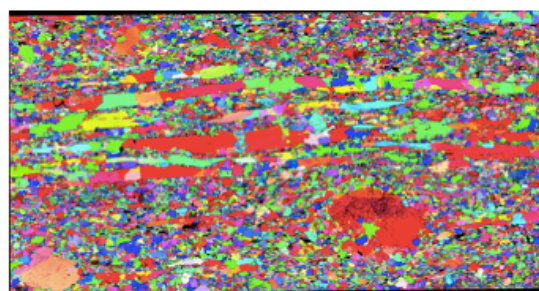
Matlab smoothed phase map



IPF-X map

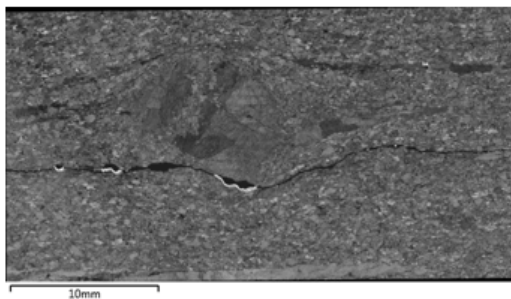


IPF-Y map

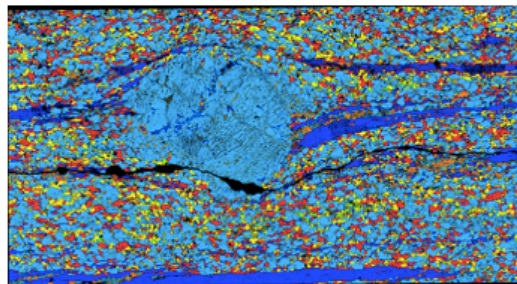


IPF-Z map

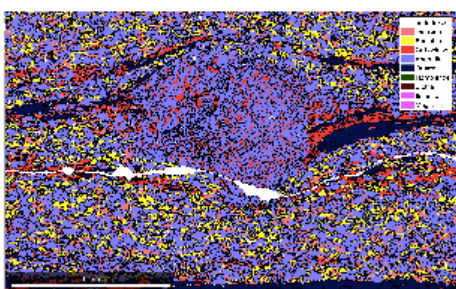
CH09-13fs



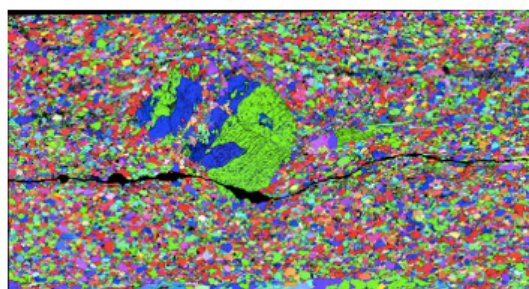
Band contrast



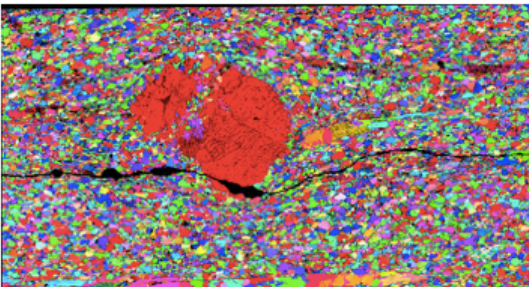
Phase map



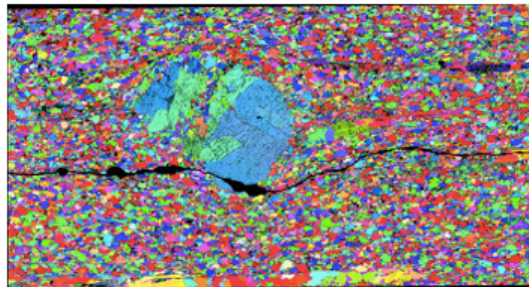
Matlab smoothed phase map



IPF-X map

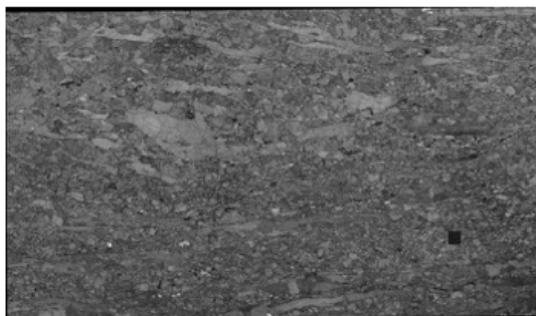


IPF-Y map

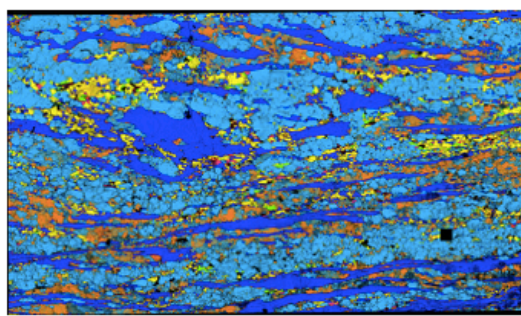


IPF-Z map

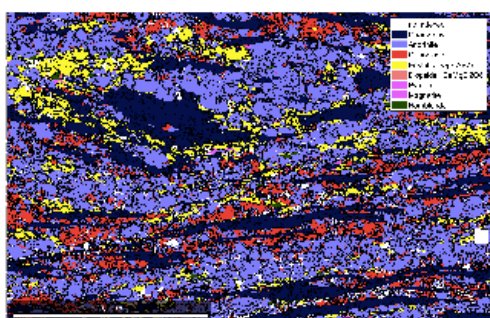
CH09-16ch



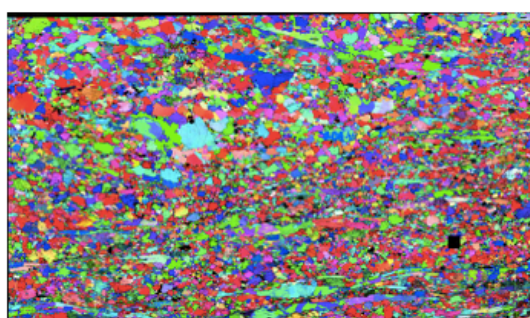
Band contrast



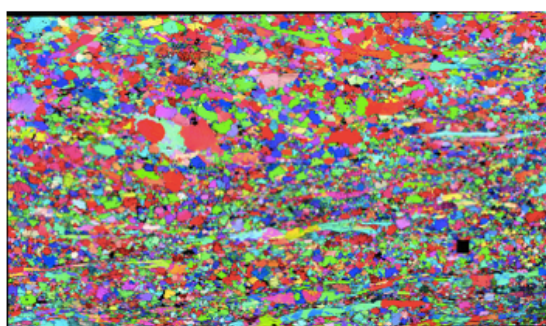
Phase map



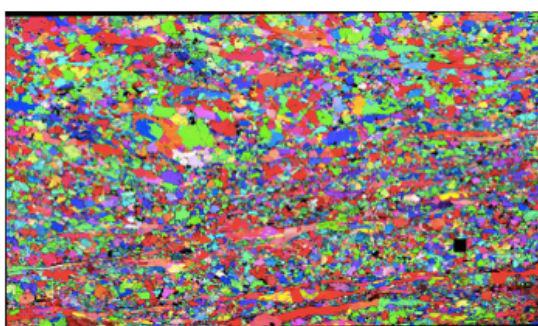
Matlab smoothed phase map



IPF-X map

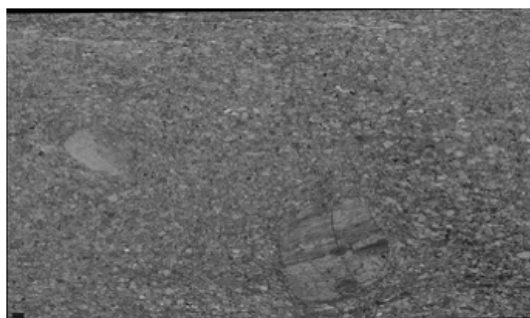


IPF-Y map

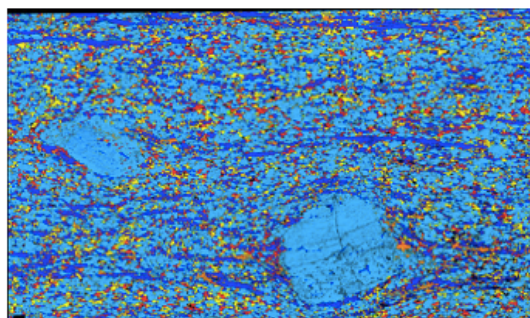


IPF-Z map

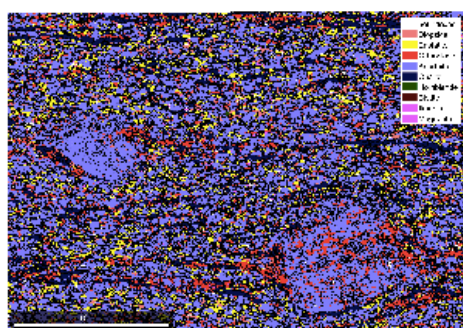
CH09-16fs



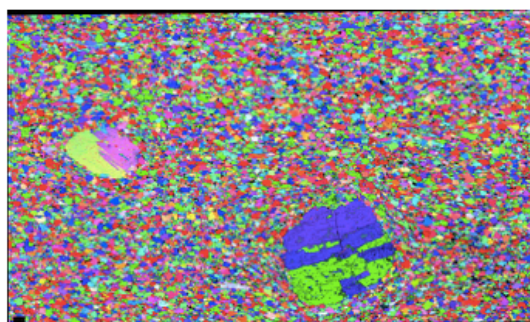
Band contrast



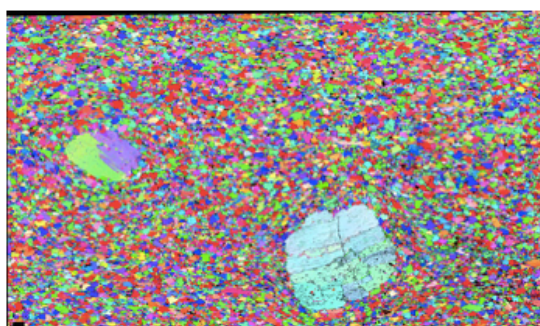
Phase map



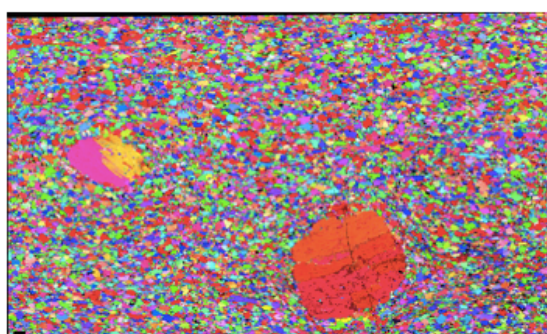
Matlab smoothed phase map



IPF-X map

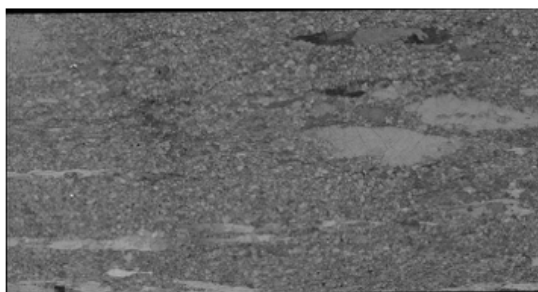


IPF-Y map

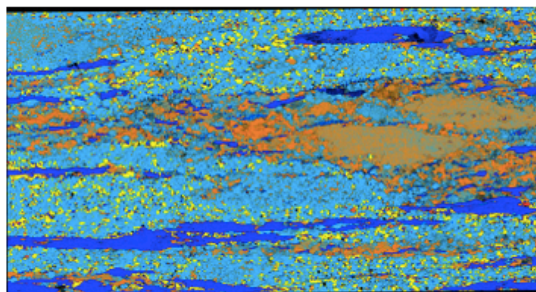


IPF-Z map

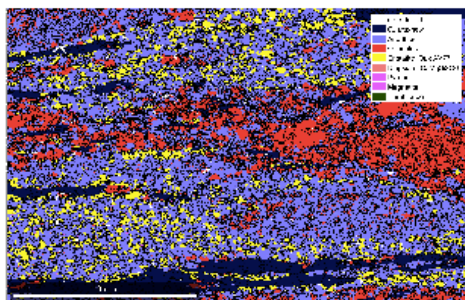
CH09-19ch-1



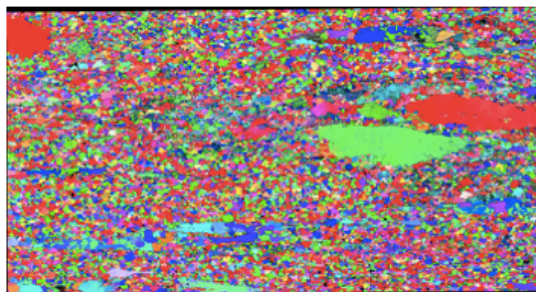
Band contrast



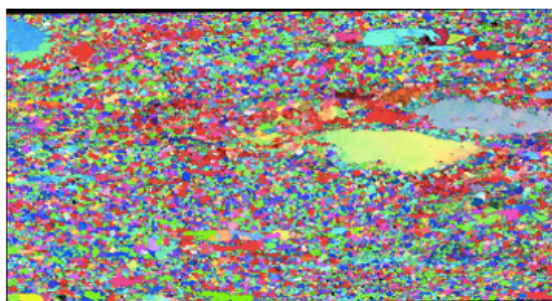
Phase map



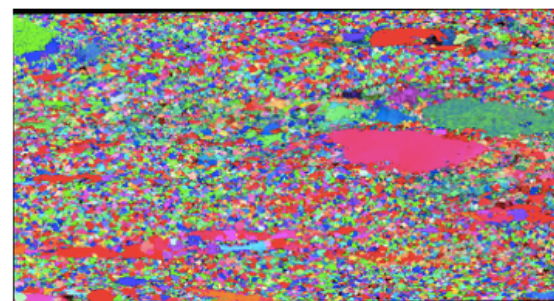
Matlab smoothed phase map



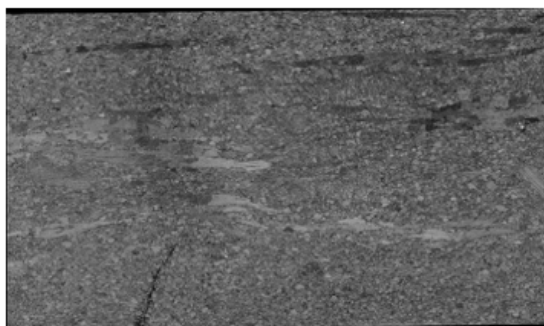
IPF-X map



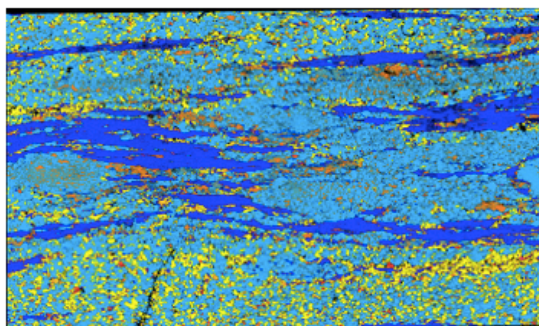
IPF-Y map



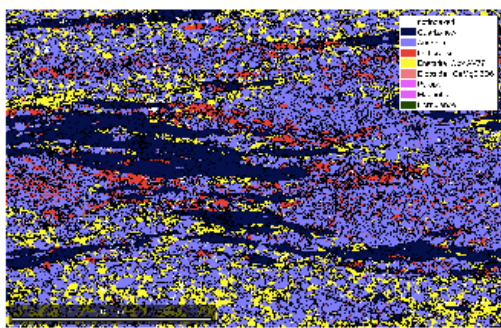
IPF-Z map



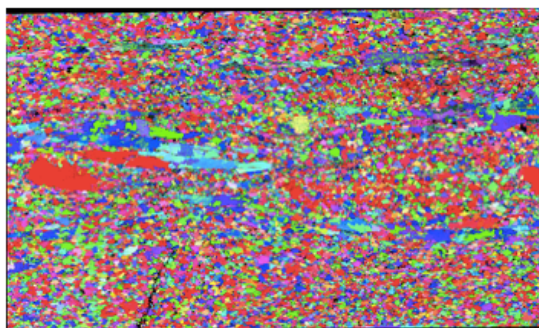
Band contrast



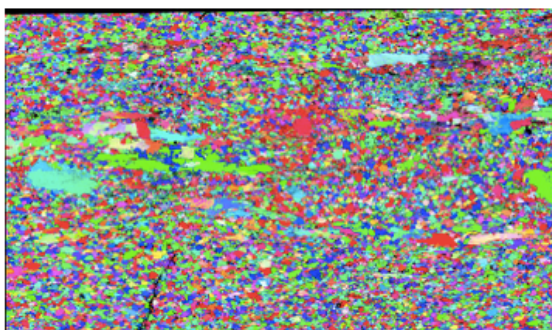
Phase map



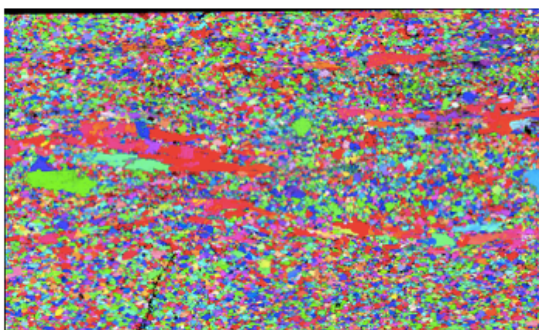
Matlab smoothed phase map



IPF-X map



IPF-Y map

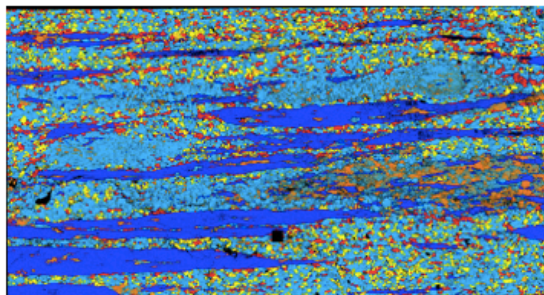


IPF-Z map

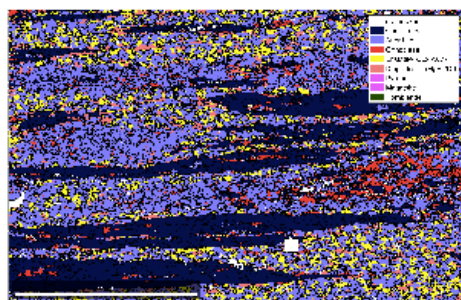
CH09-19fs



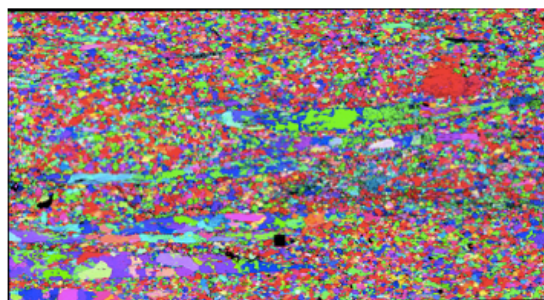
Band contrast



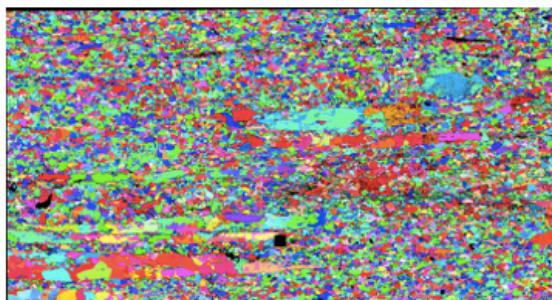
Phase map



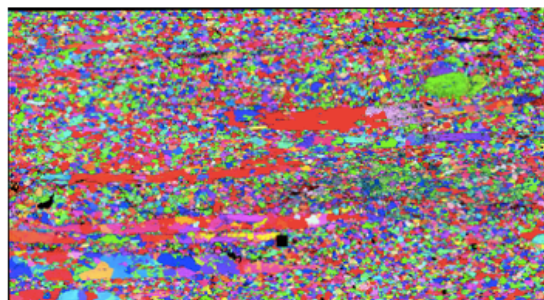
Matlab smoothed phase map



IPF-X map



IPF-Y map



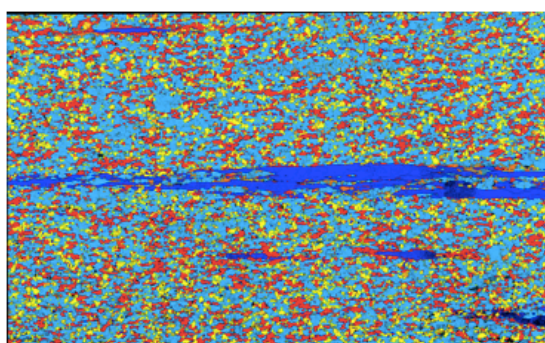
IPF-Z map

79

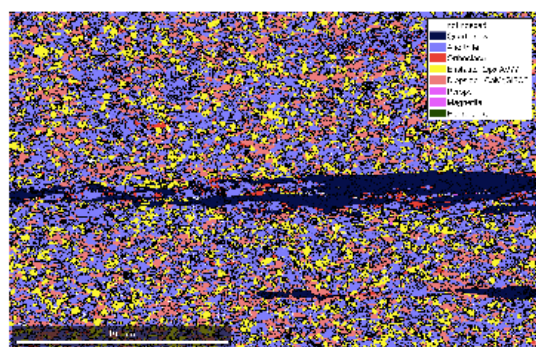
CH09-23fs



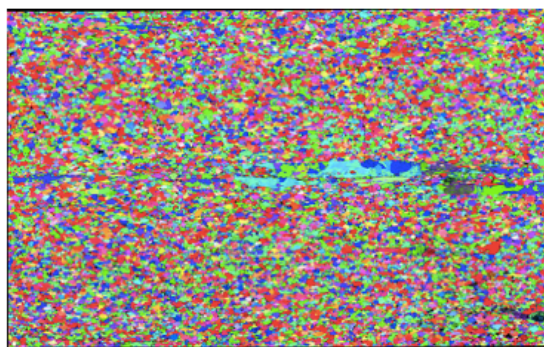
Band contrast



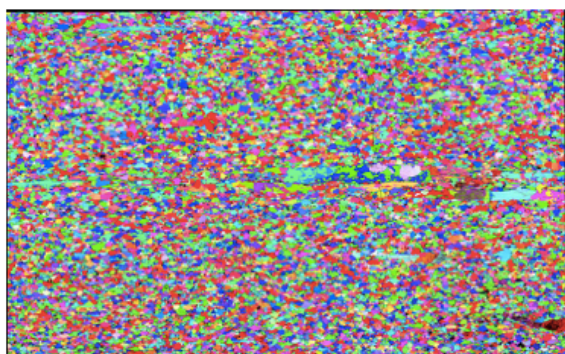
Phase map



Matlab smoothed phase map



IPF-X map

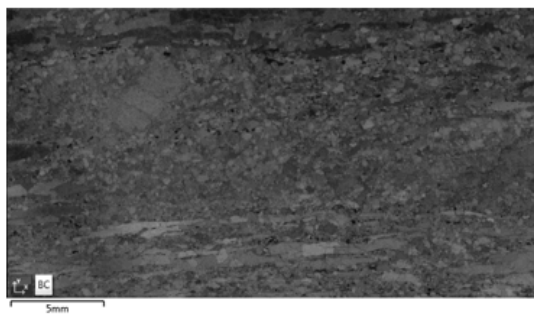


IPF-Y map

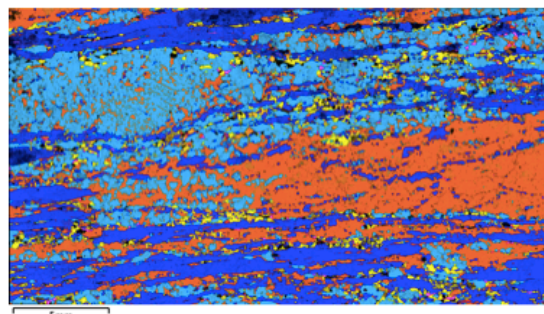


IPF-Z map

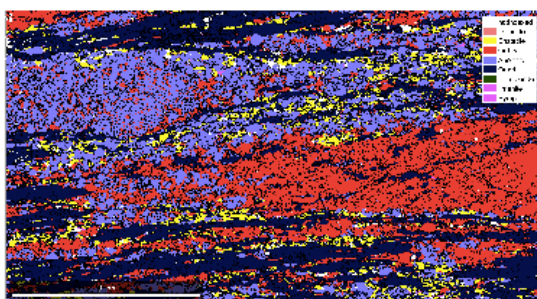
CH09-40ch



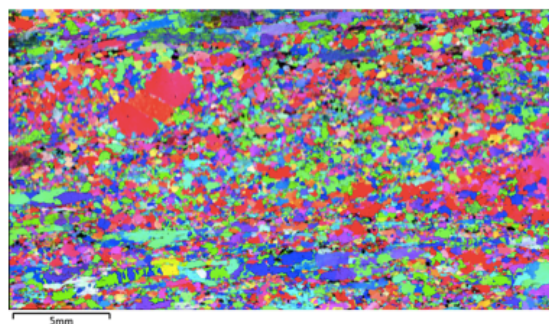
Band contrast



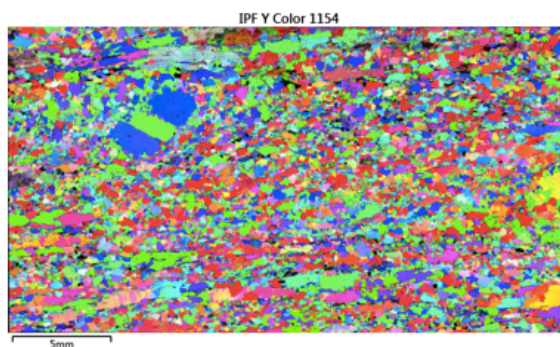
Phase map



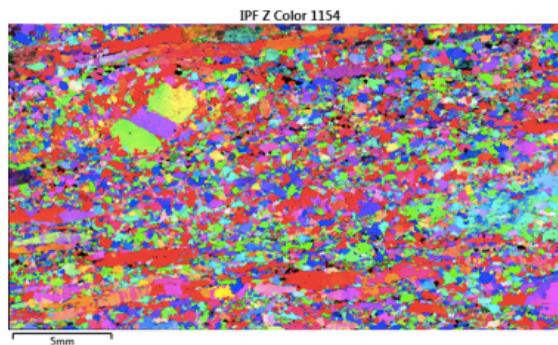
Matlab smoothed phase map



IPF-X map

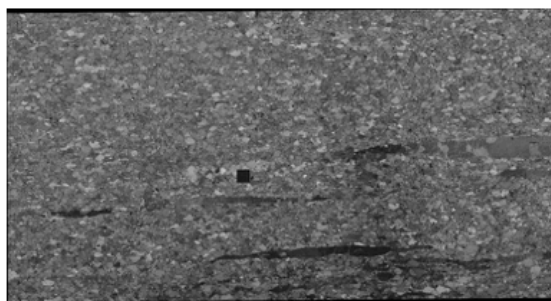


IPF-Y map

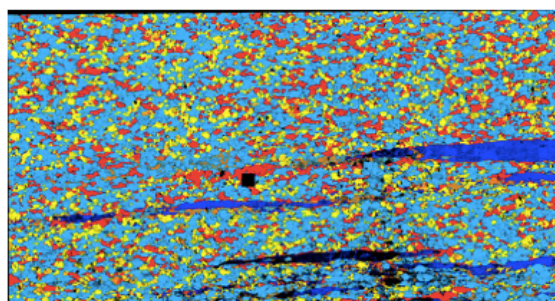


IPF-Z map

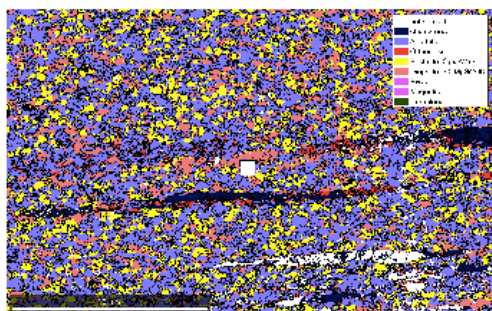
CH09-40fs



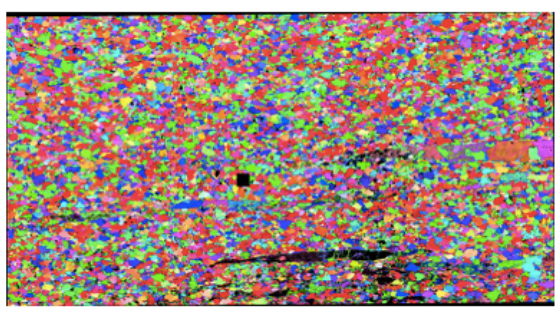
Band contrast



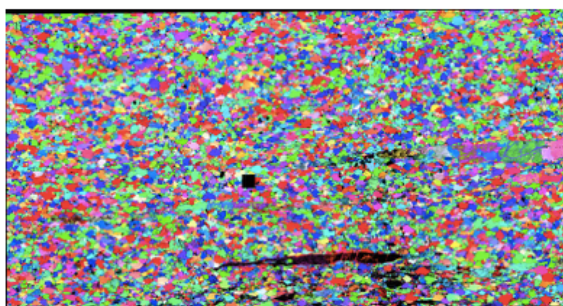
Phase map



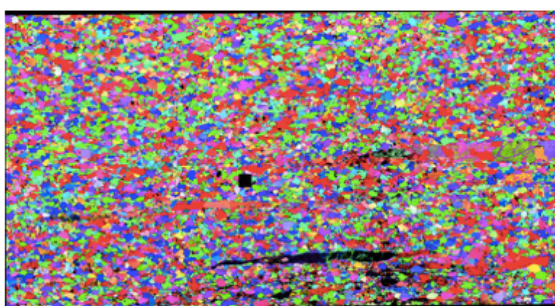
Matlab smoothed phase map



IPF-X map

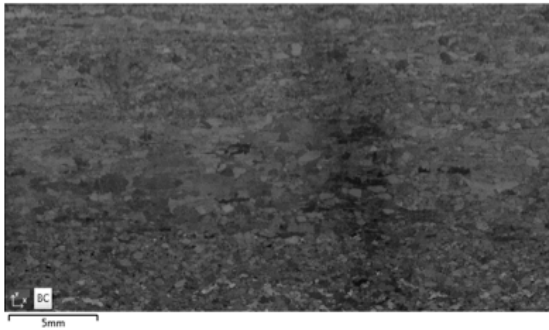


IPF-Y map

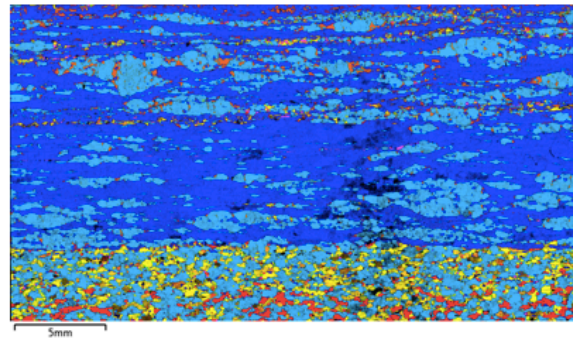


IPF-Z map

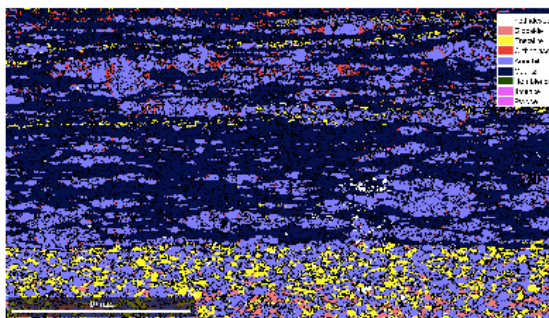
CH09-41ch



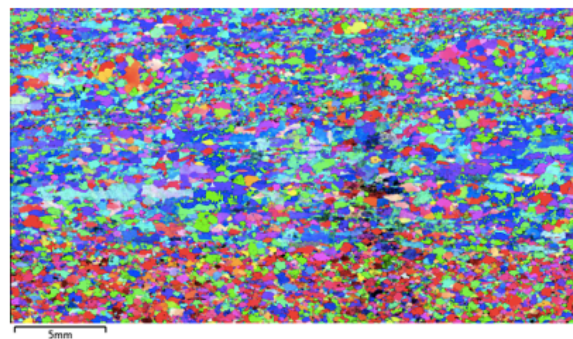
Band contrast



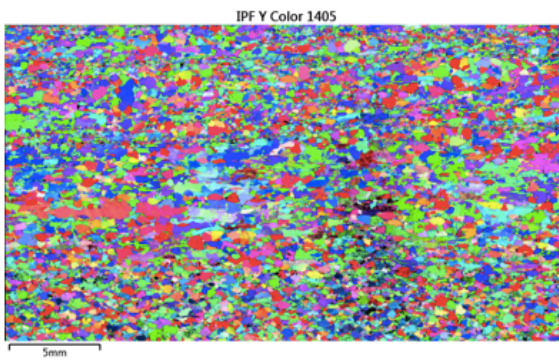
Phase map



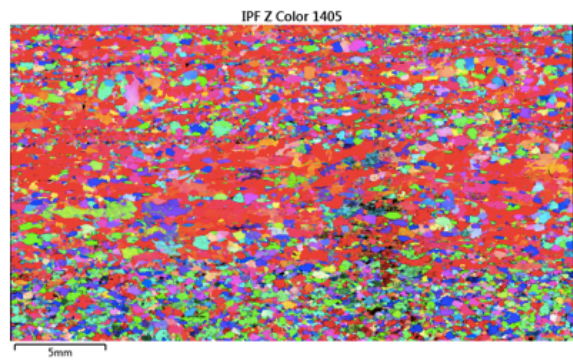
Matlab smoothed phase map



IPF-X map

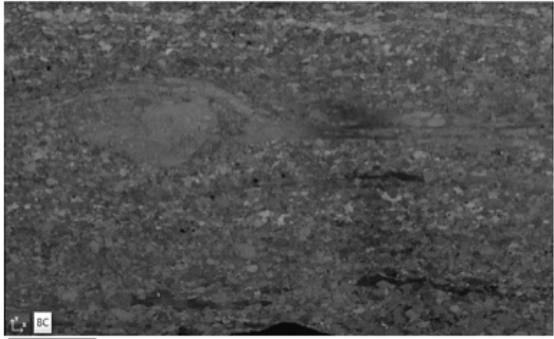


IPF-Y map

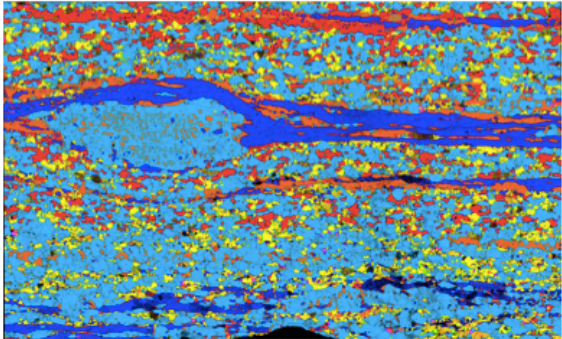


IPF-Z map

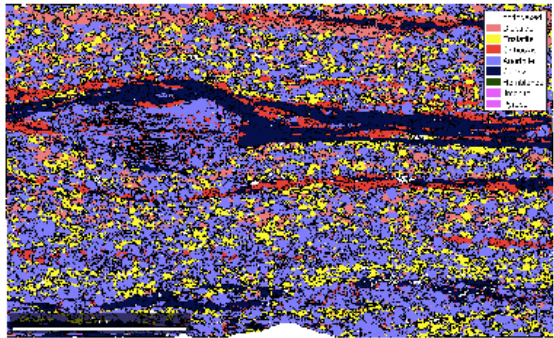
CH09-41fs



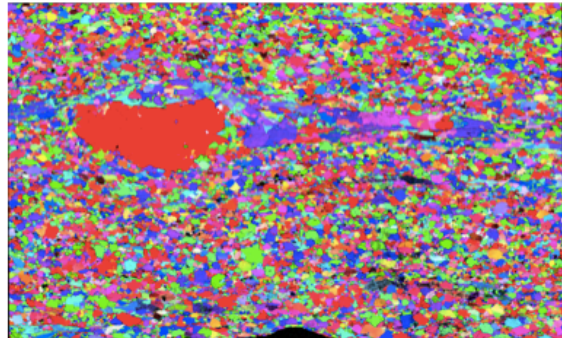
Band contrast



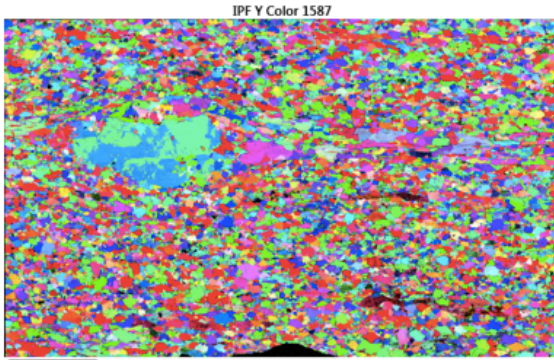
Phase map



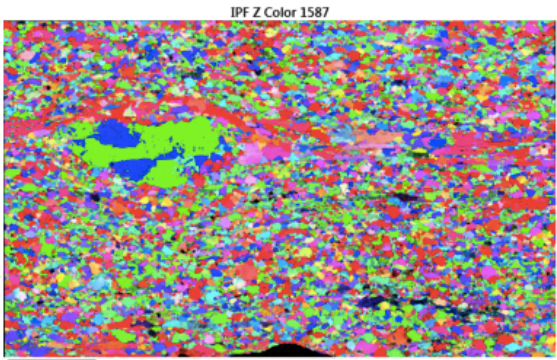
Matlab smoothed phase map



IPF-X map

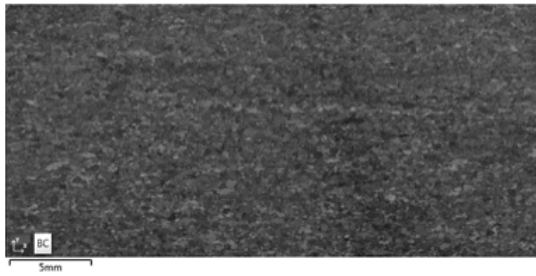


IPF-Y map

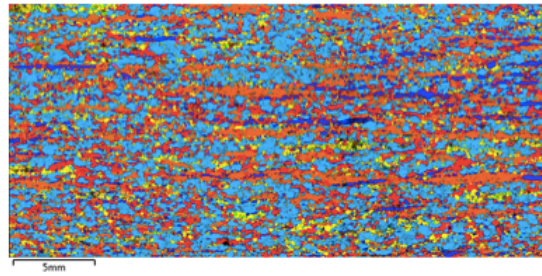


IPF-Z map

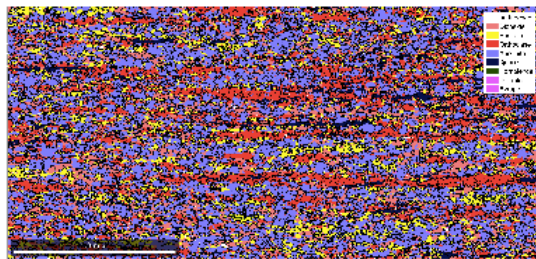
CH09-43fs



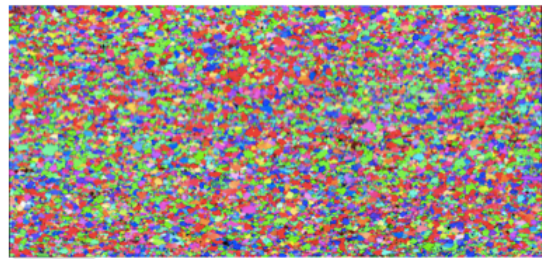
Band contrast



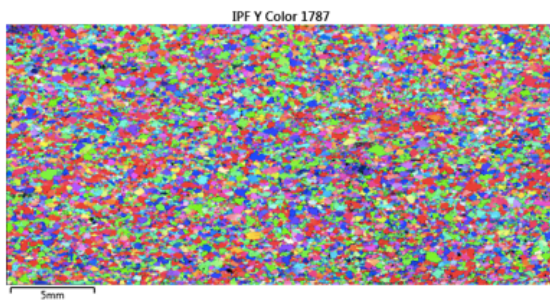
Phase map



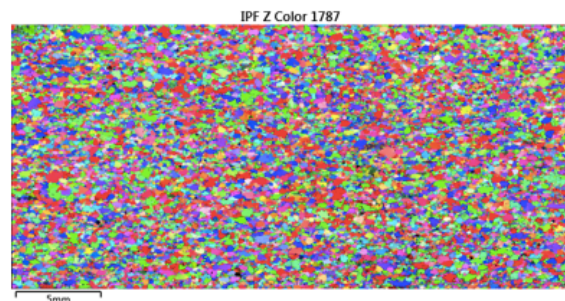
Matlab smoothed phase map



IPF-X map

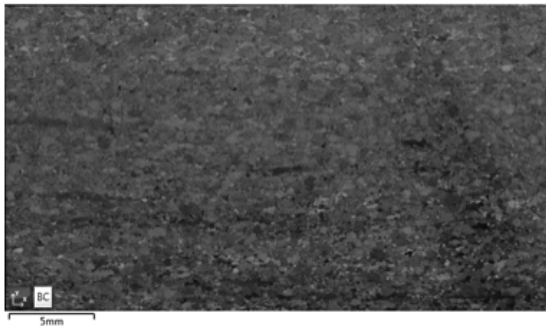


IPF-Y map

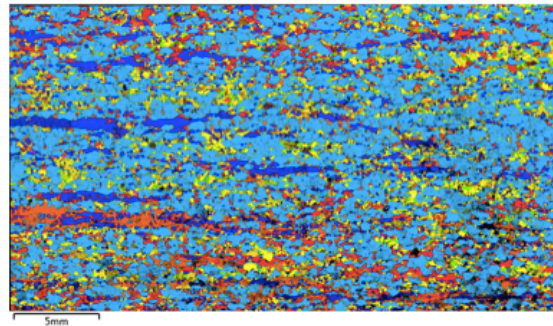


IPF-Z map

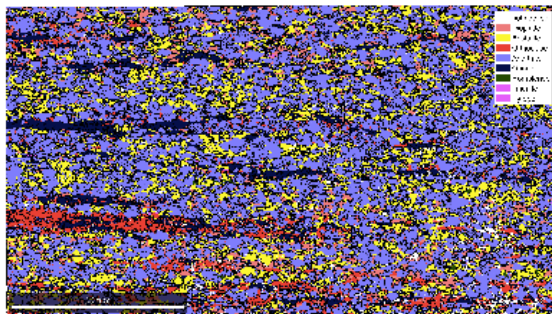
CH09-44ch



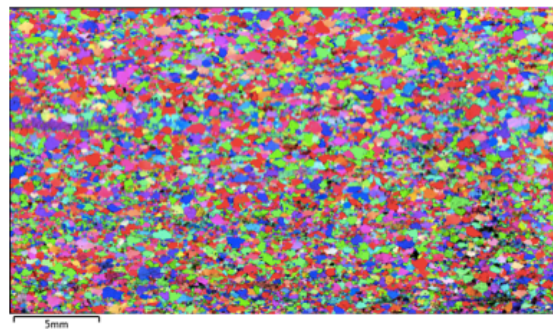
Band contrast



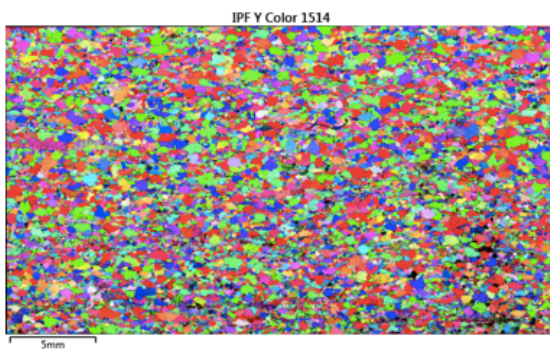
Phase map



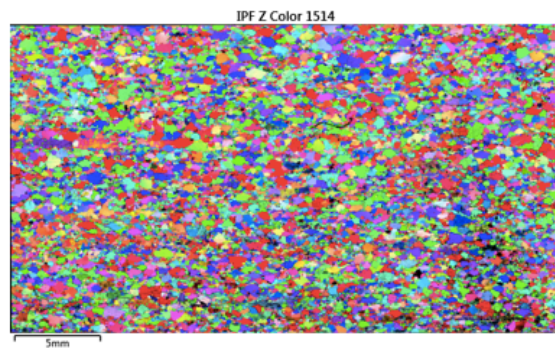
Matlab smoothed phase map



IPF-X map

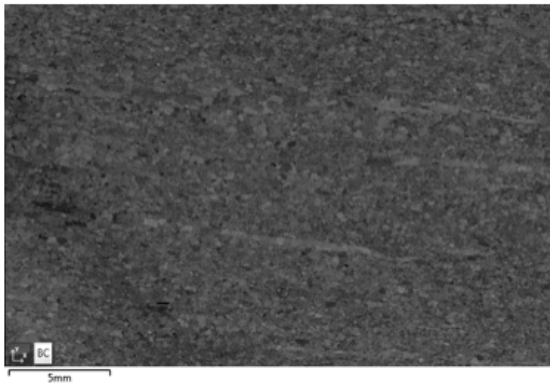


IPF-Y map

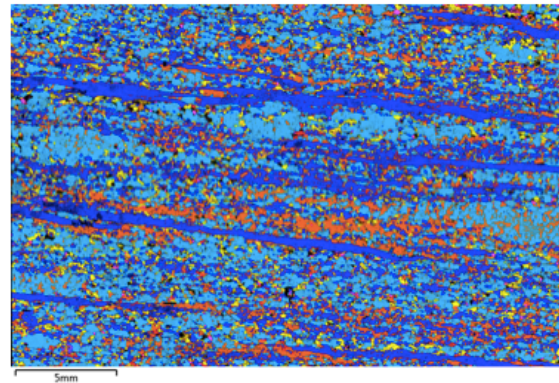


IPF-Z map

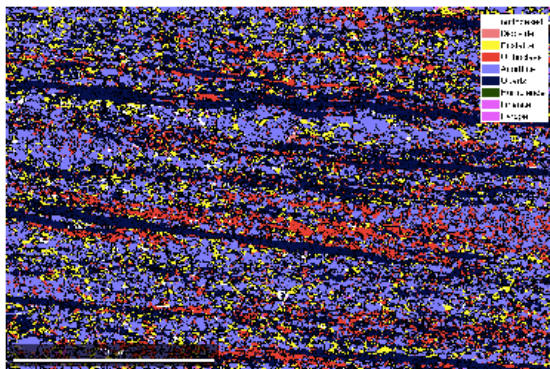
CH09-44fs



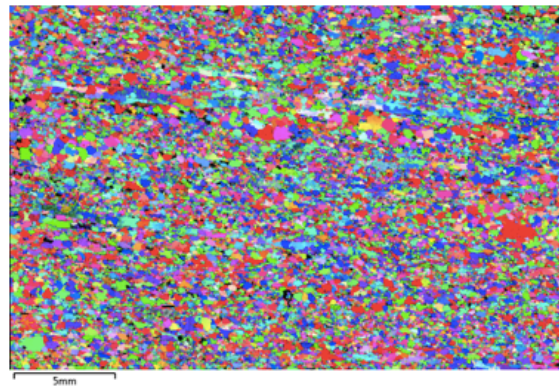
Band contrast



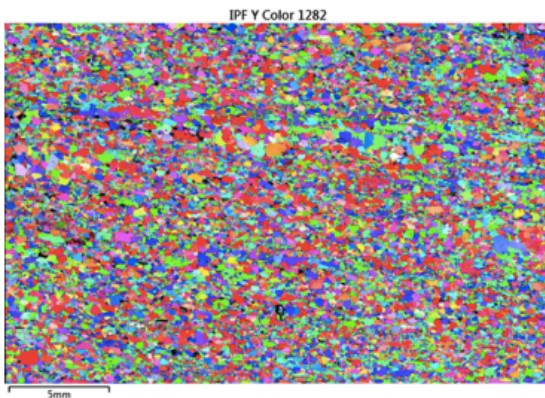
Phase map



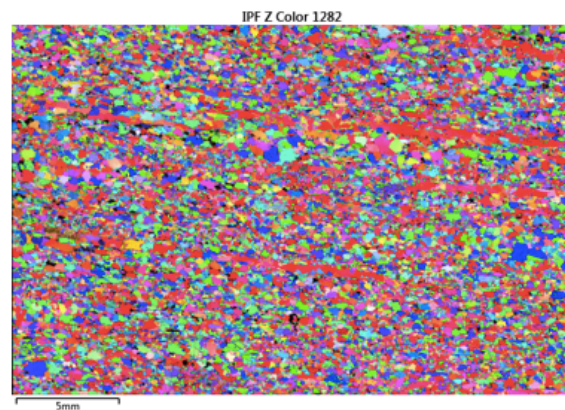
Matlab smoothed phase map





IPF-X map



IPF-Y map

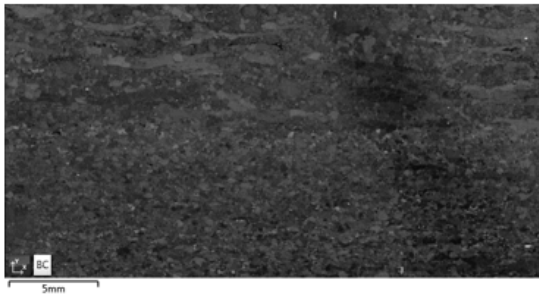


IPF-Z map

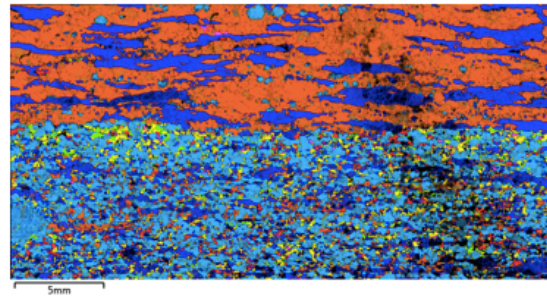


88

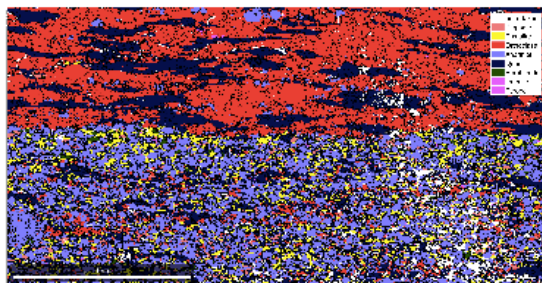
CH09-50ch



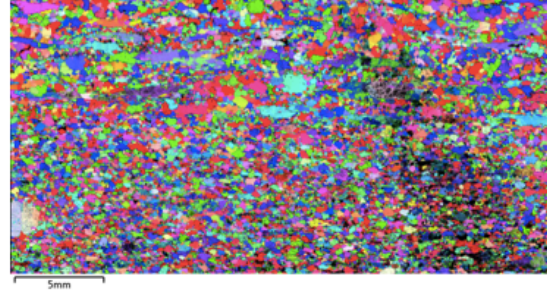
Band contrast



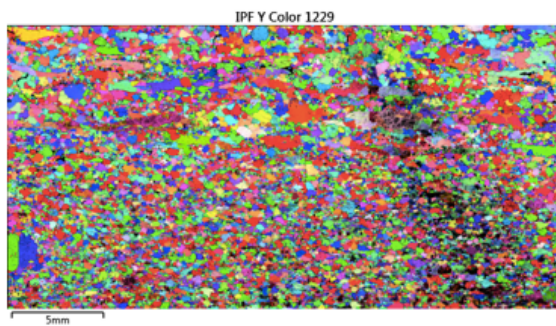
Phase map



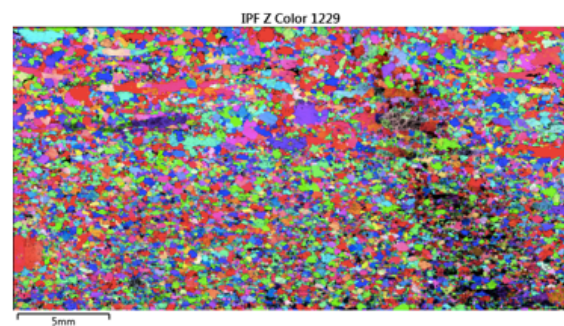
Matlab smoothed phase map



IPF-X map

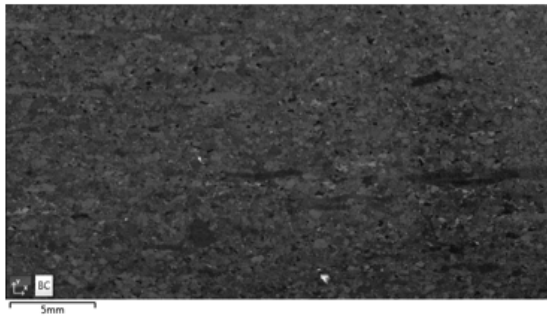


IPF-Y map

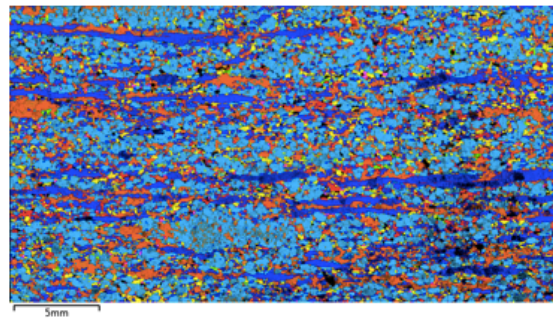


IPF-Z map

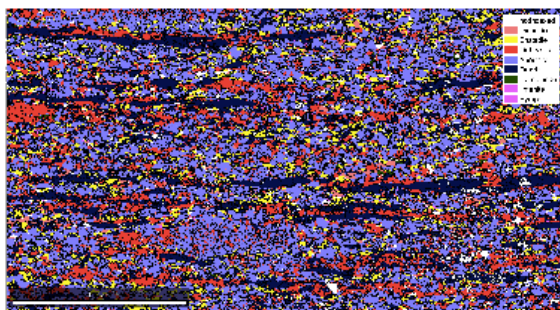
CH09-50fs



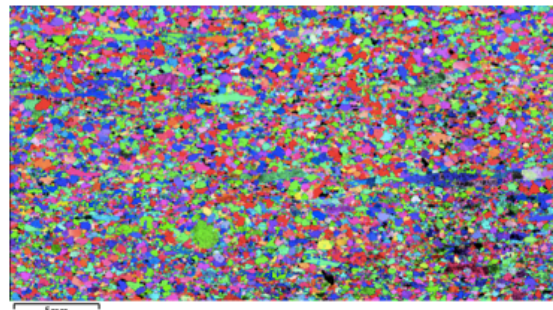
Band contrast



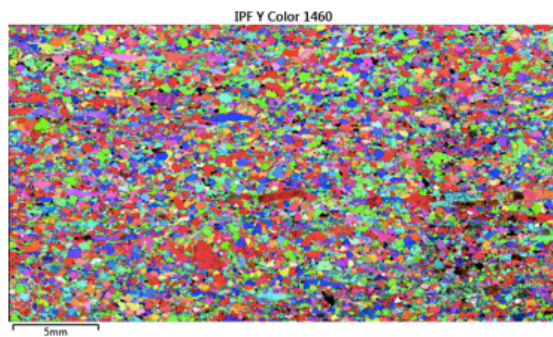
Phase map



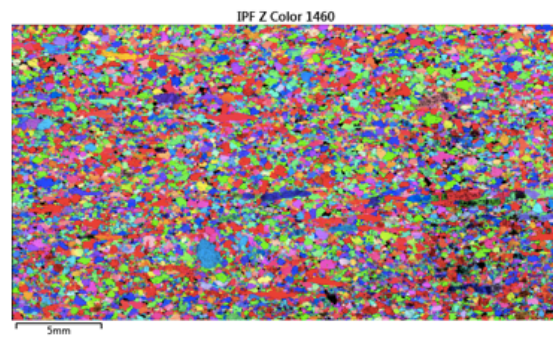
Matlab smoothed phase map



IPF-X map

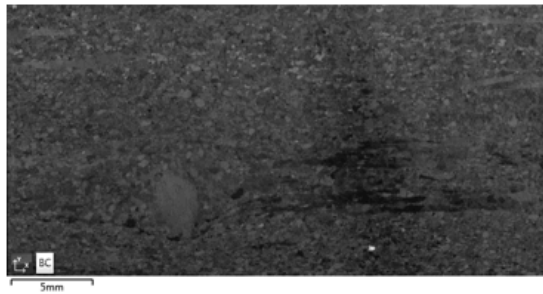


IPF-Y map

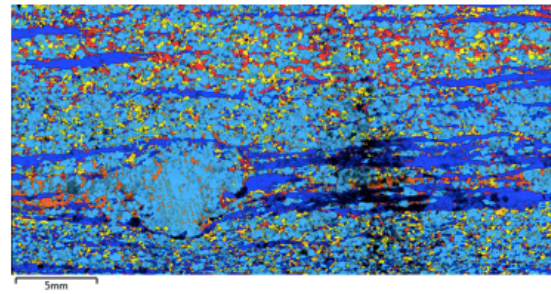


IPF-Z map

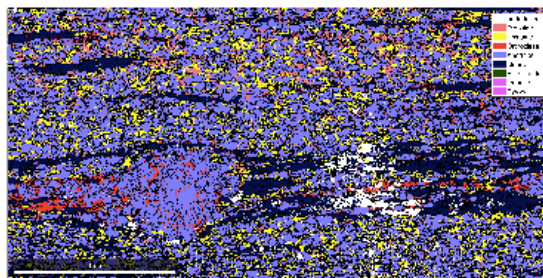
CH09-55fs



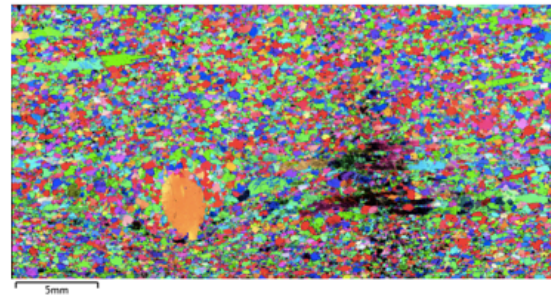
Band contrast



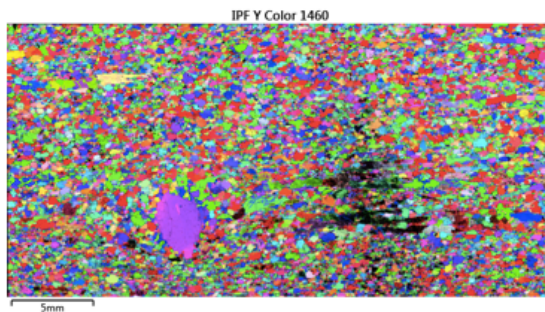
Phase map



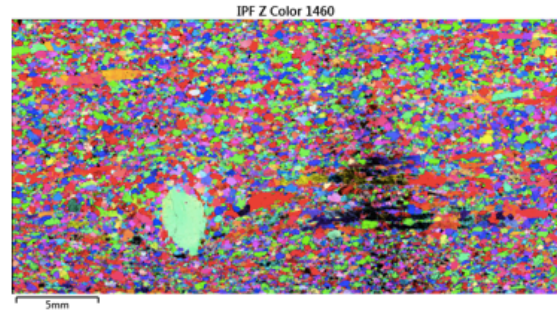
Matlab smoothed phase map



IPF-X map

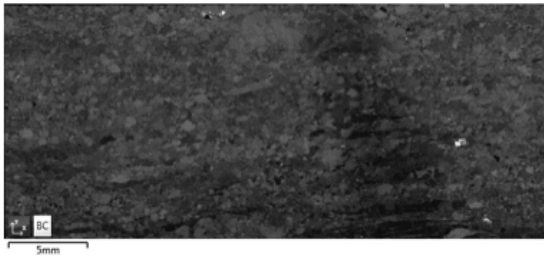


IPF-Y map

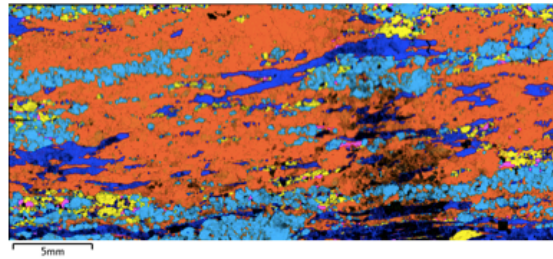


IPF-Z map

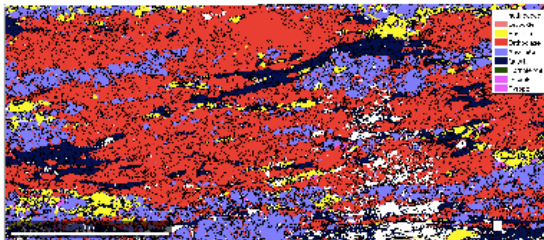
CH09-57ch



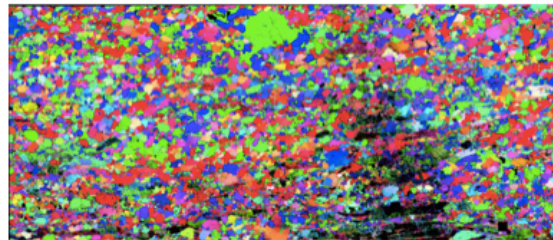
Band contrast



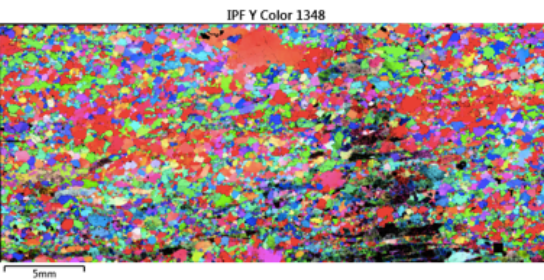
Phase map



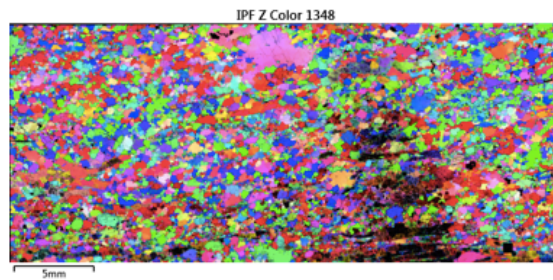
Matlab smoothed phase map



IPF-X map

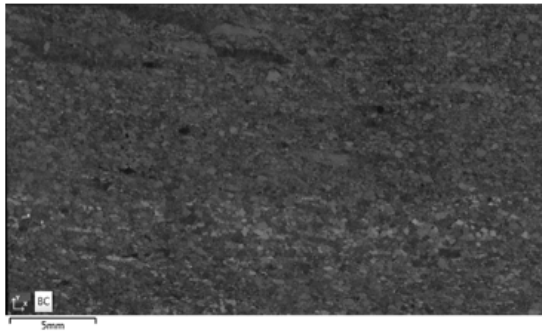


IPF-Y map

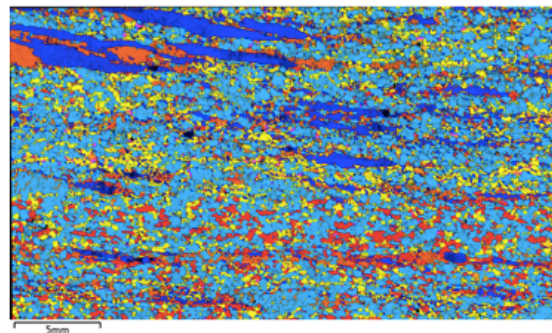


IPF-Z map

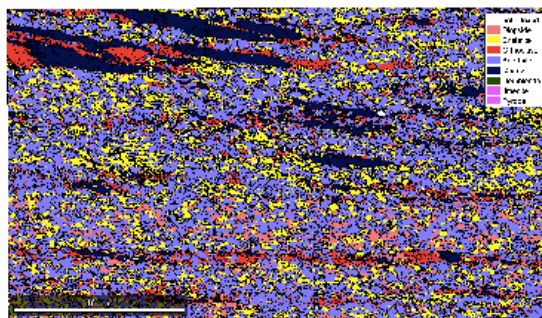
CH09-57fs



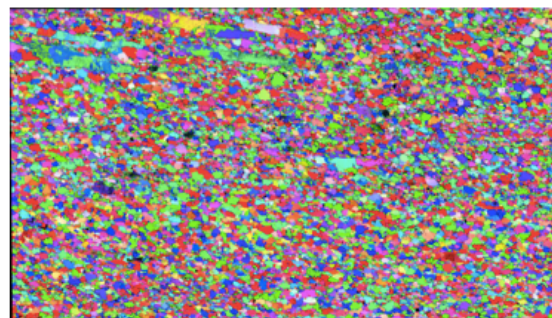
Band contrast



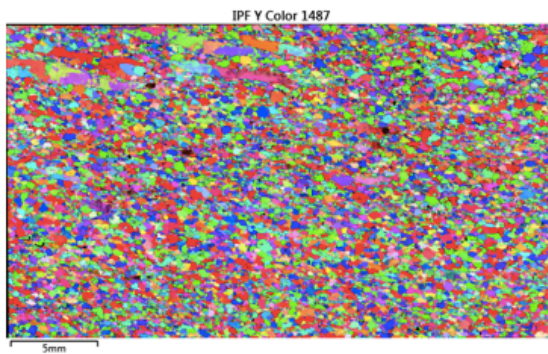
Phase map



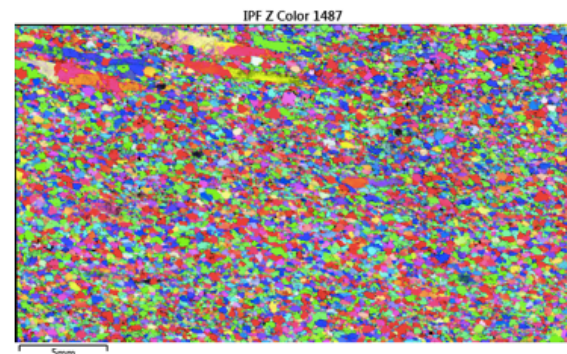
Matlab smoothed phase map



IPF-X map



IPF-Y map

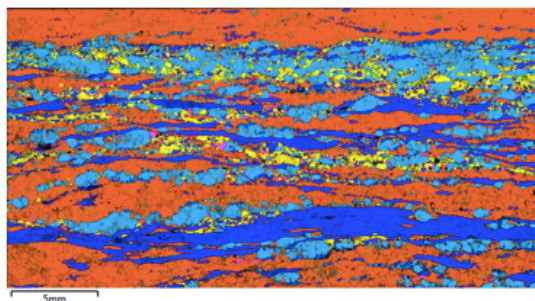


IPF-Z map

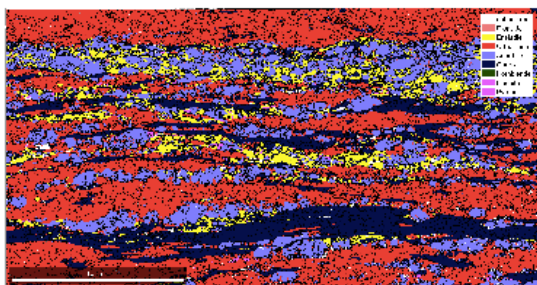
CH09-58ch



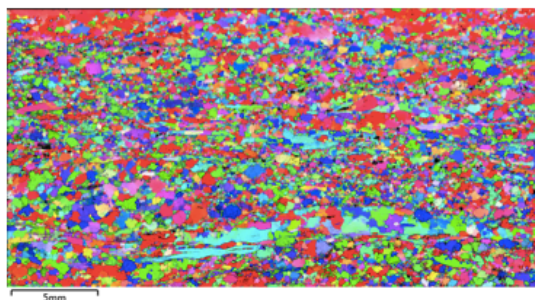
Band contrast



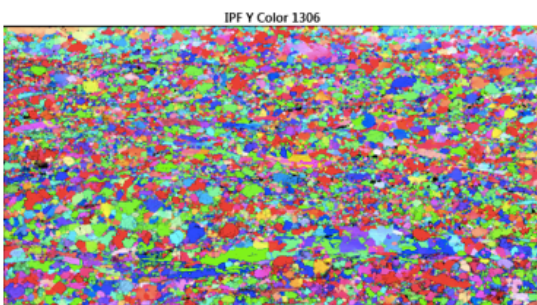
Phase map



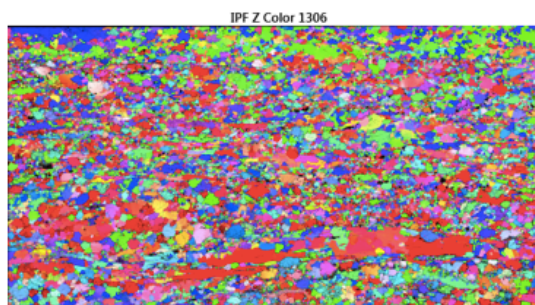
Matlab smoothed phase map



IPF-X map

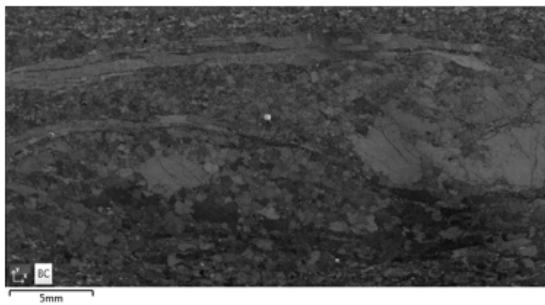


IPF-Y map

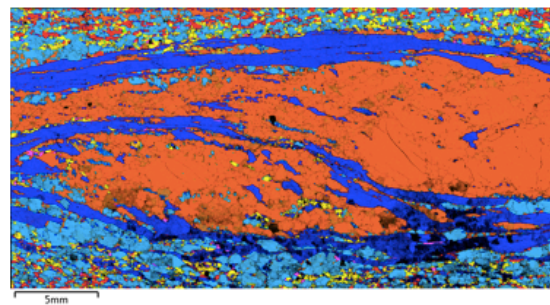


IPF-Z map

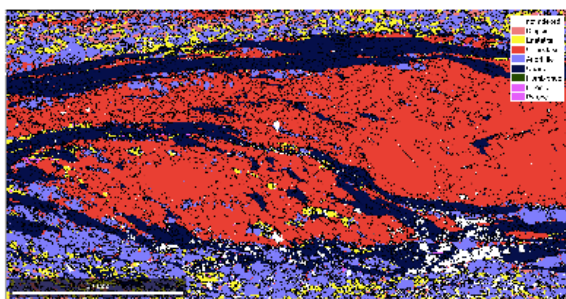
CH09-58fs



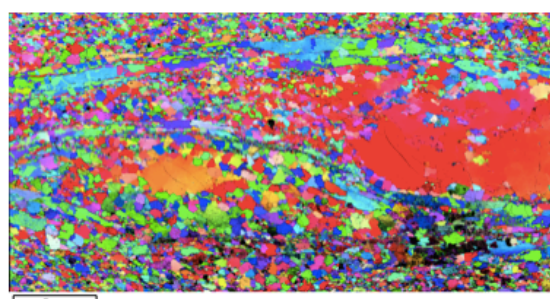
Band contrast



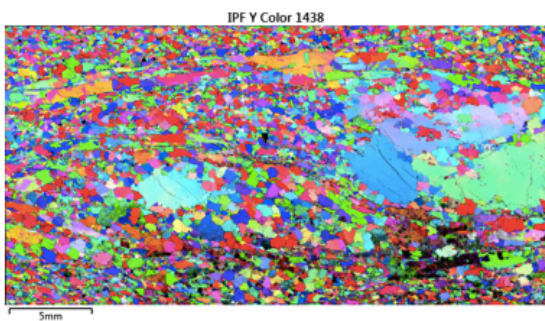
Phase map



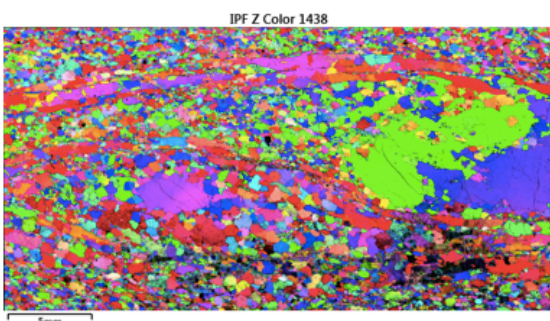
Matlab smoothed phase map



IPF-X map

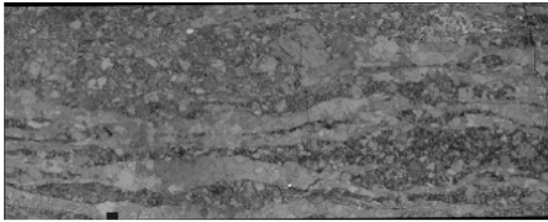


IPF-Y map

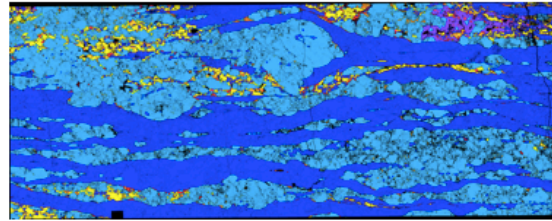


IPF-Z map

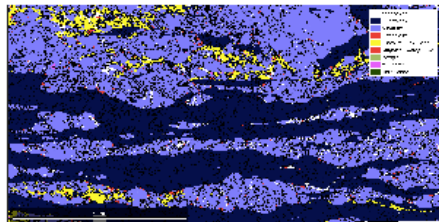
CH09-68ch



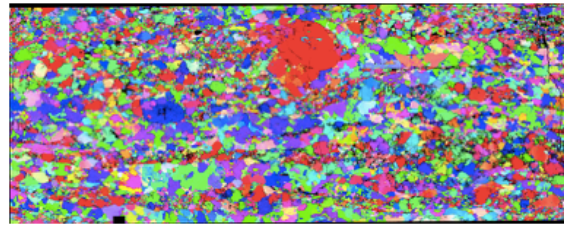
Band contrast



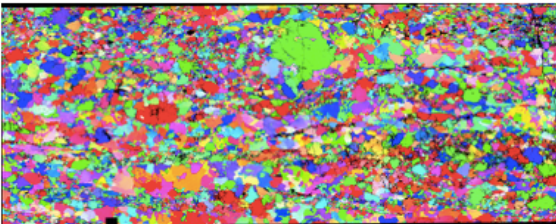
Phase map



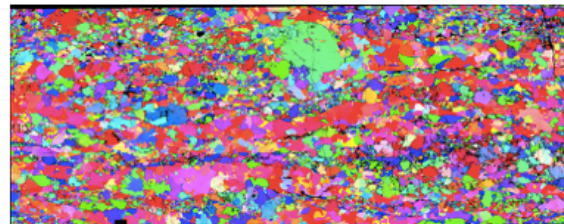
Matlab smoothed phase map



IPF-X map

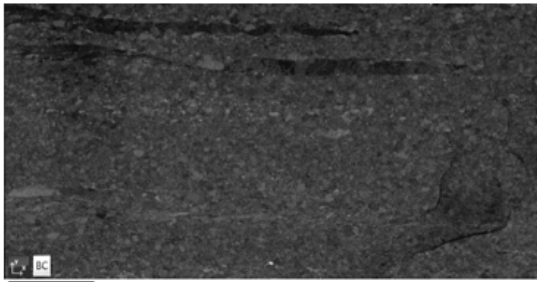


IPF-Y map

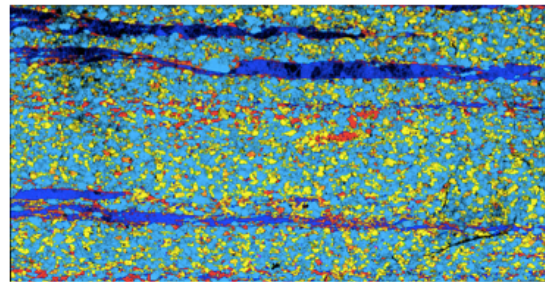


IPF-Z map

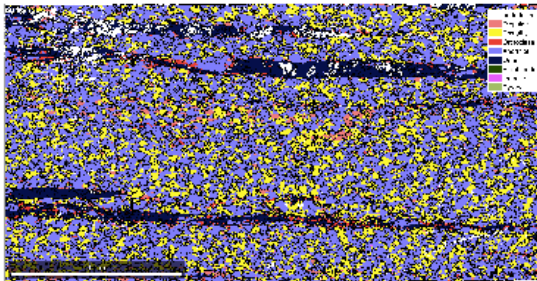
CH09-68fs



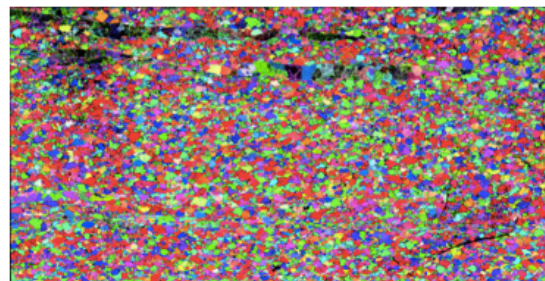
Band contrast



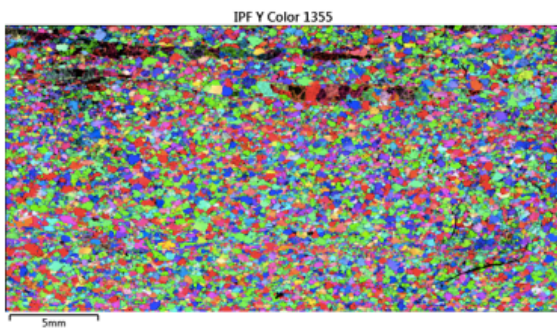
Phase map



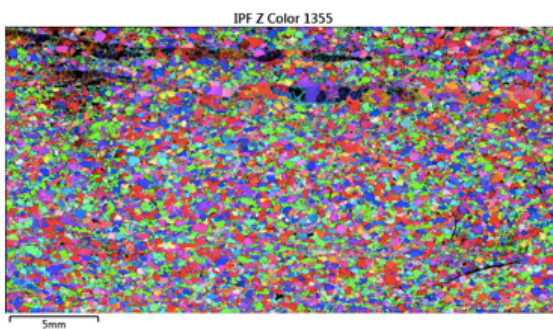
Matlab smoothed phase map



IPF-X map

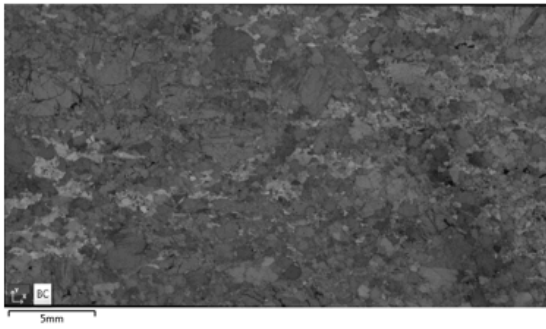


IPF-Y map

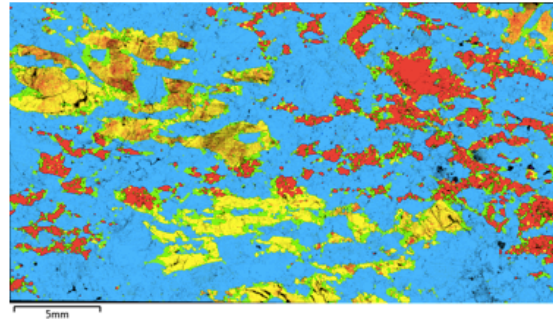


IPF-Z map

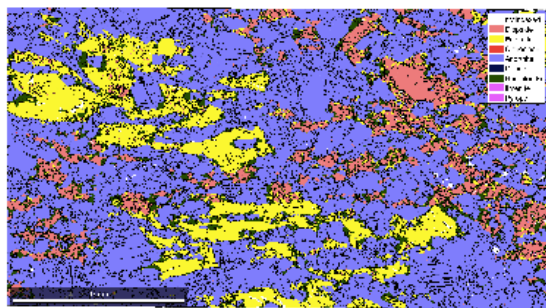
HD09-11b



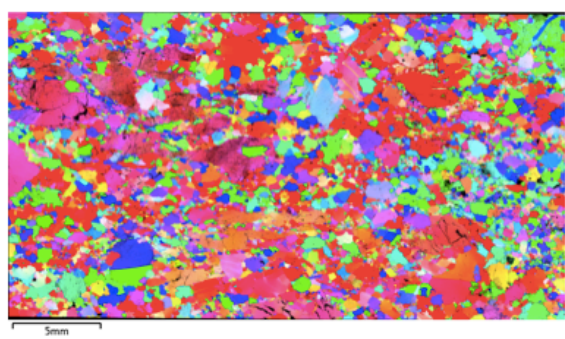
Band contrast



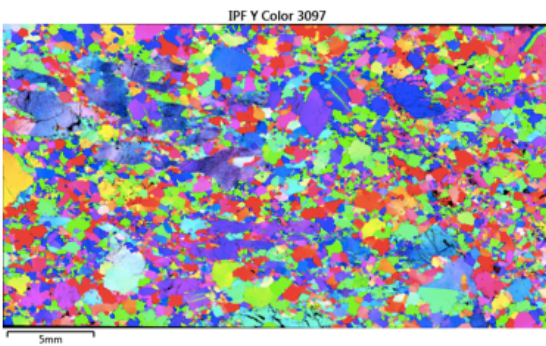
Phase map



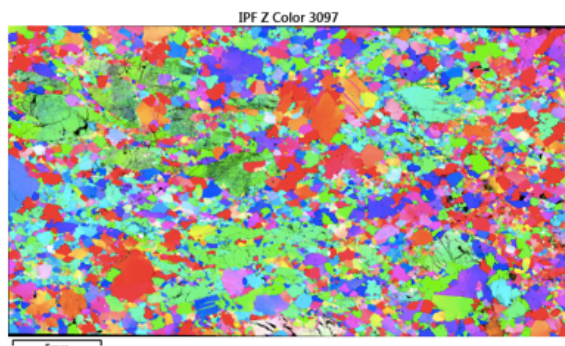
Matlab smoothed phase map



IPF-X map

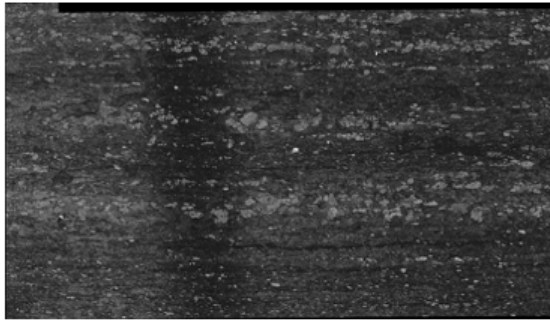


IPF-Y map

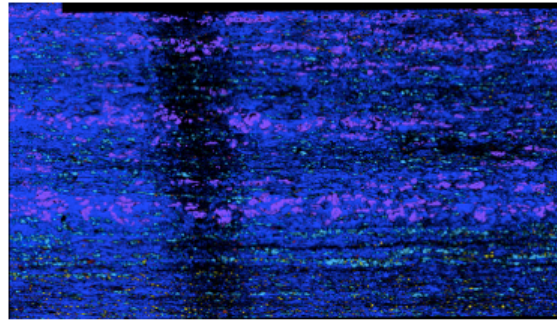


IPF-Z map

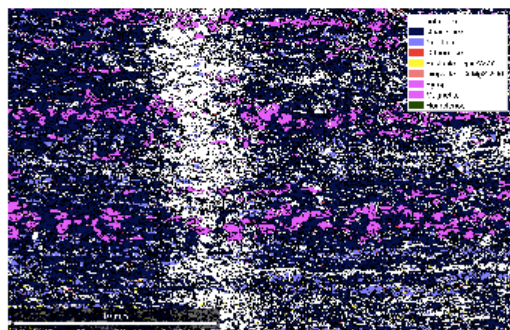
HD09-27



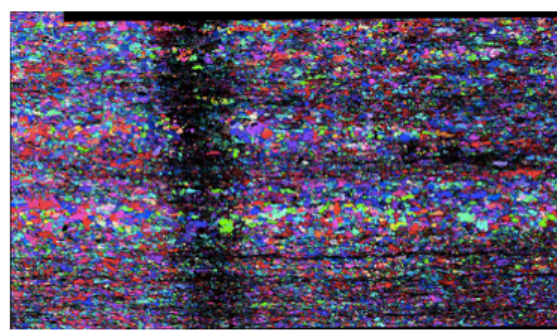
Band contrast



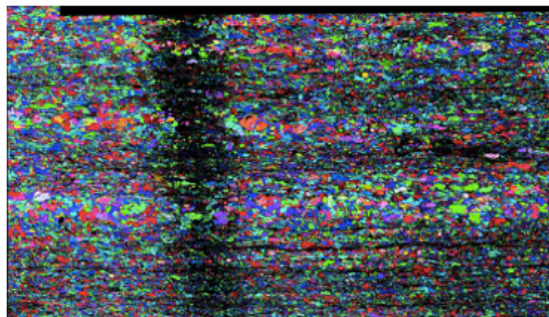
Phase map



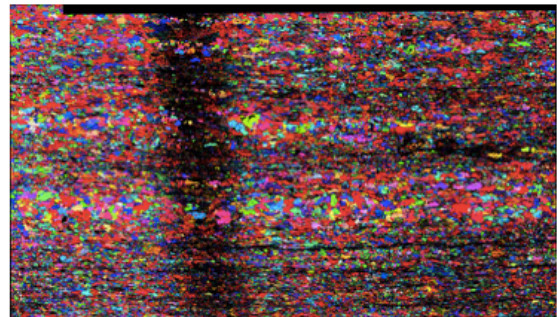
Matlab smoothed phase map



IPF-X map



IPF-Y map

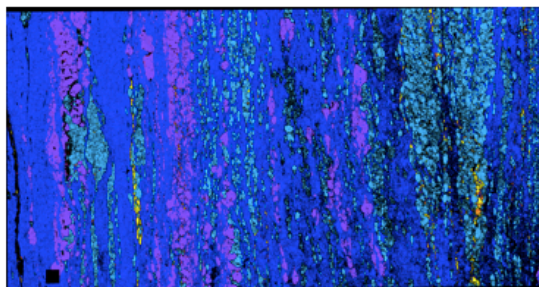


IPF-Z map

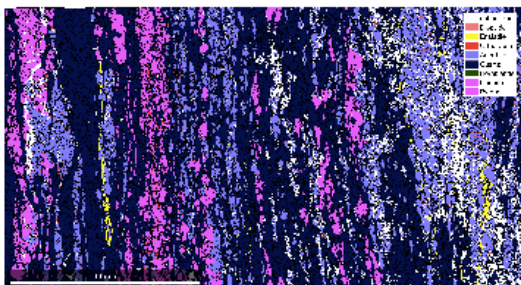
HD09-28



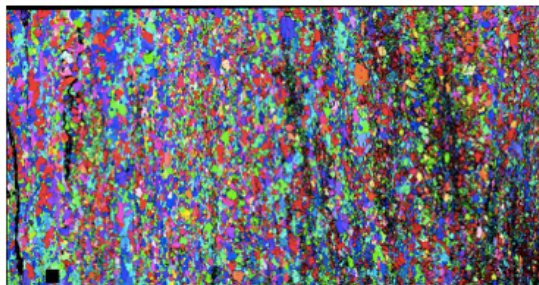
Band contrast



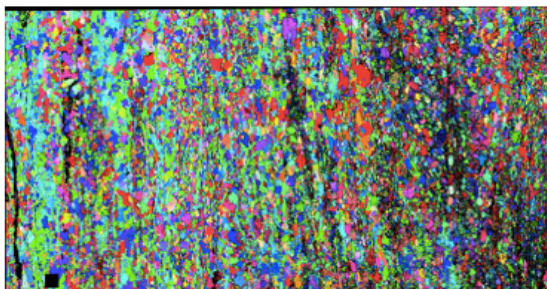
Phase map



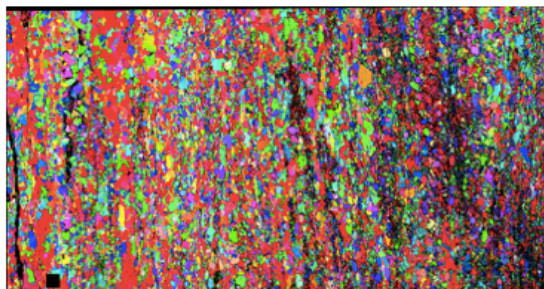
Matlab smoothed phase map



IPF-X map

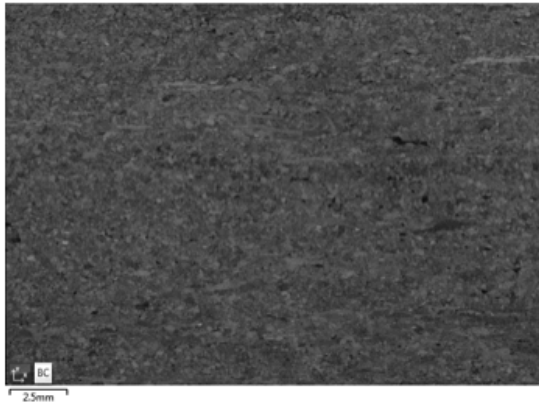


IPF-Y map

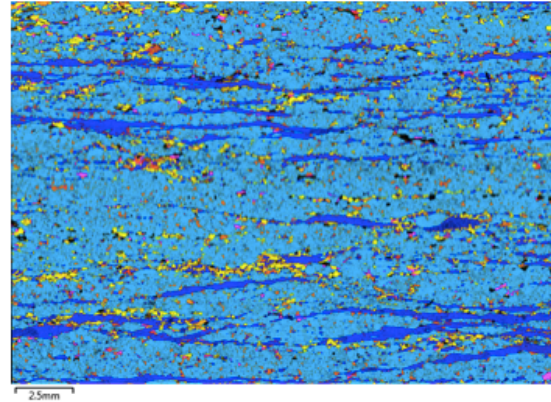


IPF-Z map

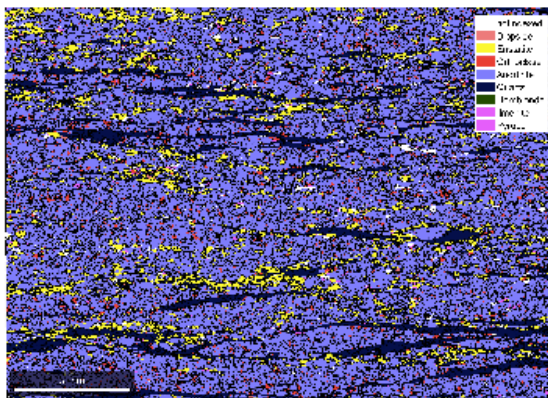
HD09-29



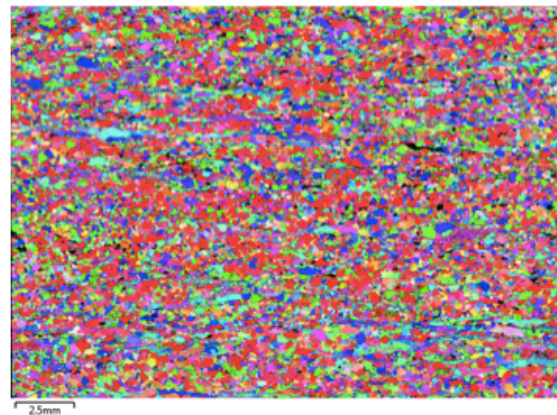
Band contrast



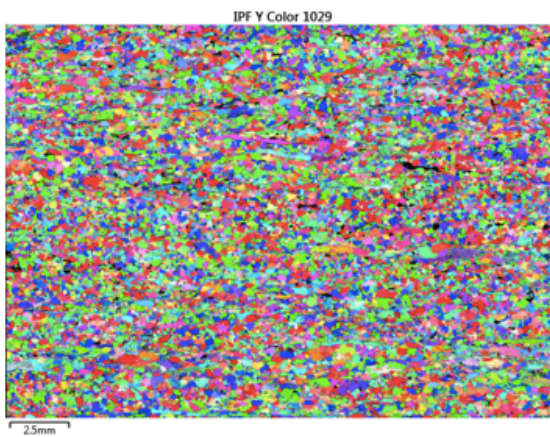
Phase map



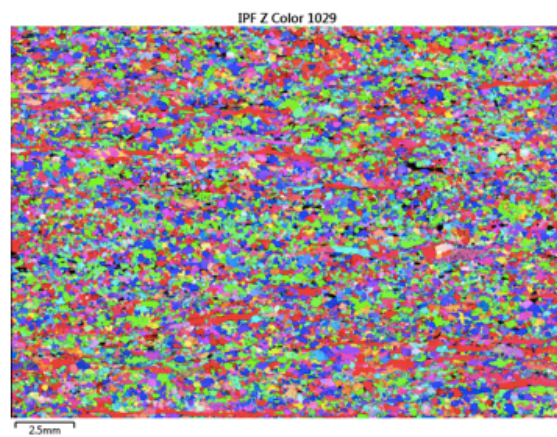
Matlab smoothed phase map



IPF-X map



IPF-Y map



IPF-Z map

Appendix D.

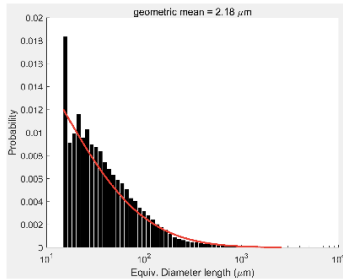
Average Grain Size Histograms

Equivalent Diameter Distribution Plots and Resultant Geometric Means for Quartz, Plagioclase, Enstatite, and Diopside, using a 3-pixel cut-off

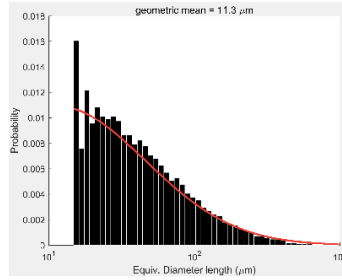
Note: the red curve for each graph shows the Gaussian distribution of the grains and the geometric mean listed on each graph is that based on the Gaussian distribution. Some graphs do not illustrate a Gaussian distribution and so the predicted geometric mean based on this is inaccurate. The geometric means used for the actual differential stress calculations were determined by using the MTEX function `geomean(2*(equivalentRadius('phase')))`, where 'phase' was quartz, plagioclase, enstatite, and diopside. The equivalent diameters were calculated using a correction factor of 1.2 and the grains on the edges of the thin sections that were incomplete were excluded.

Quartz

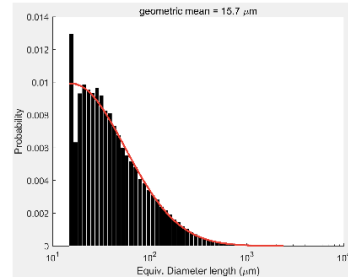
AF09-3A:



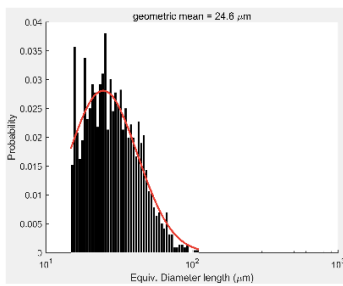
AF09-12:



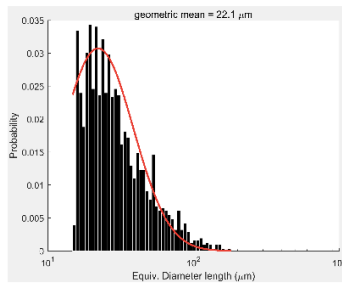
AF09-15:



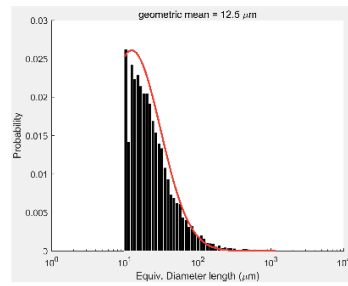
AF09-19:



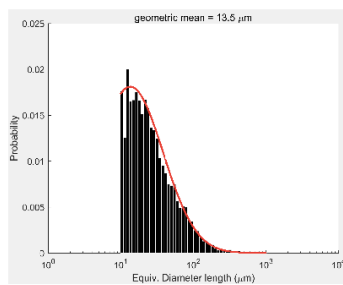
CH09-08A:



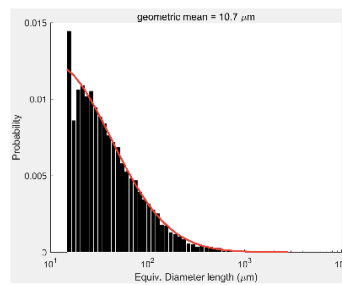
CH09-08B:



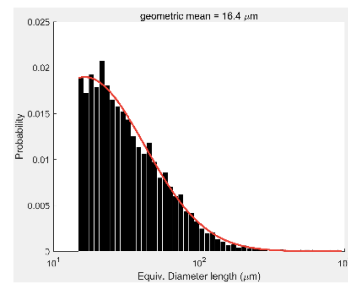
CH09-08C:



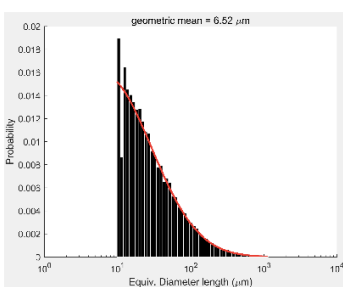
CH09-09A:



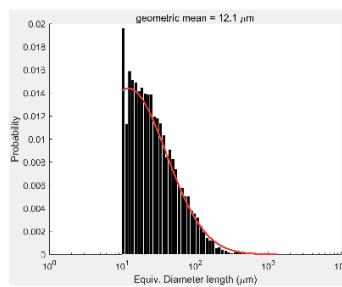
CH09-09B:



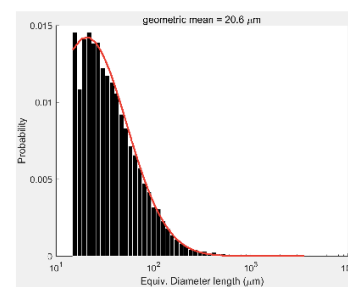
CH09-11ch:



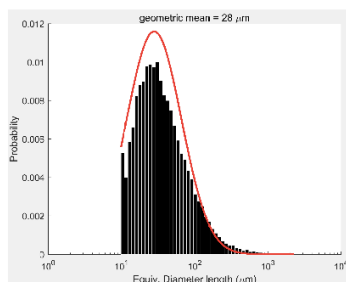
CH09-11fs:



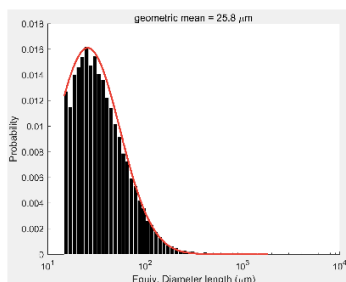
CH09-13ch-1:



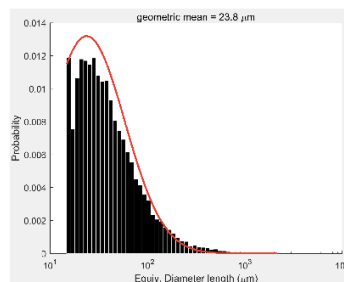
CH09-13ch-2:



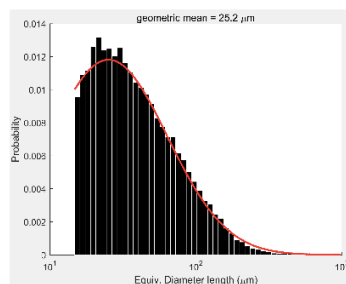
CH09-13fs:



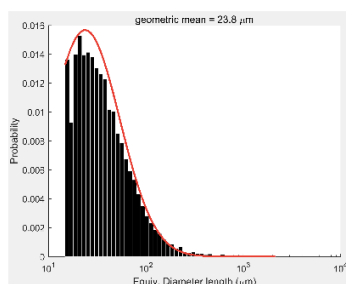
CH09-16ch:



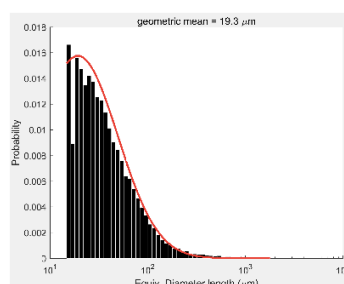
CH09-16fs:



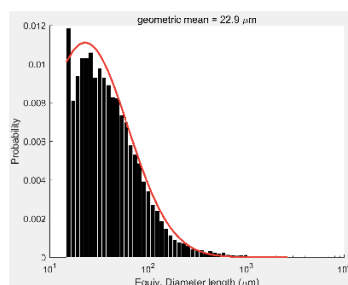
CH09-19ch-1:



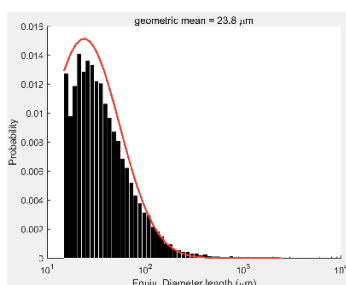
CH09-19ch-2:



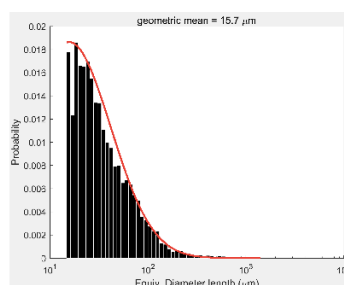
CH09-19fs:



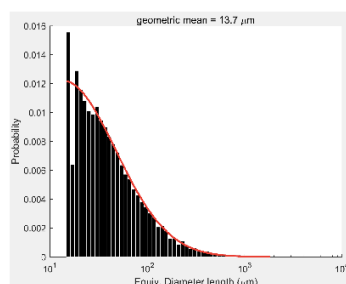
CH09-23ch:



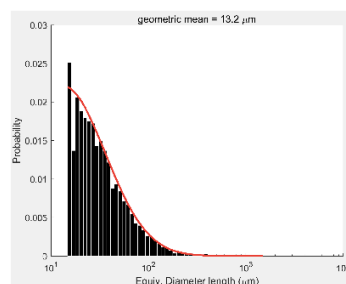
CH09-23fs:



CH09-40ch:



CH09-40fs:



CH09-41ch:

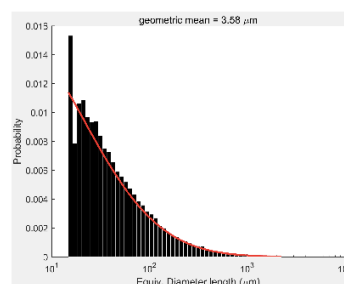


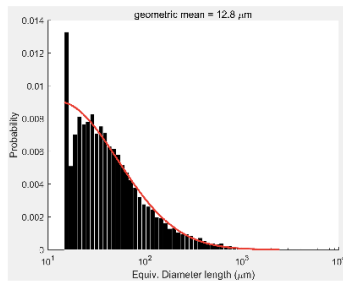
Figure 1 is a histogram showing the probability distribution of the equivalent diameter length of the particles. The x-axis is labeled 'Equiv. Diameter length (µm)' and is on a logarithmic scale from 10^1 to 10^4 . The y-axis is labeled 'Probability' and ranges from 0 to 0.02. A red curve is overlaid on the black bars, representing a fitted distribution. The text 'geometric mean = 16.3 µm' is displayed in the upper right corner of the plot area.

Figure 1 is a histogram showing the probability distribution of the equivalent diameter length of the particles. The x-axis is labeled 'Equiv. Diameter length (μm)' and is on a logarithmic scale ranging from 10¹ to 10³. The y-axis is labeled 'Probability' and ranges from 0 to 0.018. A red curve is overlaid on the black bars, representing a fitted probability density function. The text 'geometric mean = 26.8 μm' is displayed in the upper right corner of the plot area.

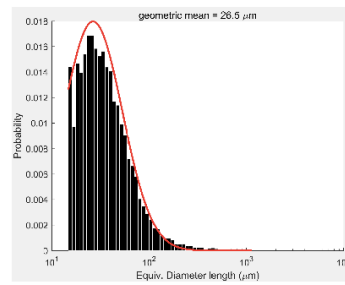
Figure 1 is a histogram showing the probability distribution of Equus diameter lengths. The x-axis is labeled 'Equis Diameter length (μm)' and ranges from 10¹ to 10⁴ on a logarithmic scale. The y-axis is labeled 'Probability' and ranges from 0 to 0.014. A red curve is overlaid on the histogram, representing a geometric mean fit. The text 'geometric mean = 22.5 μm' is displayed at the top of the plot area.

Figure 1 is a histogram showing the probability distribution of particle diameter lengths. The x-axis is labeled 'Diameter length (μm)' and is on a logarithmic scale from 10^1 to 10^4 . The y-axis is labeled 'Probability' and ranges from 0 to 0.014. The histogram consists of vertical black bars. A red curve is overlaid on the histogram, representing a geometric fit. The text 'geometric mean = 27.9 μm' is displayed above the curve.

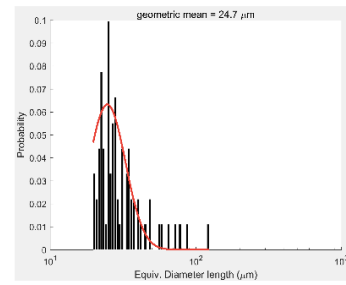
CH09-68ch:



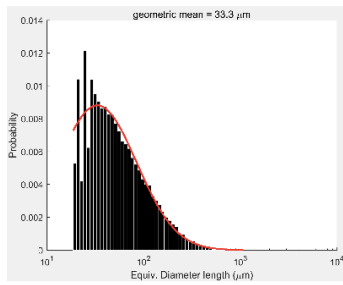
CH09-68fs:



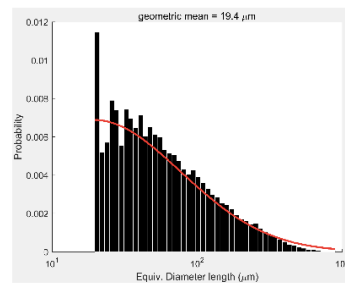
HD09-11b:



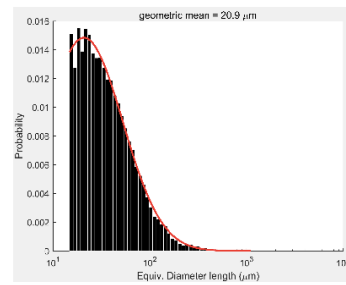
HD09-27:



HD09-28:

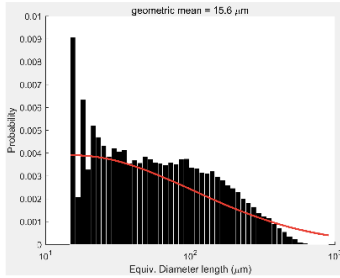


HD09-29:

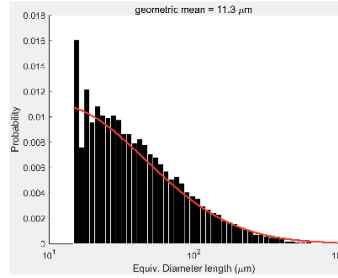


Plagioclase Feldspar

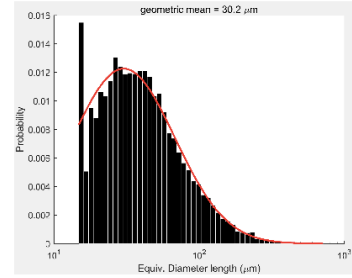
AF09-3A:



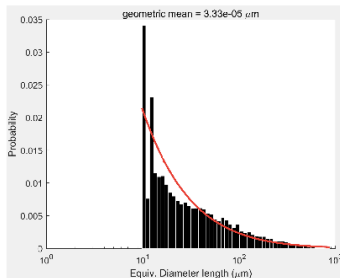
AF09-12:



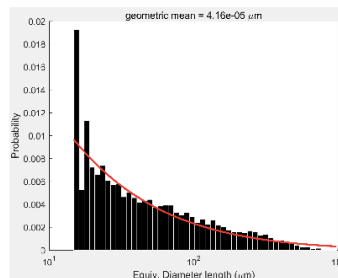
AF09-15



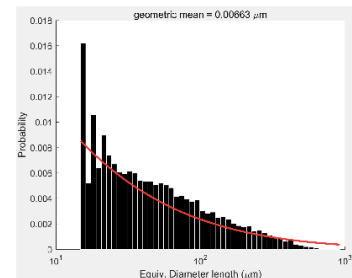
AF09-19:



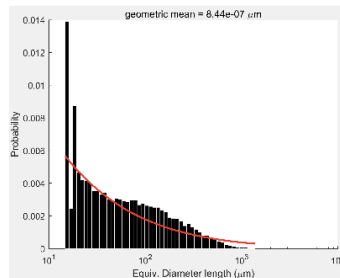
CH09-08A:



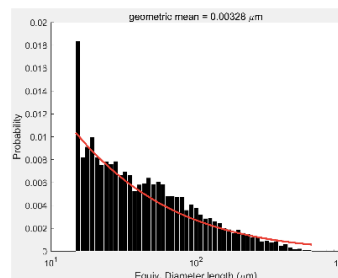
CH09-08B:



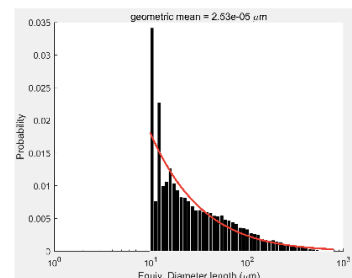
CH09-08C:



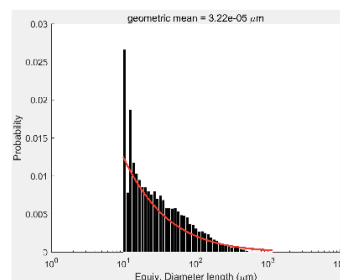
CH09-09A:



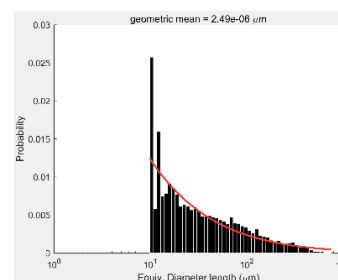
CH09-09B:



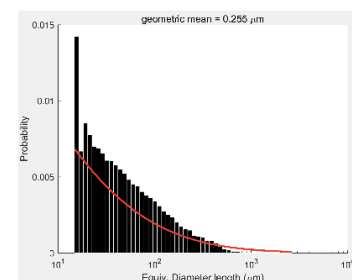
CH09-11ch:



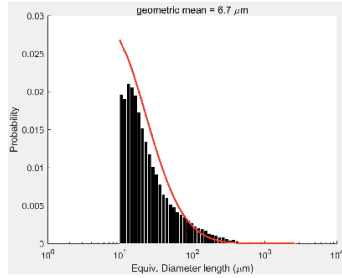
CH09-11fs:



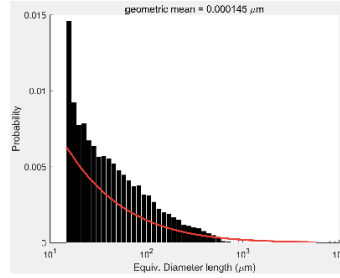
CH09-13ch-1:



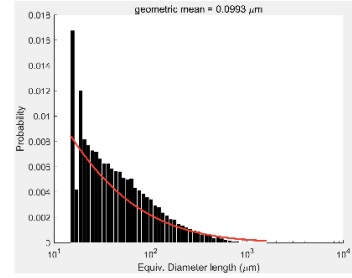
CH09-13ch-2:



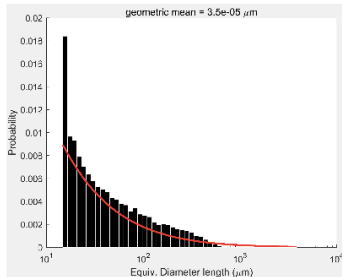
CH09-13fs:



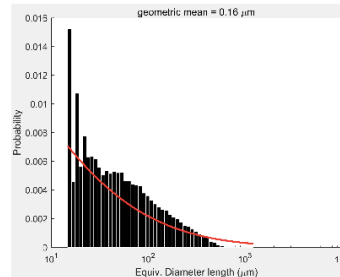
CH09-16ch:



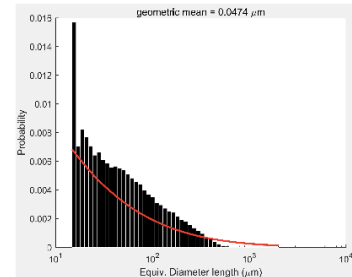
CH09-16fs:



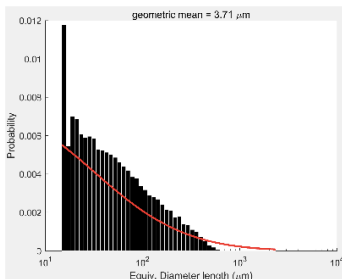
CH09-19ch-1:



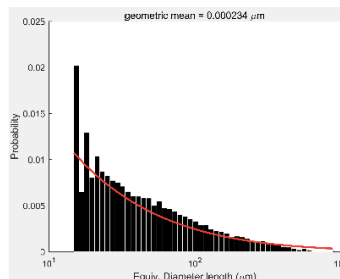
CH09-19ch-2:



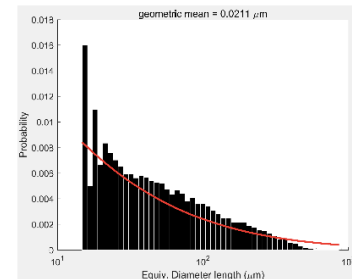
CH09-19fs:



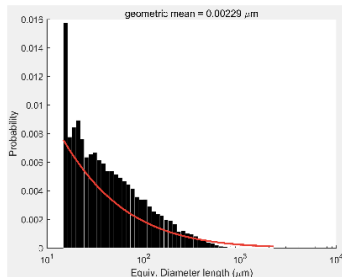
CH09-23ch:



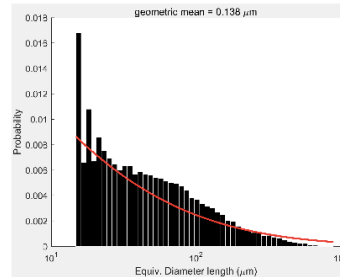
CH09-23fs:



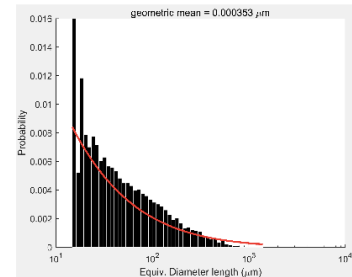
CH09-40ch:



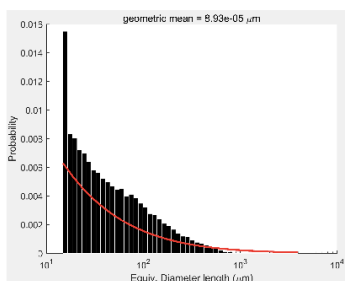
CH09-40fs:



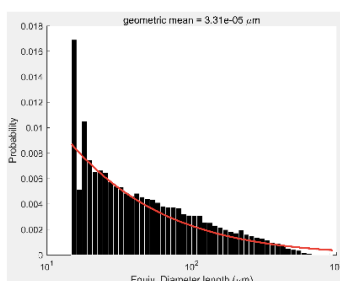
CH09-41ch:



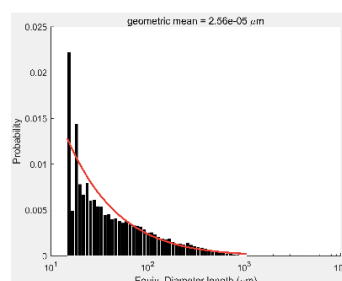
CH09-41fs:



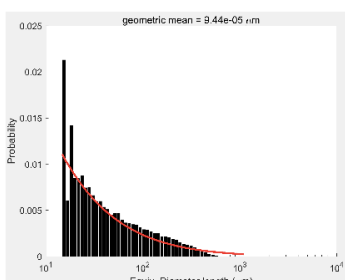
CH09-43fs:



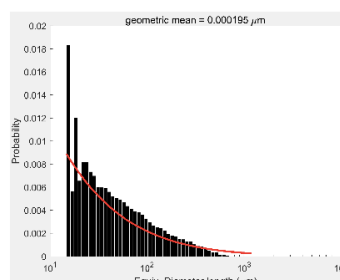
CH09-44ch:



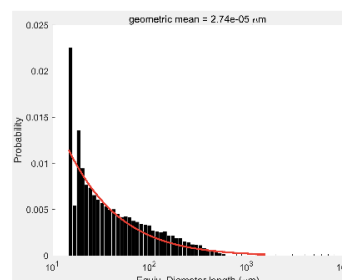
CH09-44fs:



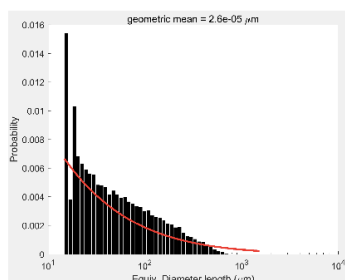
CH09-46fs:



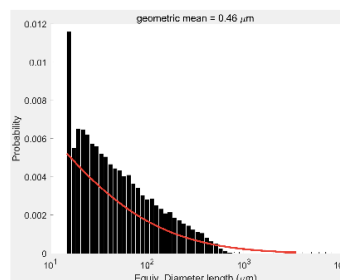
CH09-50ch:



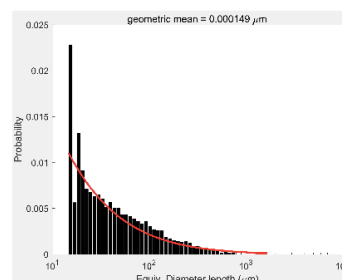
CH09-50fs:



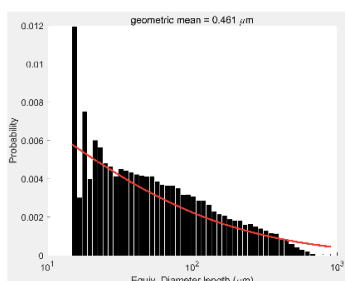
CH09-55fs:



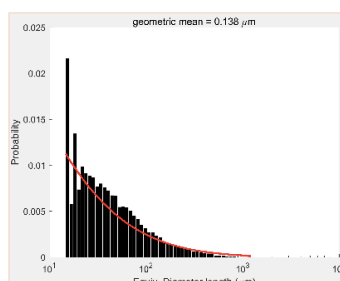
CH09-57ch:



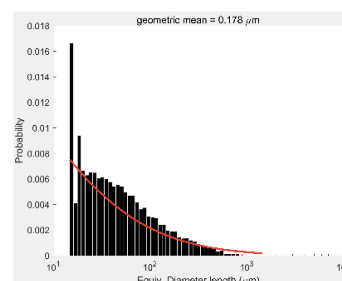
CH09-57fs:



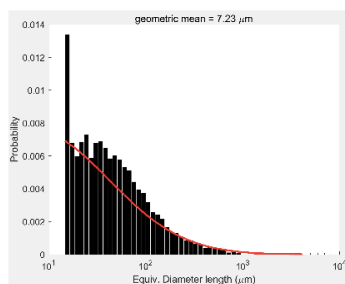
CH09-58ch:



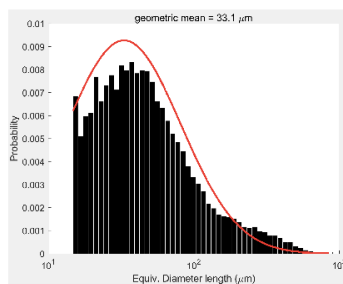
CH09-58fs:



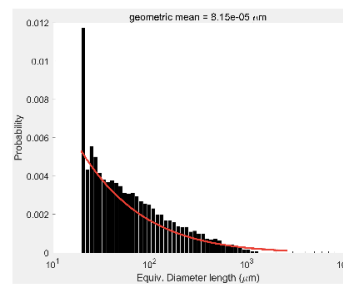
CH09-68ch:



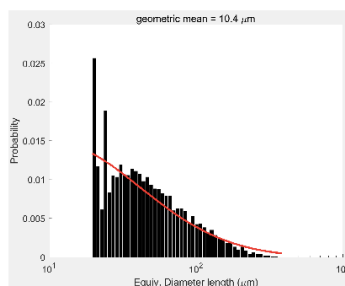
CH09-68fs:



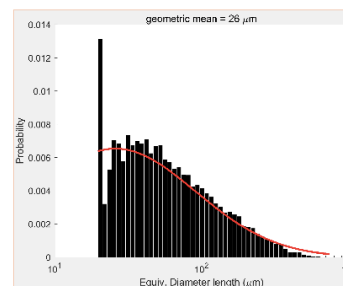
HD09-11b:



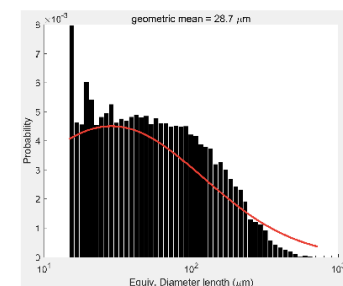
HD09-27:



HD09-28:

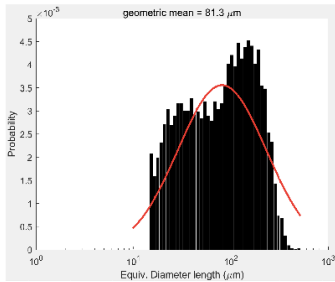


HD09-29:

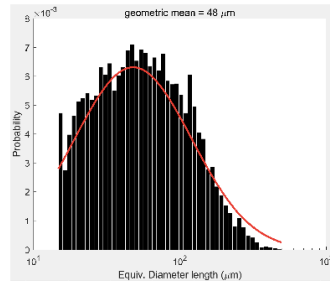


Enstatite

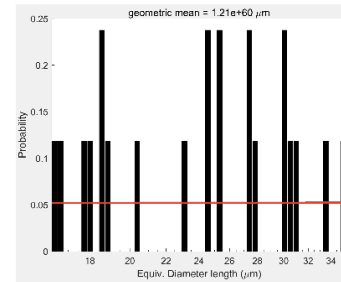
AF09-3A:



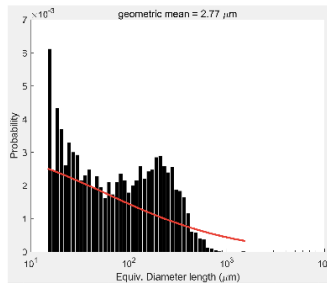
AF09-12:



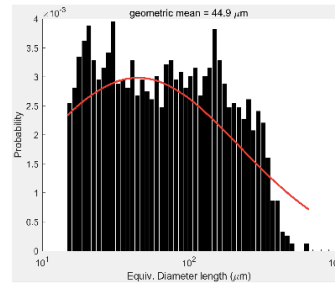
AF09-15:



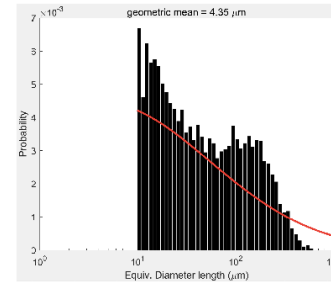
AF09-19:



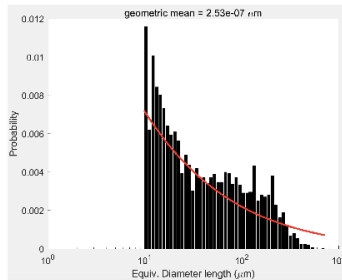
CH09-08A:



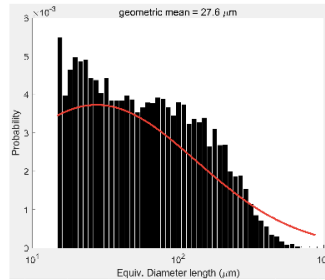
CH09-08B:



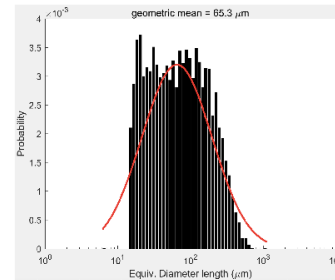
CH09-08C:



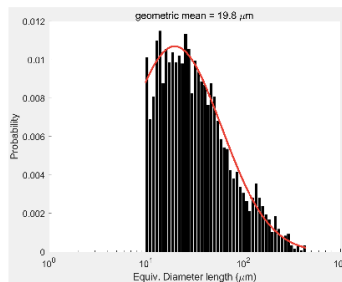
CH09-09A:



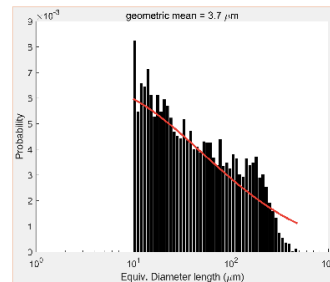
CH09-09B:



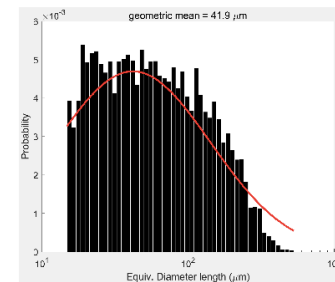
CH09-11ch:



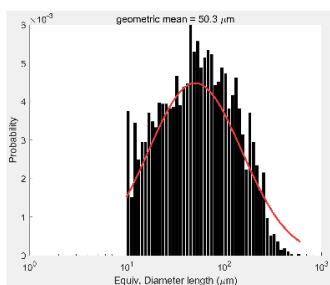
CH09-11fs:



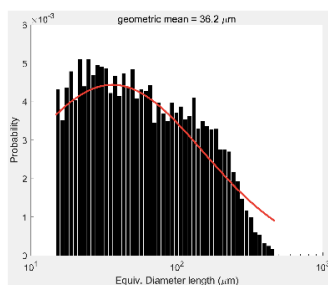
CH09-13ch-1:



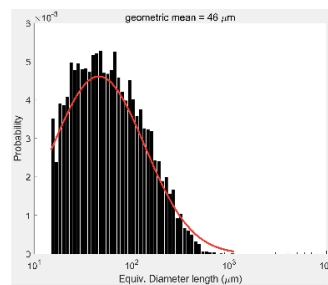
CH09-13ch-2:



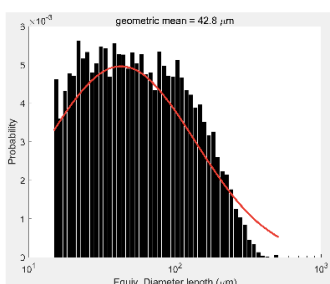
CH09-13fs:



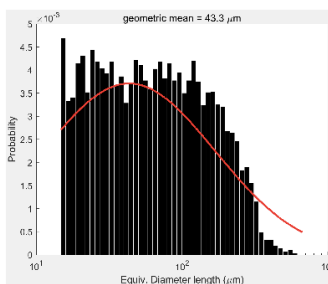
CH09-16ch:



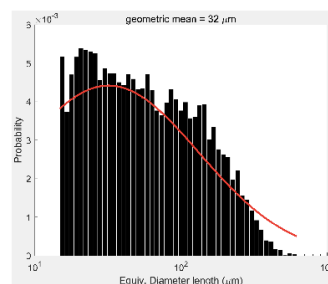
CH09-16fs:



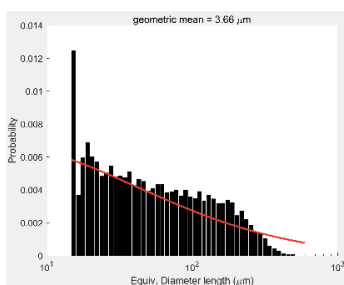
CH09-19ch-1:



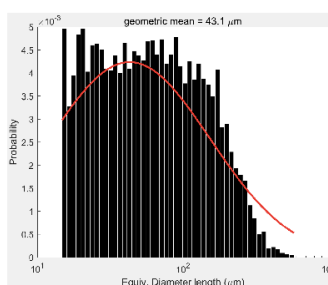
CH09-19ch-2:



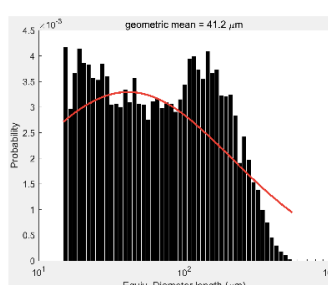
CH09-19fs:



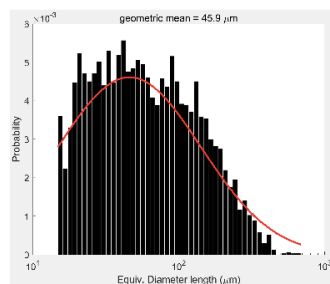
CH09-23ch:



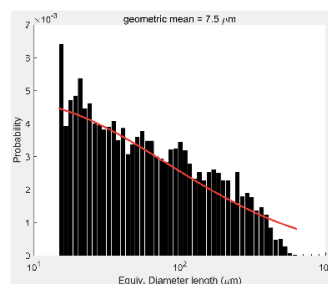
CH09-23fs:



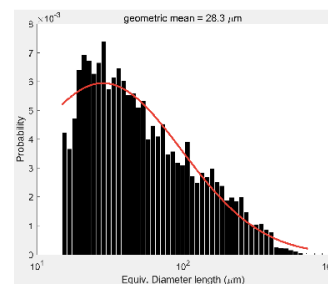
CH09-40ch:



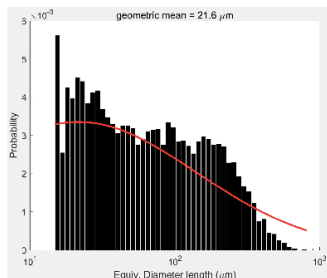
CH09-40fs:



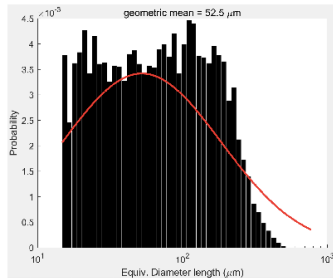
CH09-41ch:



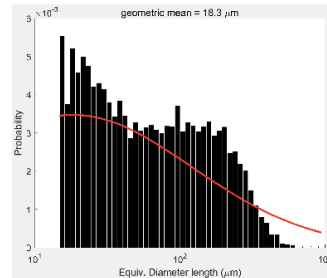
CH09-41fs:



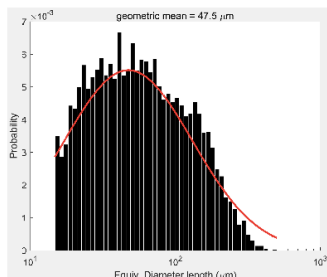
CH09-43fs:



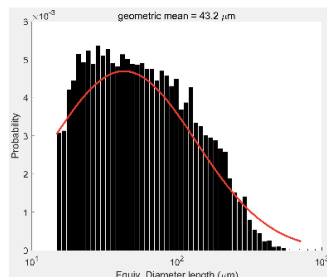
CH09-44ch:



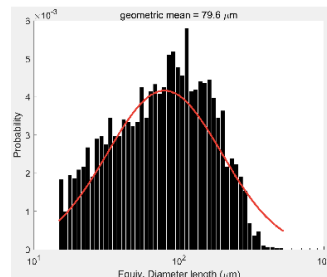
CH09-44fs:



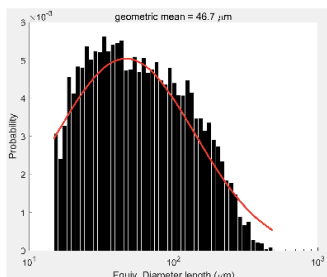
CH09-46fs:



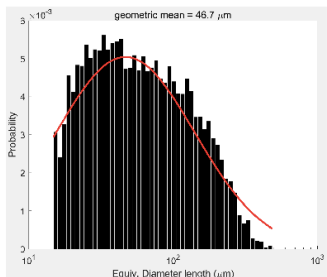
CH09-50ch:



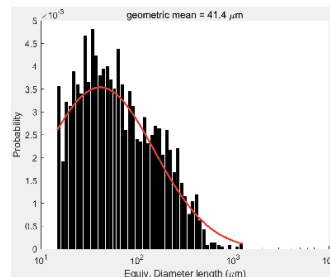
CH09-50fs:



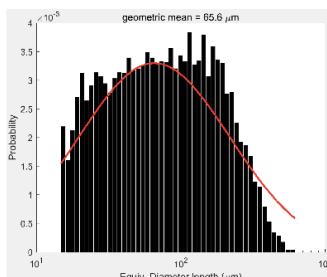
CH09-55fs:



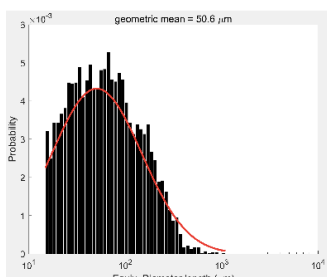
CH09-57ch:



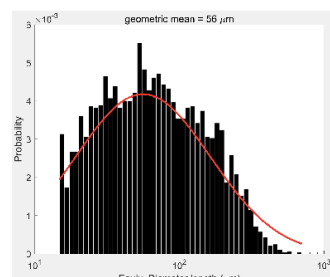
CH09-57fs:



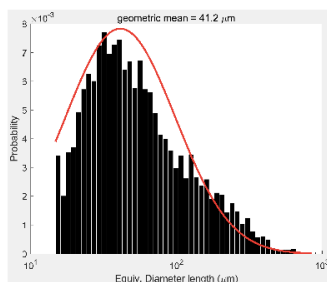
CH09-58ch:



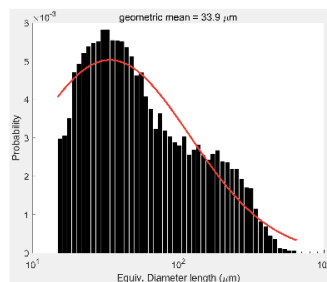
CH09-58fs:



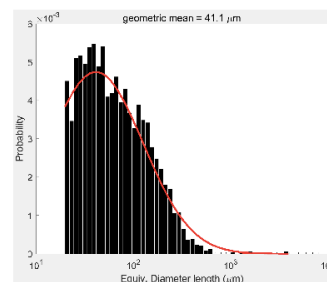
CH09-68ch:



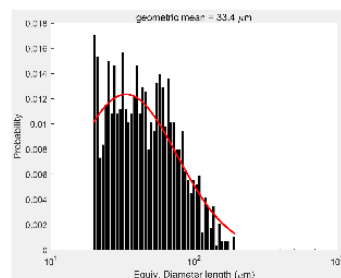
CH09-68fs:



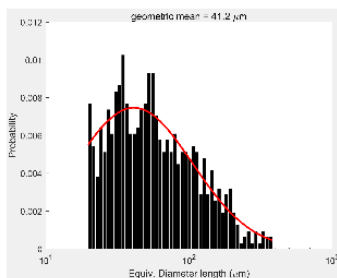
HD09-11b:



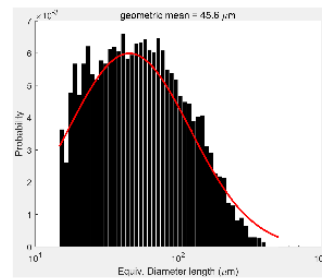
HD09-27:



HD09-28:

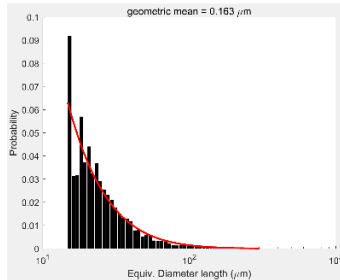


HD09-29:

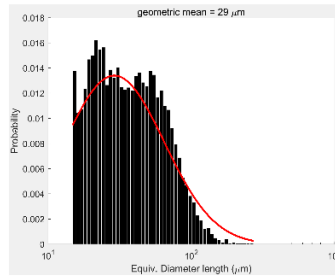


Diopside

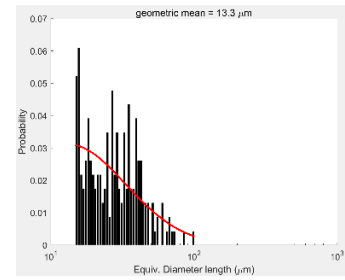
AF09-3A:



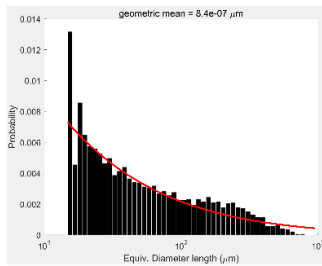
AF09-12:



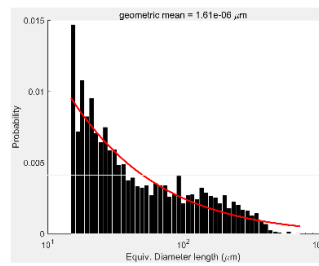
AF09-15:



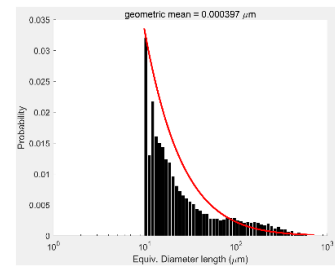
AF09-19:



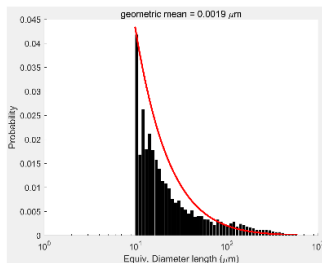
CH09-08A:



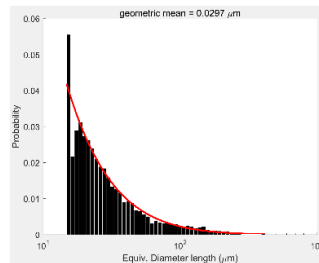
CH09-08B:



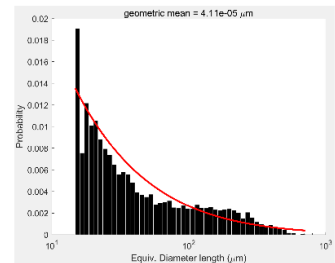
CH09-08C:



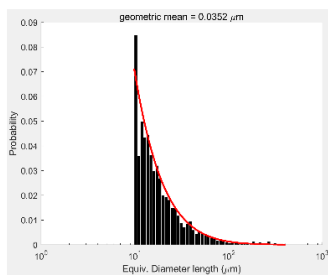
CH09-09A:



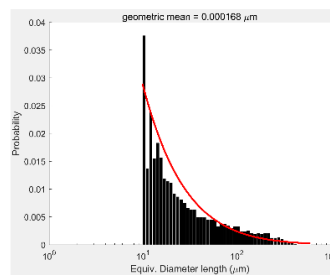
CH09-09B:



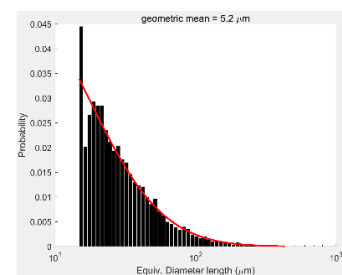
CH09-11ch:



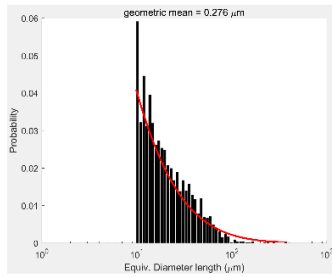
CH09-11fs:



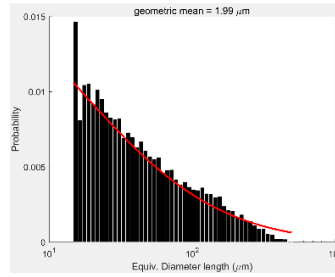
CH09-13ch-1:



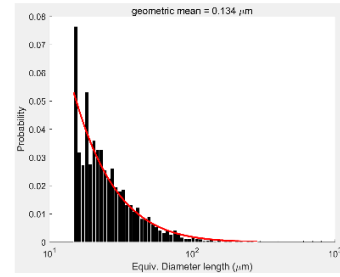
CH09-13ch-2:



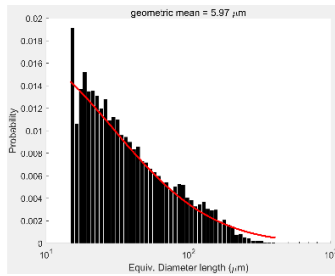
CH09-13fs:



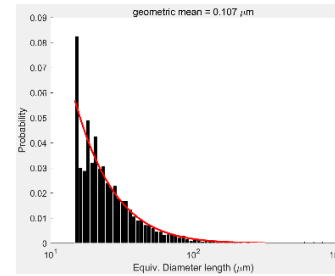
CH09-16ch:



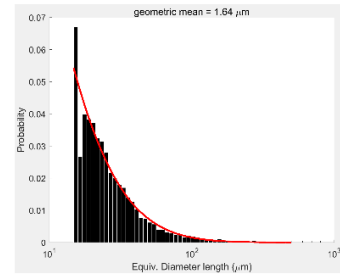
CH09-16fs:



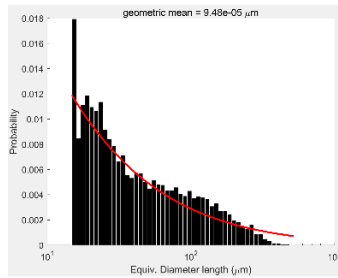
CH09-19ch-1:



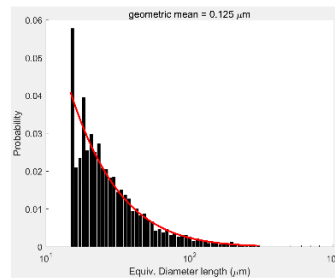
CH09-19ch-2:



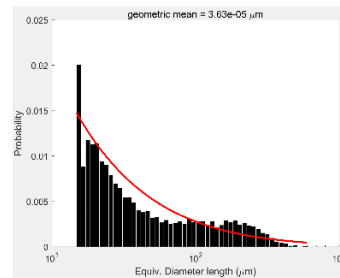
CH09-19fs:



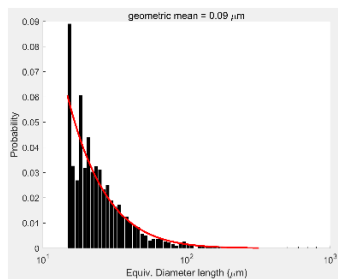
CH09-23ch:



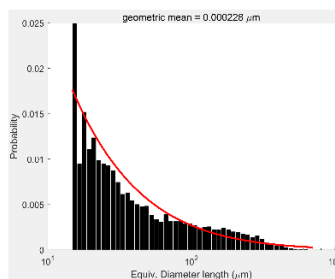
CH09-23fs:



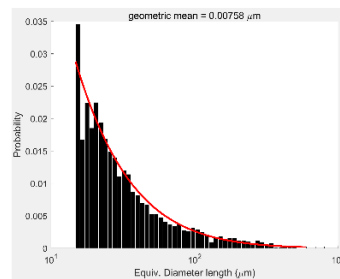
CH09-40ch:



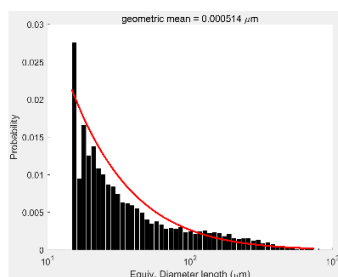
CH09-40fs:



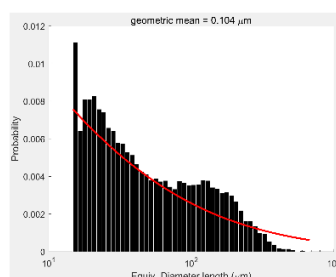
CH09-41ch:



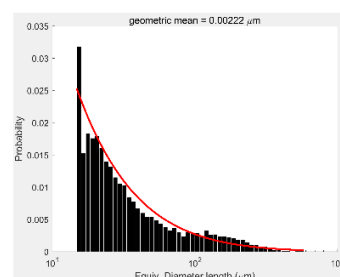
CH09-41fs:



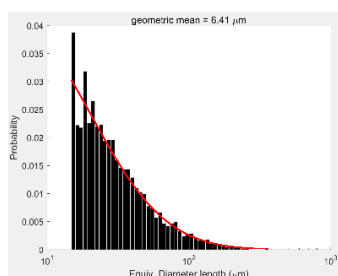
CH09-43fs:



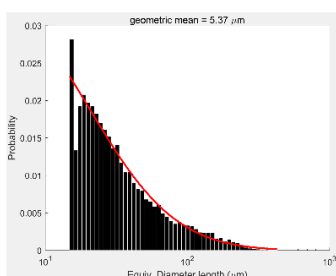
CH09-44ch:



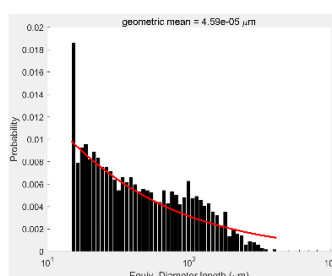
CH09-44fs:



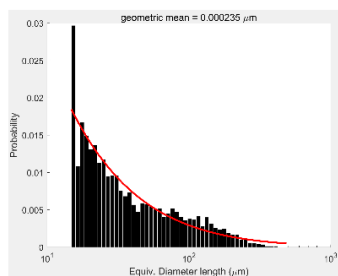
CH09-46fs:



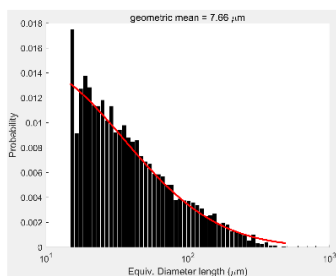
CH09-50ch:



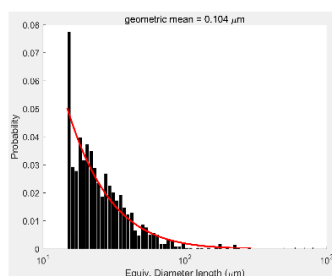
CH09-50fs:



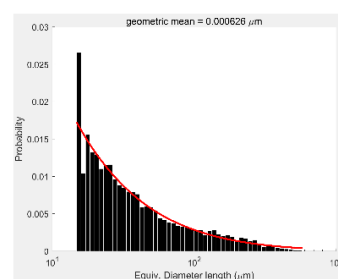
CH09-55fs:



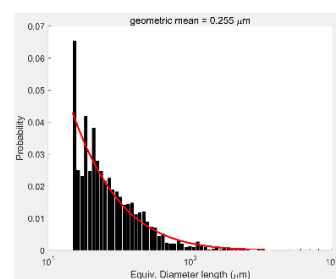
CH09-57ch:



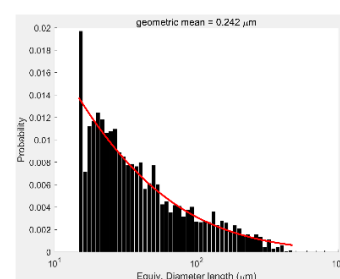
CH09-57fs:



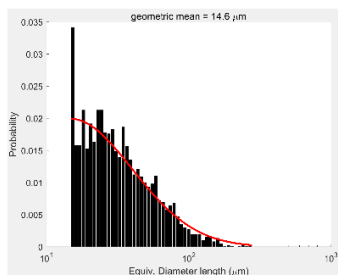
CH09-58ch:



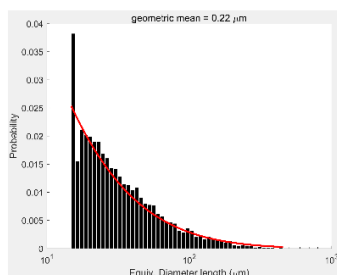
CH09-58fs:



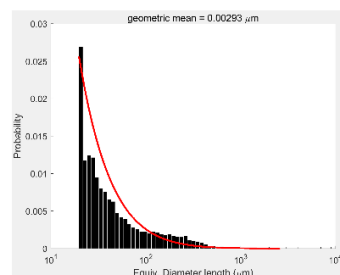
CH09-68ch:



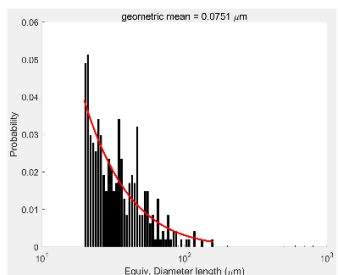
CH09-68fs:



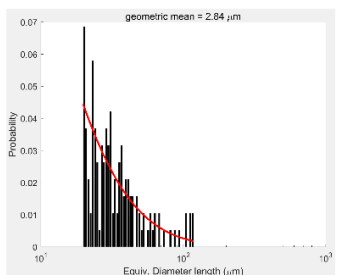
HD09-11b:



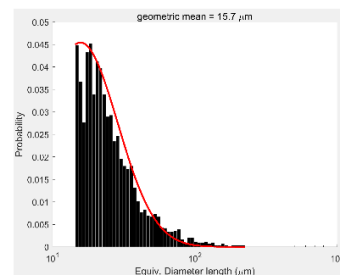
HD09-27:



HD09-28:



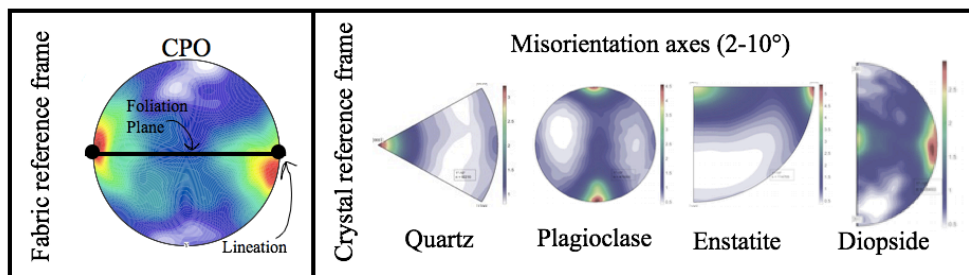
HD09-29:



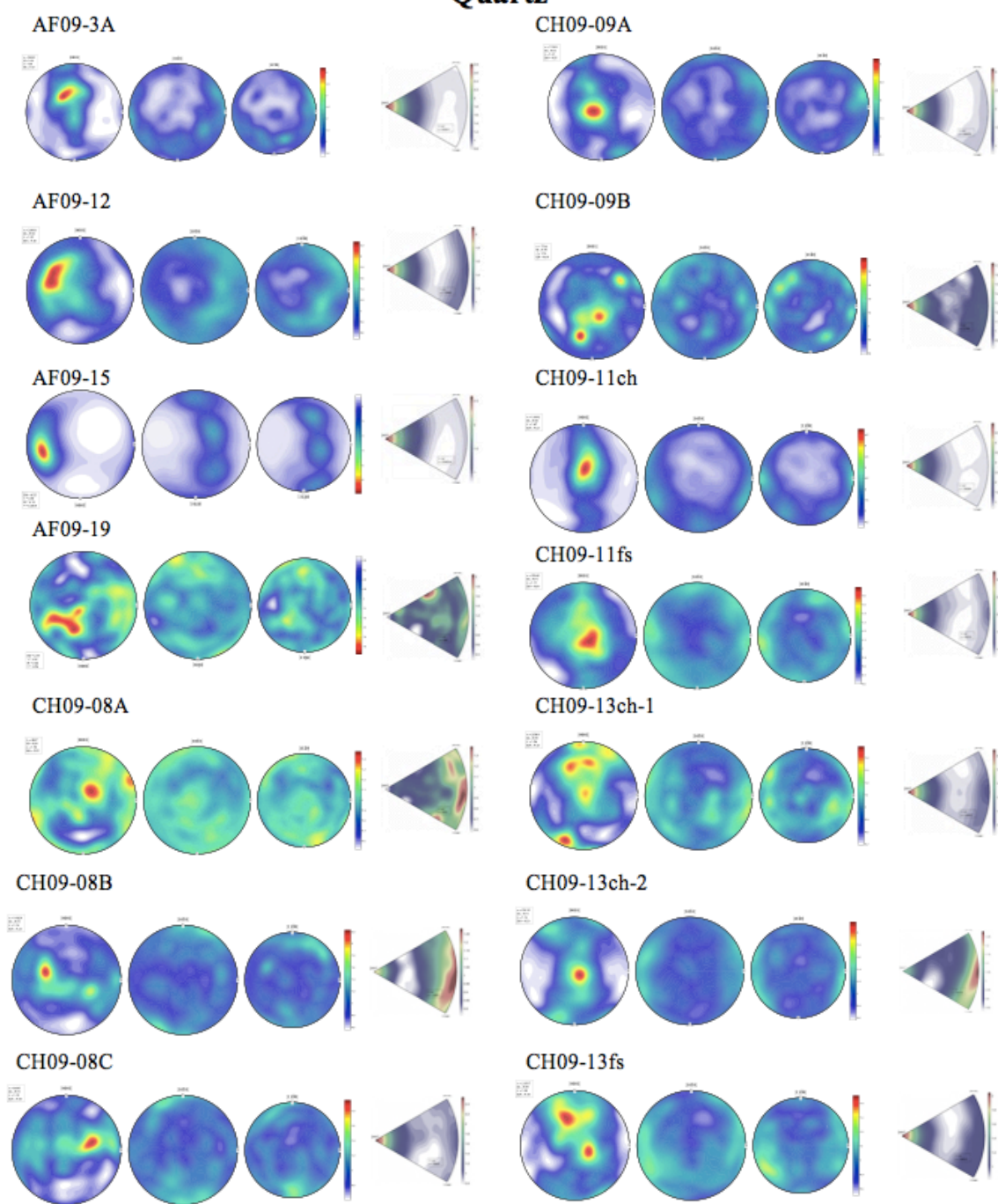
Appendix E.

Crystallographic Preferred Orientations and Misorientation Axes

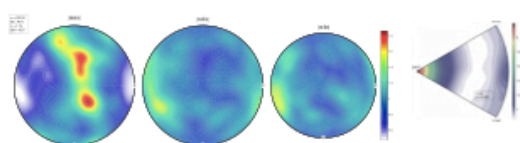
Note: Some samples do not have images for their misorientation axes. In these cases, the phase percentage was too low to calculate the misorientation axes



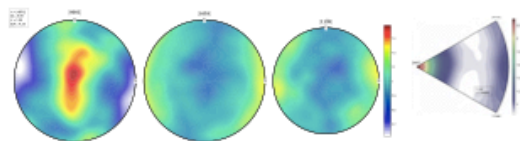
Quartz



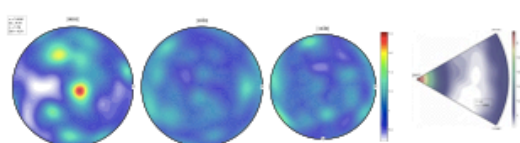
CH09-16ch



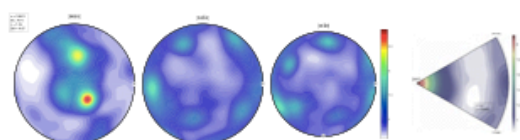
CH09-16fs



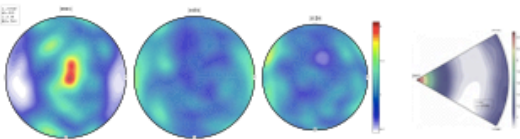
CH09-19ch-1



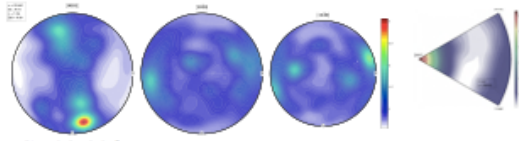
CH09-19ch-2



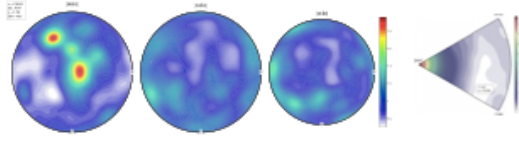
CH09-19fs



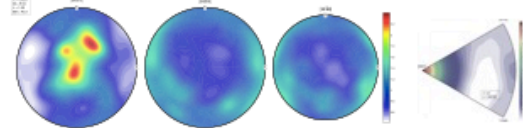
CH09-23ch



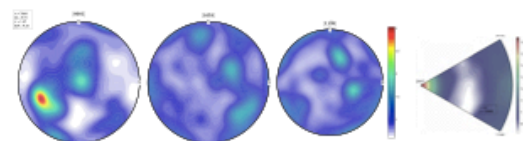
CH09-23fs



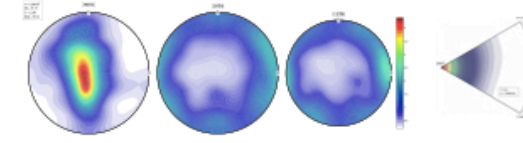
CH09-40ch



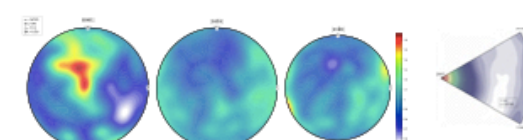
CH09-40fs



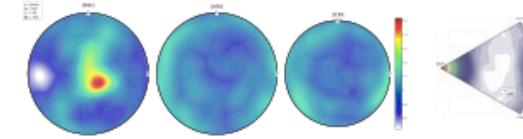
CH09-41ch



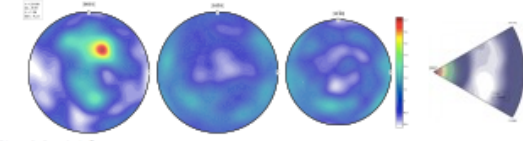
CH09-41fs



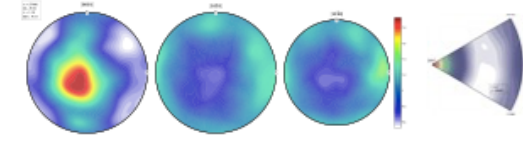
CH09-43fs



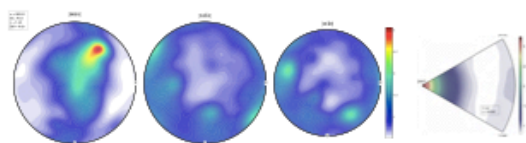
CH09-44ch



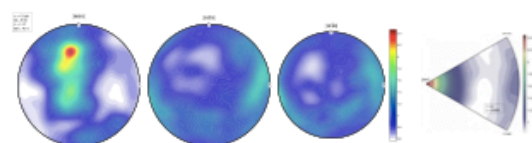
CH09-44fs



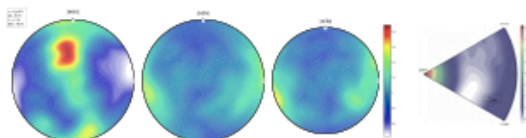
CH09-46fs



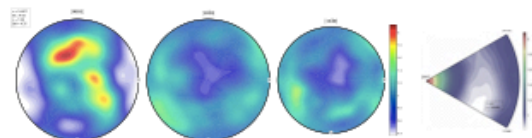
CH09-58fs



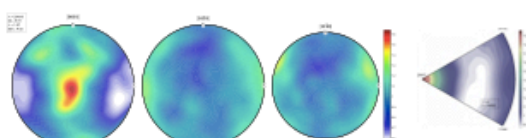
CH09-50ch



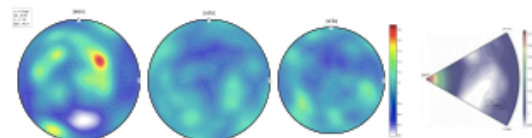
CH09-68ch



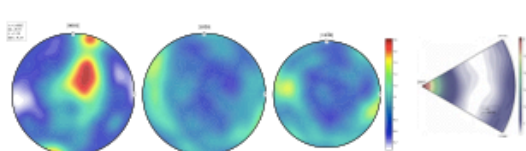
CH09-50fs



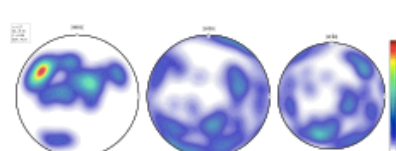
CH09-68fs



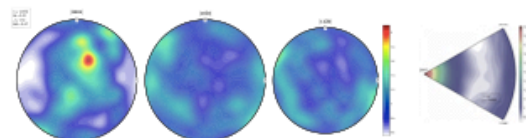
CH09-55fs



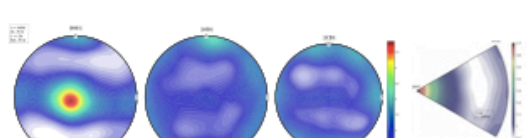
HD09-11b



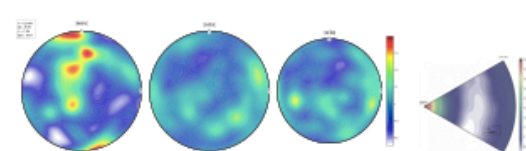
CH09-57ch



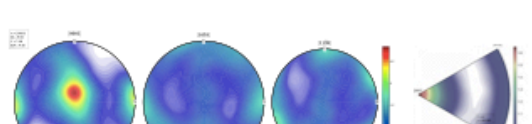
HD09-27



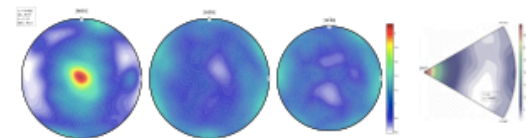
CH09-57fs



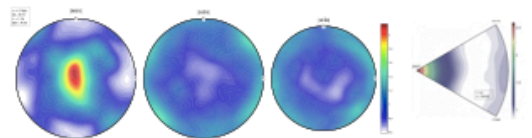
HD09-28



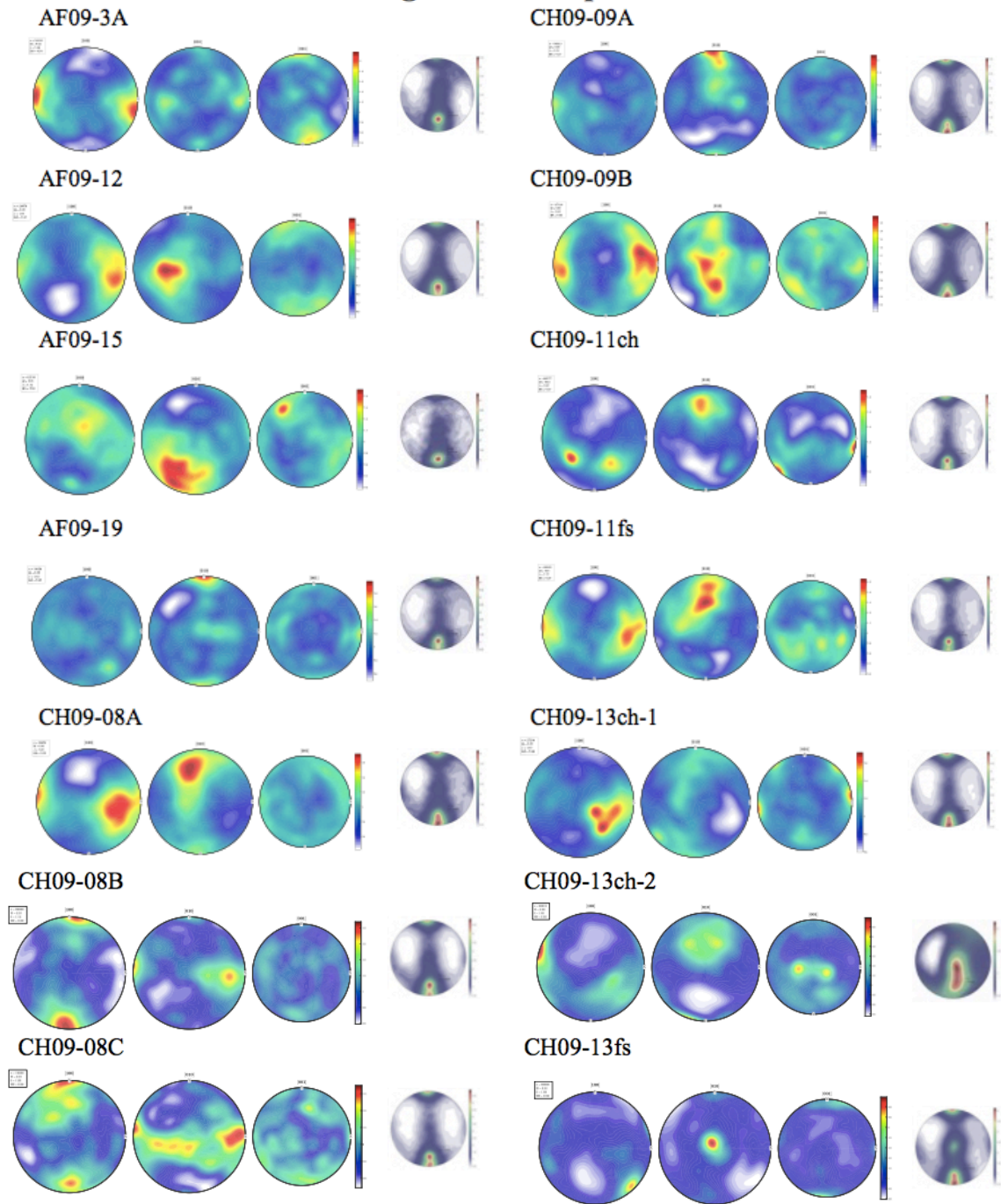
CH09-58ch



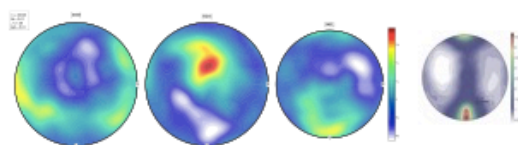
HD09-29



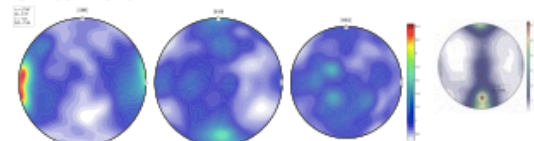
Plagioclase Feldspar



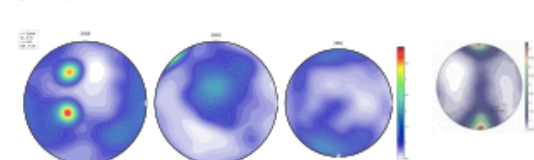
CH09-16ch



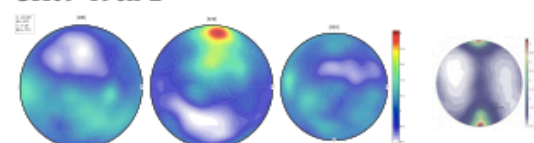
CH09-16fs



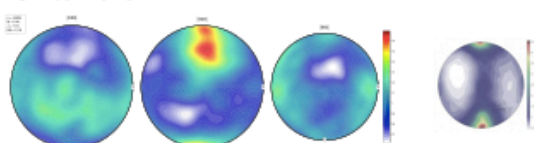
CH09-19ch-1



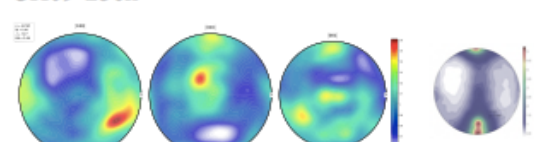
CH09-19ch-2



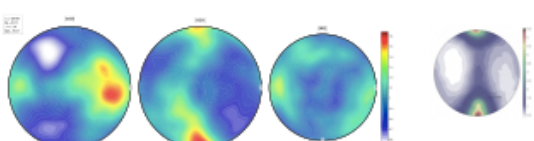
CH09-19fs



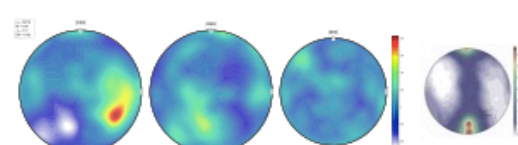
CH09-23ch



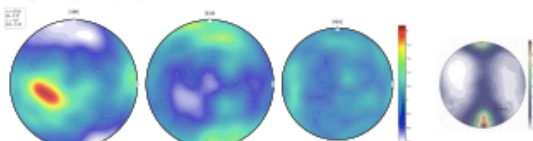
CH09-23fs



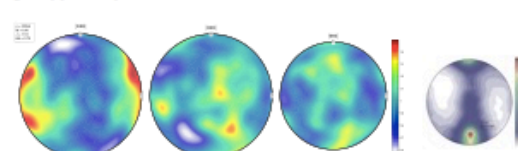
CH09-40ch



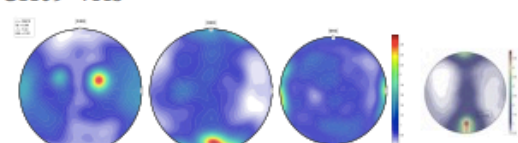
CH09-40fs



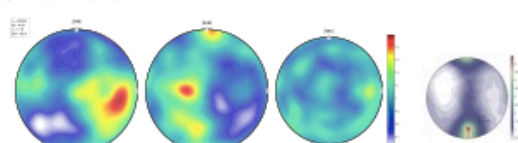
CH09-41ch



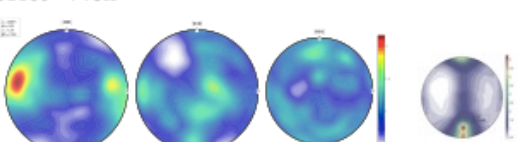
CH09-41fs



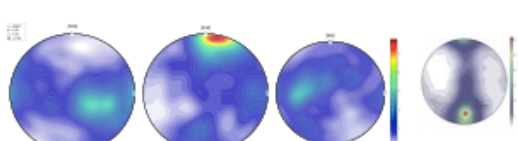
CH09-43fs



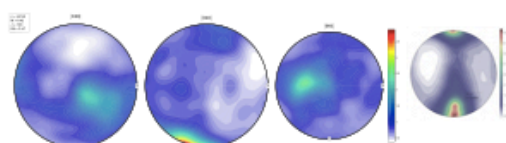
CH09-44ch



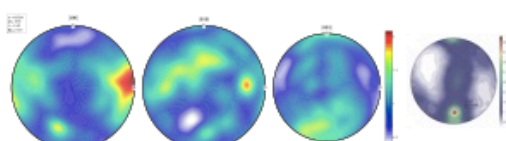
CH09-44fs



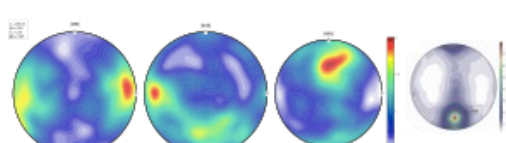
CH09-46fs



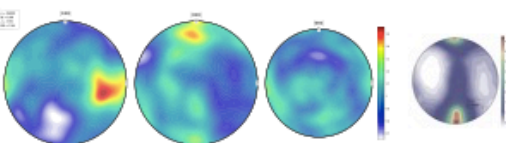
CH09-50ch



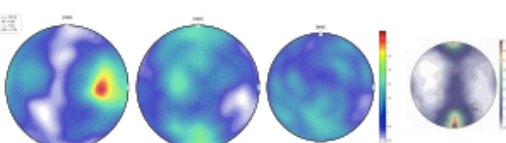
CH09-50fs



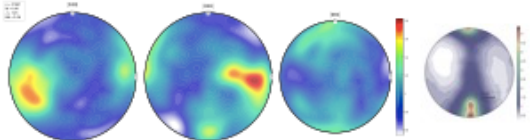
CH09-55fs



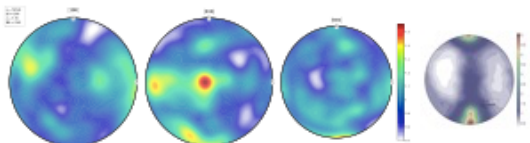
CH09-57ch



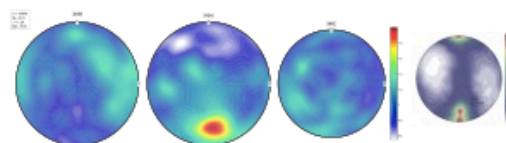
CH09-57fs



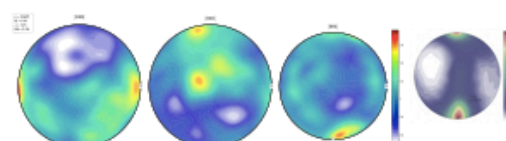
CH09-58ch



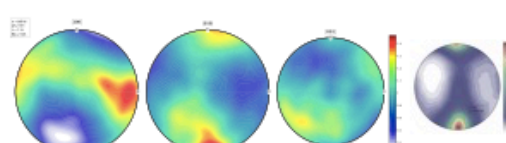
CH09-58fs



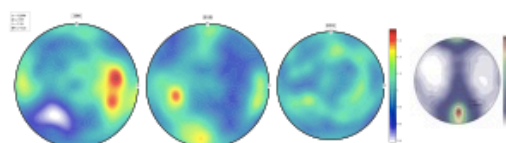
CH09-68ch



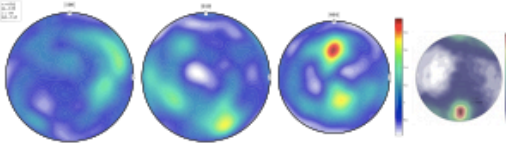
CH09-68fs



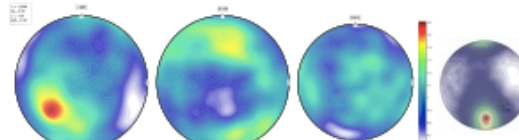
HD09-11b



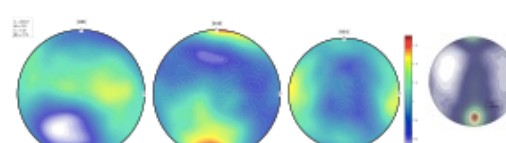
HD09-27



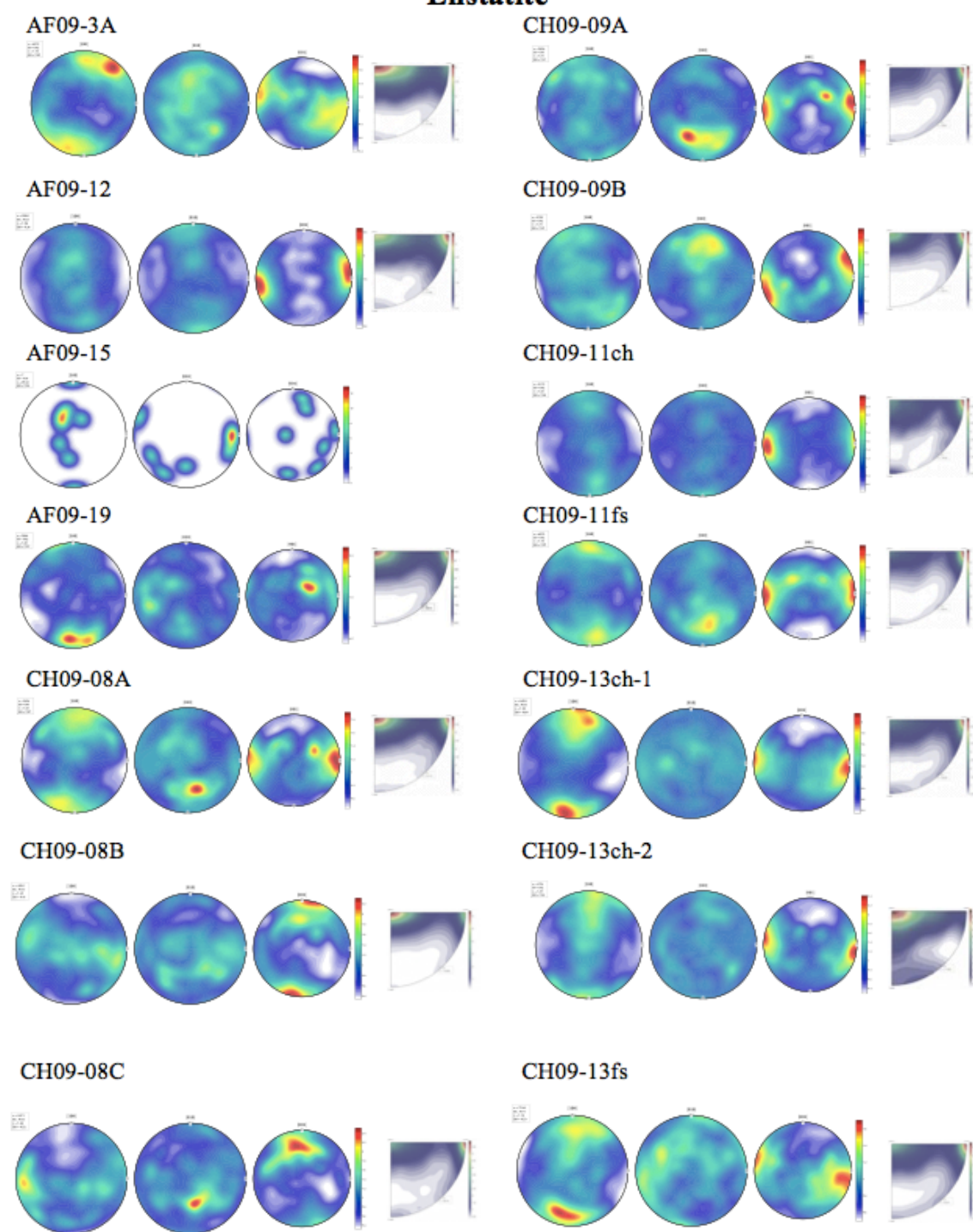
HD09-28



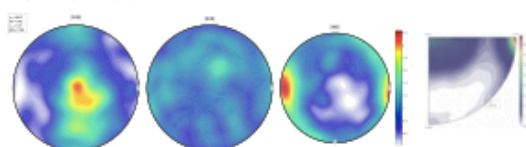
HD09-29



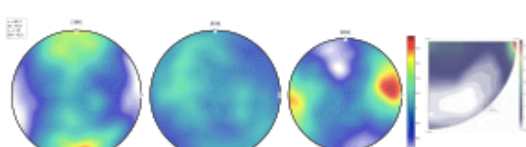
Enstatite



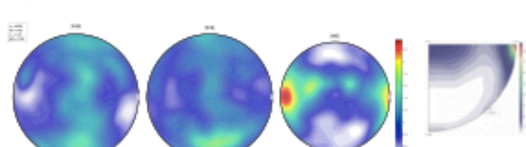
CH09-16ch



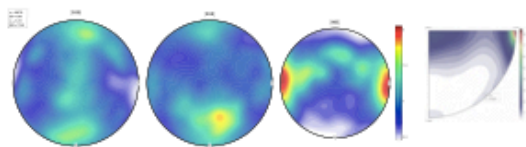
CH09-16fs



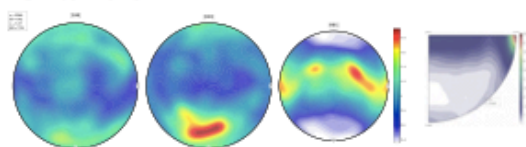
CH09-19ch-1



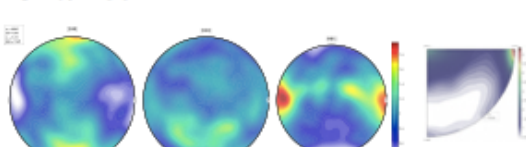
CH09-19ch-2



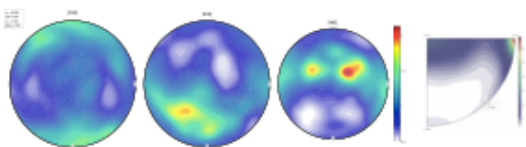
CH09-19fs



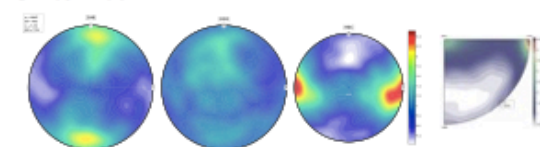
CH09-23ch



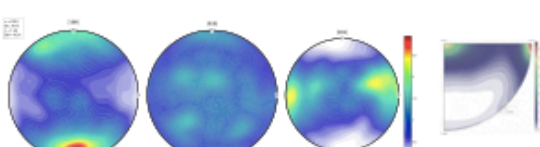
CH09-23fs



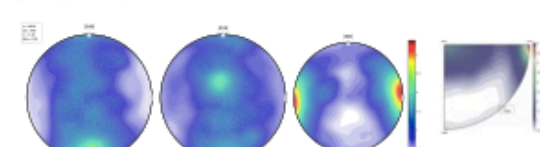
CH09-40ch



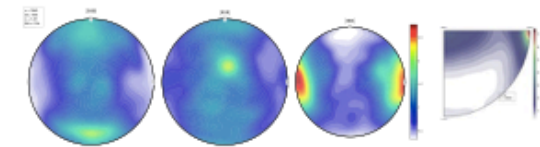
CH09-40fs



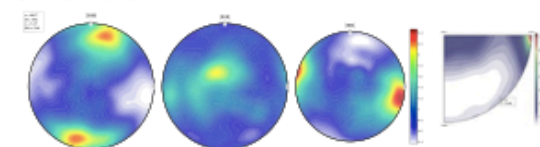
CH09-41ch



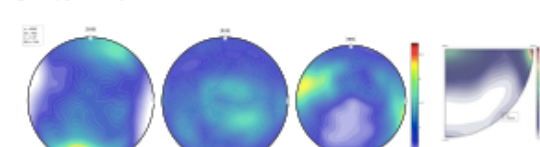
CH09-41fs



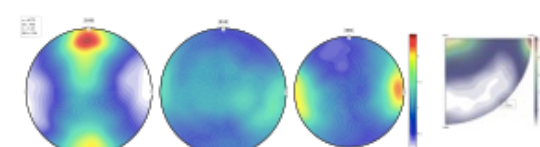
CH09-43fs

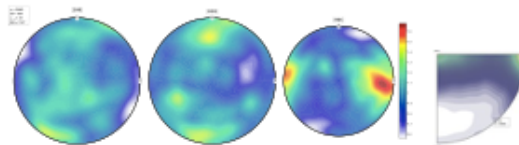
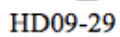
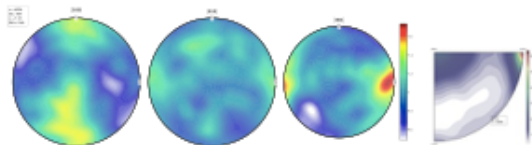
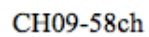
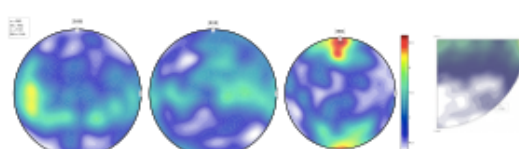
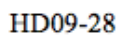
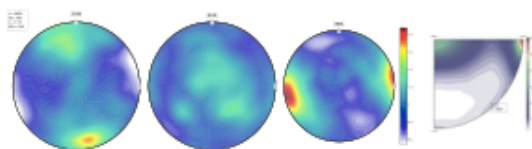
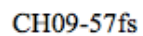
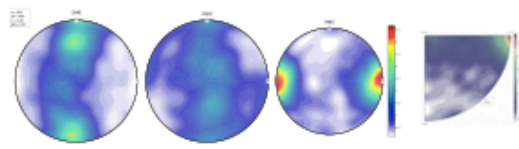
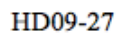
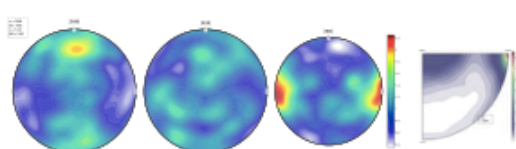
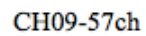
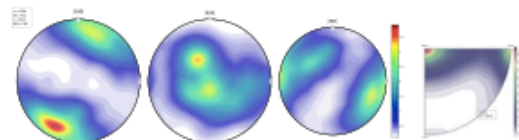
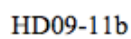
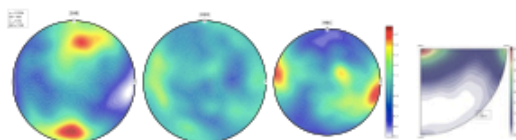
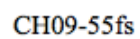
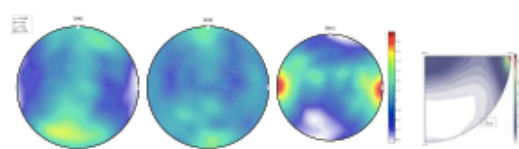
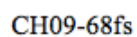
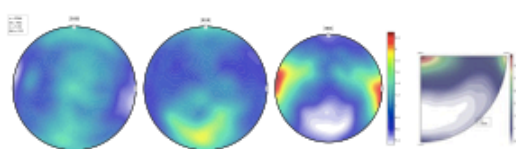
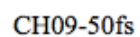
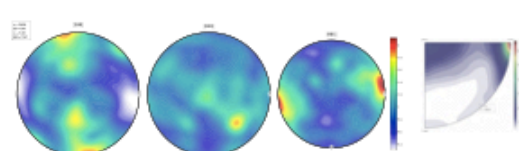
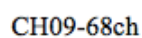
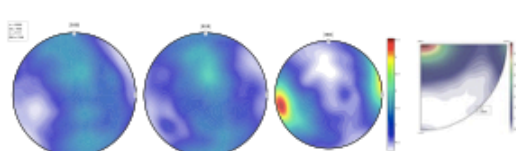
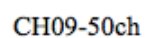
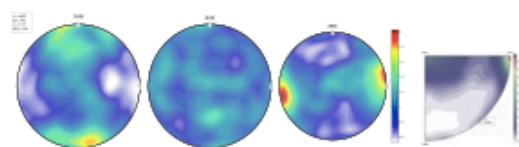
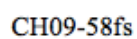
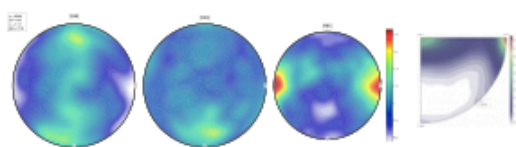
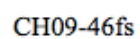


CH09-44ch

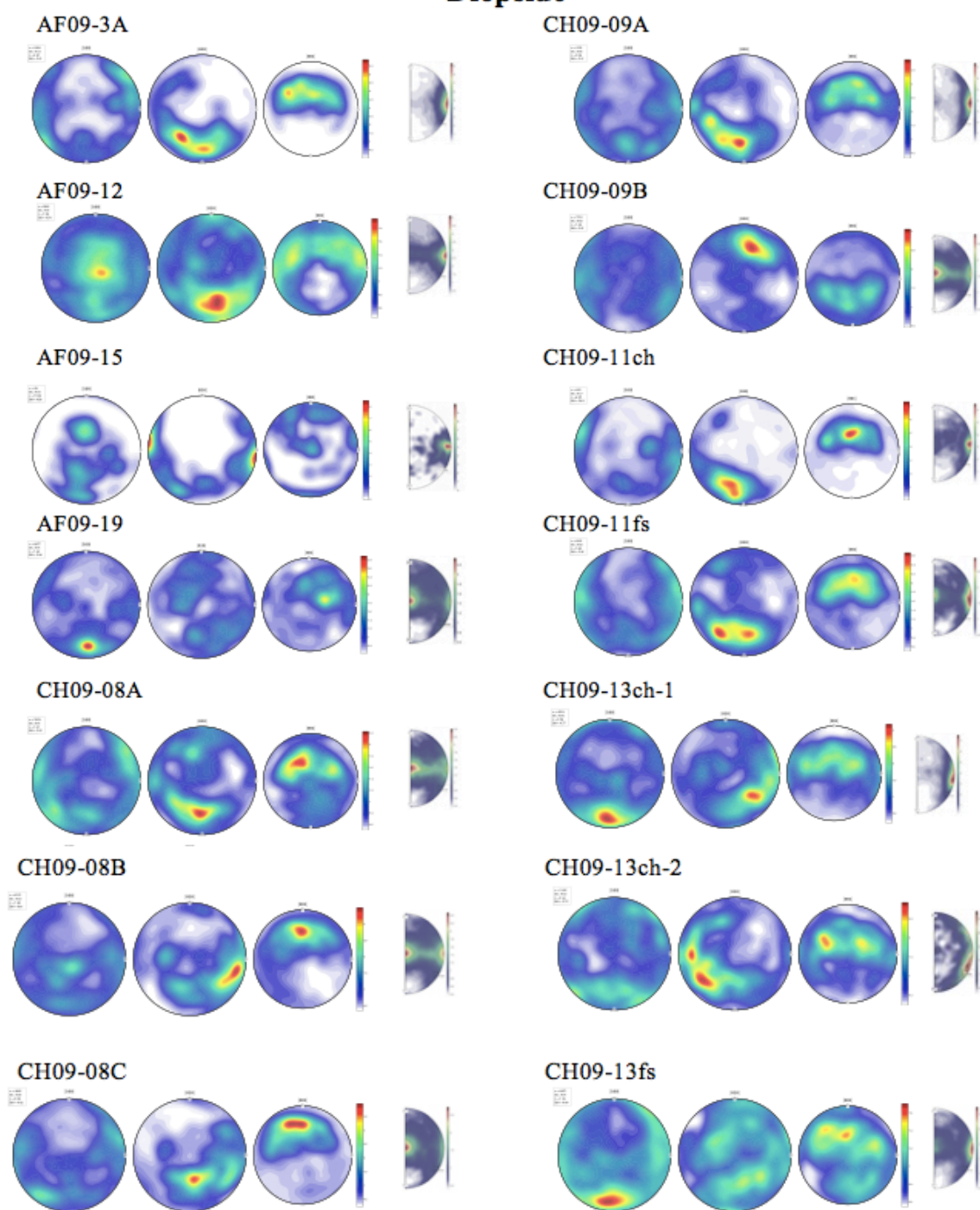


CH09-44fs

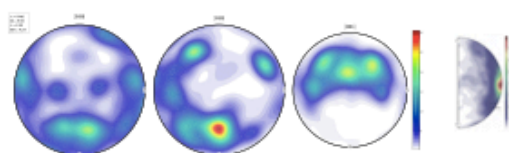




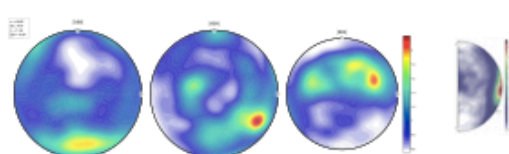
Diopside



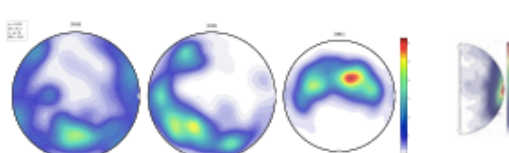
CH09-16ch



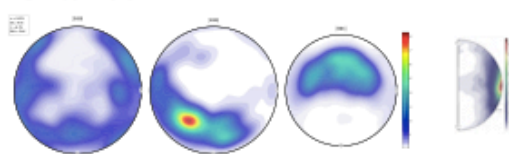
CH09-16fs



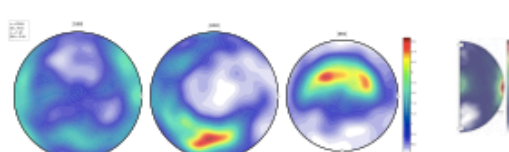
CH09-19ch-1



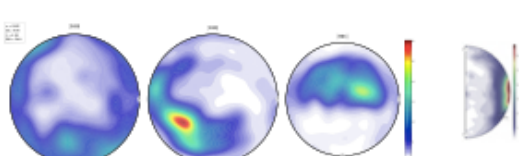
CH09-19ch-2



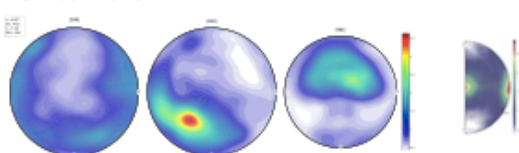
CH09-19fs



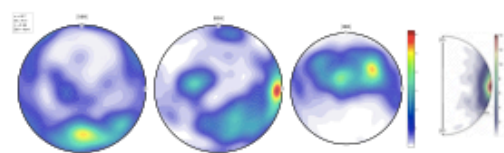
CH09-23ch



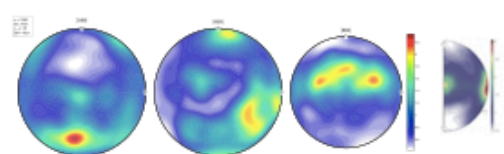
CH09-23fs



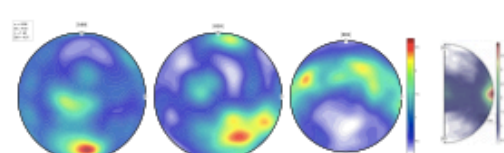
CH09-40ch



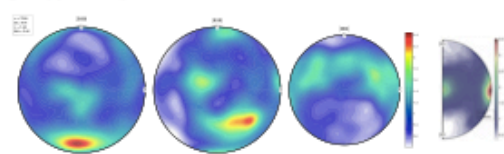
CH09-40fs



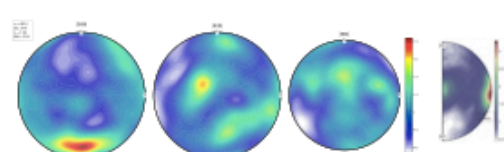
CH09-41ch



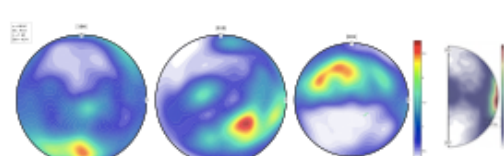
CH09-41fs



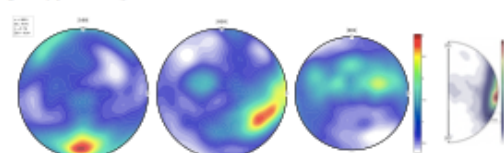
CH09-43fs

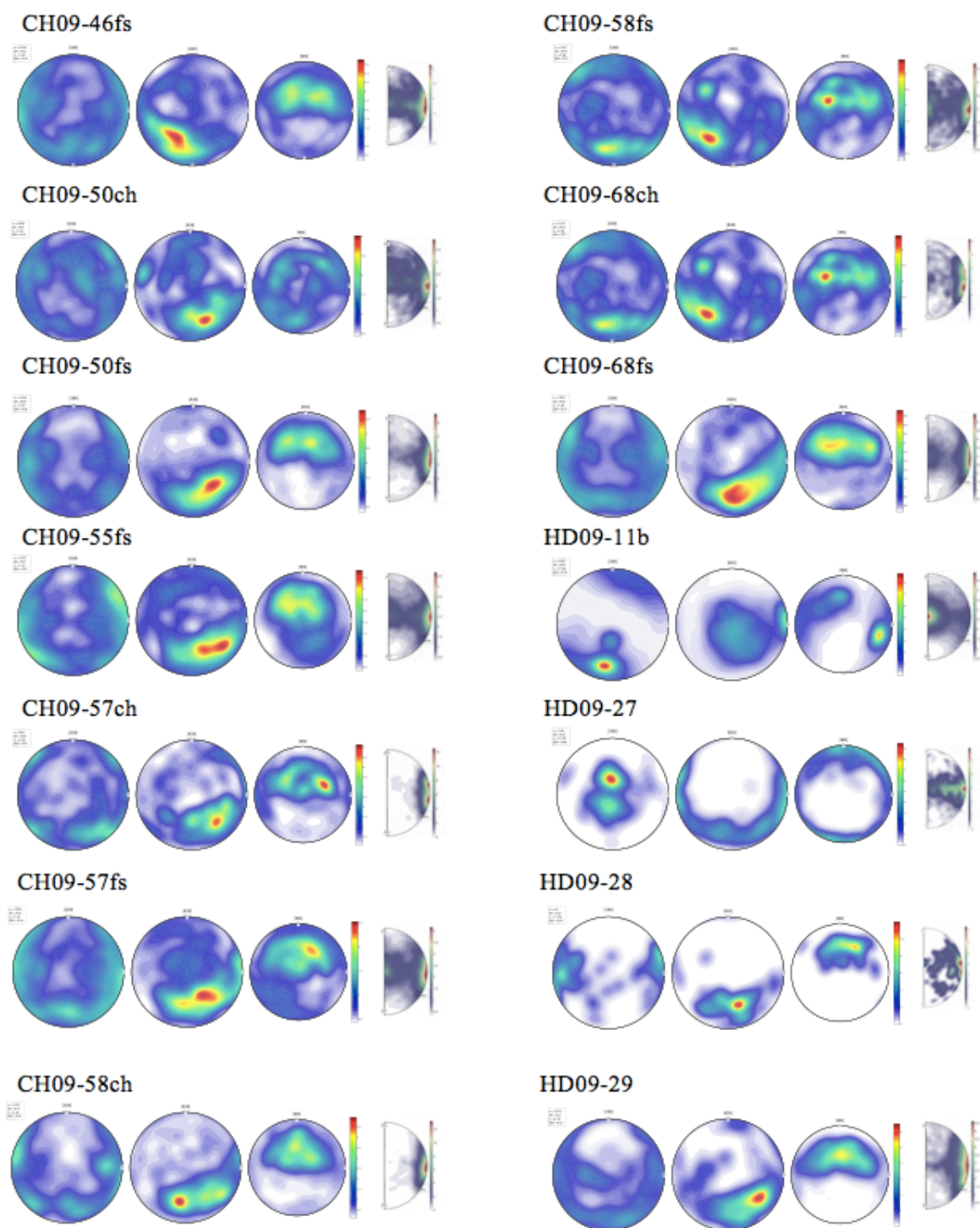


CH09-44ch



CH09-44fs





Appendix F.

Electron Microprobe Raw Data and Temperatures

Clinopyroxene Composition - in Weight Percent														Orthopyroxene Composition - in Weight Percent										Calculated Temperatures		
Sample Site, Pair	SiO2	TiO2	Al2O3	FeOt	MnO	MgO	CaO	Na2O	K2O	Cr2O3	Total	SiO2	TiO2	Al2O3	FeOt	MnO	MgO	CaO	Na2O	K2O	Cr2O3	Total	BK ^a 1990	T ^b 1998	P ^c 2008	
CH09-08A-1,1	51.43	0.10	2.24	9.68	0.14	12.99	22.39	0.38	0.01	0.07	99.42	50.96	0.03	1.39	27.93	0.54	18.61	0.31	0.00	-0.01	0.02	99.78	677.1	793.8	831.4	
CH09-08A-1,2	51.76	0.18	2.10	10.04	0.21	12.93	22.08	0.47	-0.02	0.05	99.81	50.72	0.07	1.37	27.89	0.52	18.43	0.42	0.00	0.00	0.02	99.44	699.7	817.6	840.7	
CH09-08A-1,3	51.24	0.19	2.32	10.03	0.20	12.71	22.35	0.42	0.02	0.09	99.56	50.49	0.05	1.45	27.92	0.50	18.65	0.53	0.00	0.00	0.03	99.62	690.9	803.1	836.0	
CH09-08A-2,1	51.70	0.19	2.12	9.86	0.23	13.11	22.34	0.47	0.01	0.09	100.12	50.37	0.04	1.53	27.97	0.50	18.43	0.41	0.01	-0.02	0.03	99.29	713.4	837.0	841.6	
CH09-08A-2,3	51.75	0.16	2.17	10.21	0.27	12.97	22.14	0.45	0.01	0.06	100.21	50.96	0.02	1.37	27.70	0.54	18.84	0.41	-0.01	0.01	0.02	99.87	708.5	823.7	844.6	
CH09-08A-3,1	51.16	0.17	2.19	9.58	0.17	13.06	22.13	0.46	-0.01	0.08	98.98	50.50	0.05	1.34	27.65	0.48	19.00	0.34	0.02	-0.01	0.05	99.41	694.6	805.8	844.7	
CH09-08A-3,2	51.72	0.21	2.55	10.37	0.18	12.68	21.81	0.46	0.00	0.08	100.06	50.29	0.04	1.31	27.88	0.49	18.79	0.34	-0.01	0.00	0.02	99.15	714.5	830.1	850.8	
CH09-08A-3,3	51.34	0.16	2.22	11.00	0.15	12.88	21.22	0.45	-0.02	0.10	99.50	50.57	0.02	1.38	28.00	0.46	18.62	0.42	0.00	0.00	0.04	99.51	764.3	891.1	886.1	
CH09-08A-3,4	51.69	0.18	2.32	10.35	0.21	12.57	22.03	0.48	-0.02	0.10	99.91	50.78	0.04	1.48	28.13	0.48	18.77	0.47	-0.02	-0.01	0.06	100.18	704.6	818.3	839.9	
CH09-11fs-1,2	51.88	0.14	2.33	9.64	0.17	13.05	21.84	0.44	0.00	0.10	99.59	50.89	0.04	1.55	27.16	0.55	18.73	0.42	0.00	0.00	0.04	99.37	729.7	854.2	848.0	
CH09-11fs-1,3	51.92	0.16	2.31	10.40	0.26	12.66	21.96	0.45	0.01	0.10	100.22	50.95	0.04	1.39	27.56	0.50	18.44	0.43	-0.01	-0.01	0.07	99.35	724.4	844.9	847.2	
CH09-11fs-1,4	51.48	0.25	2.51	10.04	0.20	12.58	21.81	0.54	0.00	0.15	99.56	51.28	0.05	1.48	27.32	0.53	18.55	0.42	0.00	0.00	0.01	99.64	710.9	820.6	842.7	
CH09-11fs-3,1	51.82	0.23	2.41	10.05	0.23	12.88	21.95	0.48	0.01	0.14	100.19	51.06	0.04	1.52	27.47	0.53	18.64	0.42	-0.01	-0.01	0.08	99.74	721.5	838.7	848.0	
CH09-11fs-3,2	51.53	0.27	2.64	10.03	0.13	12.65	21.95	0.44	0.02	0.14	99.79	50.60	0.04	1.55	27.54	0.51	18.79	0.43	-0.04	0.00	0.08	99.50	721.5	834.3	841.7	
CH09-11fs-3,4	51.39	0.20	2.95	9.51	0.17	12.69	21.75	0.46	0.00	0.19	99.30	50.91	0.04	1.75	27.06	0.52	18.81	0.41	-0.01	0.00	0.05	99.54	732.7	854.8	847.0	
CH09-11fs-4,2	52.17	0.16	2.44	10.16	0.22	12.62	21.93	0.48	-0.01	0.13	100.29	51.22	0.06	1.51	26.86	0.58	18.79	0.40	0.00	0.00	0.09	99.51	739.4	865.6	837.8	
CH09-11fs-4,3	51.76	0.19	2.35	9.82	0.18	12.80	22.00	0.46	0.00	0.13	99.67	50.96	0.05	1.53	27.60	0.55	19.02	0.40	0.01	0.01	0.09	100.22	699.9	814.3	840.0	
CH09-11fs-4,4	51.64	0.20	2.49	9.91	0.18	12.68	22.51	0.48	0.01	0.07	100.16	50.93	0.03	1.55	28.02	0.62	18.74	0.45	-0.01	-0.01	0.09	100.42	665.7	768.0	815.2	
CH09-13fs-1,1	50.72	0.19	2.33	11.68	0.25	11.99	21.71	0.38	0.00	0.02	99.27	49.71	0.05	1.50	29.88	0.61	17.18	0.42	0.00	0.01	-0.02	99.34	707.1	835.7	842.5	
CH09-13fs-1,2	51.00	0.13	2.07	10.78	0.26	12.49	22.28	0.38	0.01	0.00	99.41	50.37	0.00	1.40	30.09	0.68	16.83	0.35	-0.01	-0.02	-0.02	99.67	659.6	788.1	819.1	
CH09-13fs-1,3	51.07	0.17	2.18	11.46	0.24	12.05	21.94	0.44	-0.02	-0.04	99.49	50.39	0.03	1.56	29.81	0.59	17.60	0.39	0.01	-0.01	-0.01	100.34	686.5	809.8	832.4	
CH09-13fs-1,4	50.90	0.20	2.43	11.79	0.27	11.70	21.68	0.41	-0.01	0.05	99.43	50.05	0.09	1.52	29.84	0.62	16.76	0.41	0.02	-0.02	-0.03	99.26	704.8	834.0	838.7	
CH09-13fs-2,1	51.02	0.22	2.67	11.48	0.28	11.81	21.78	0.44	0.00	0.04	99.74	49.81	0.04	1.44	29.87	0.74	16.88	0.50	0.00	0.00	-0.03	99.24	701.5	825.7	824.2	
CH09-13fs-2,2	50.85	0.17	2.32	11.83	0.28	11.86	21.85	0.52	0.00	0.03	99.70	50.14	0.05	1.57	29.59	0.64	17.20	0.42	-0.05	0.00	0.03	99.59	721.1	851.8	828.5	
CH09-13fs-2,3	51.30	0.19	2.42	11.30	0.26	12.13	21.95	0.40	-0.01	0.03	99.96	50.23	0.05	1.42	29.24	0.52	17.43	0.46	0.00	-0.01	0.01	99.36	704.4	828.3	842.9	
CH09-13fs-4,1	50.99	0.17	2.28	11.44	0.23	12.10	21.63	0.46	-0.01	0.03	99.34	49.98	0.05	1.41	30.09	0.56	16.85	0.52	0.01	0.00	0.08	99.55	675.7	794.4	846.8	
CH09-13fs-4,2	50.48	0.22	2.40	11.86	0.23	11.77	21.50	0.46	-0.01	0.03	98.94	50.16	0.04	1.40	29.22	0.65	17.38	0.42	0.02	-0.03	0.02	99.28	711.2	829.1	844.2	
CH09-13fs-4,3	50.97	0.20	2.28	11.74	0.26	11.84	21.74	0.40	0.00	0.01	99.44	50.00	0.04	1.34	29.58	0.61	17.09	0.40	-0.03	0.00	0.02	99.04	704.1	828.0	831.7	
CH09-23fs-2,1	51.23	0.33	2.98	10.91	0.22	12.16	21.77	0.46	0.00	0.04	100.11	50.84	0.03	1.43	28.25	0.50	18.03	0.42	-0.03	-0.01	0.04	99.49	725.2	836.0	847.1	

(Continued)

Clinopyroxene Composition - in Weight Percent														Orthopyroxene Composition - in Weight Percent										Calculated Temperatures	
Sample Site, Pair	SiO2	TiO2	Al2O3	FeOt	MnO	MgO	CaO	Na2O	K2O	Cr2O3	Totals	SiO2	TiO2	Al2O3	FeOt	MnO	MgO	CaO	Na2O	K2O	Cr2O3	Totals	BK ^a 1990 T ^b 1998	P ^c 2008	
CH09-23fs 2,2	51.91	0.18	2.11	10.06	0.18	12.73	22.03	0.42	-0.01	0.05	99.66	50.53	0.07	1.54	28.11	0.51	18.22	0.37	-0.01	0.00	0.04	99.39	699.5	819.7	832.9
CH09-23fs 2,3	51.79	0.23	2.48	11.12	0.18	12.46	21.21	0.50	-0.02	0.09	100.04	51.12	0.03	1.39	28.34	0.54	18.58	0.40	0.00	-0.01	0.04	100.43	766.5	882.9	865.9
CH09-23fs 3,1	51.92	0.23	2.78	9.82	0.18	12.34	21.87	0.46	-0.02	0.15	99.73	50.92	0.02	1.43	28.02	0.48	18.49	0.38	0.00	-0.01	0.02	99.75	716.0	830.6	831.1
CH09-23fs 3,2	51.77	0.16	2.19	10.41	0.21	12.78	21.91	0.41	-0.01	0.11	99.94	50.97	0.01	1.40	28.37	0.58	18.20	0.39	0.01	-0.01	0.03	99.95	738.2	862.3	847.5
CH09-23fs 3,3	51.71	0.19	2.28	10.97	0.27	12.46	21.27	0.37	0.00	0.04	99.56	50.76	0.05	1.53	28.28	0.55	18.11	0.45	-0.01	-0.01	0.02	99.72	725.6	854.9	860.4
CH09-23fs 3,4	51.61	0.21	2.26	10.55	0.21	12.63	21.33	0.44	0.00	0.04	99.29	50.89	0.00	1.43	28.16	0.59	18.01	0.47	0.00	-0.01	0.04	99.57	750.2	880.0	853.6
CH09-23fs 4,1	51.93	0.20	2.53	10.35	0.10	12.60	21.73	0.47	-0.02	0.08	99.97	50.79	0.03	1.57	27.83	0.52	18.28	0.41	-0.04	0.00	0.06	99.44	730.9	853.7	843.8
CH09-23 4,1,5	51.80	0.21	2.44	10.37	0.23	12.64	21.66	0.53	-0.02	0.07	99.95	51.17	0.02	1.49	28.09	0.57	18.56	0.42	-0.02	-0.01	0.03	100.31	729.6	848.0	843.4
CH09-23fs 4,2	51.72	0.17	2.25	10.17	0.17	12.61	21.98	0.40	-0.02	0.11	99.57	51.36	0.04	1.38	27.80	0.51	18.15	0.42	-0.01	0.01	0.07	99.74	701.5	821.4	839.4
CH09-23fs 4,3	52.30	0.22	2.23	9.97	0.17	12.84	22.19	0.51	0.01	0.10	100.53	50.54	0.06	1.38	28.00	0.52	18.39	0.43	-0.02	0.00	0.05	99.34	700.6	822.4	829.3
CH09-23fs 4,4	51.25	0.20	2.58	10.59	0.21	12.55	21.41	0.50	0.01	0.10	99.40	51.15	0.02	1.38	27.97	0.51	18.52	0.40	-0.02	0.00	0.05	99.98	744.3	861.2	860.3
CH09-40fs 1,1	52.27	0.11	2.23	10.14	0.16	12.87	21.87	0.47	0.00	0.11	100.21	51.91	0.02	1.48	27.42	0.48	18.97	0.39	-0.01	-0.01	0.09	100.73	702.6	819.0	851.8
CH09-40fs 1,1	51.70	0.14	2.19	9.68	0.17	13.17	22.66	0.42	-0.01	0.11	100.22	51.08	0.03	1.52	27.48	0.53	18.68	0.44	0.00	0.00	0.05	99.81	664.1	777.0	834.5
CH09-40fs 1,2	51.11	0.19	2.35	10.58	0.20	12.70	21.99	0.45	0.01	0.13	99.72	50.43	0.06	1.53	27.62	0.56	18.63	0.45	0.03	0.00	0.01	99.30	708.4	821.7	855.5
CH09-40fs 1,2	51.21	0.24	2.35	10.09	0.16	12.65	22.04	0.42	0.00	0.11	99.27	50.86	0.00	1.22	27.60	0.53	18.72	0.39	0.03	-0.02	0.01	99.34	699.7	812.8	843.4
CH09-40fs 1,4	50.65	0.17	2.15	10.12	0.22	12.87	22.26	0.52	0.00	0.09	99.04	49.82	0.04	1.48	27.87	0.52	18.57	0.40	-0.01	-0.01	0.02	98.72	716.6	841.1	844.1
CH09-40fs 1,5	51.40	0.11	2.09	9.66	0.21	12.85	22.15	0.45	-0.01	0.10	99.01	50.83	0.02	1.43	27.29	0.51	18.90	0.44	0.00	0.00	0.01	99.43	680.8	796.9	833.0
CH09-40fs 2,1	51.13	0.18	2.43	10.26	0.24	12.95	22.23	0.49	0.01	0.06	99.99	50.79	0.02	1.40	27.84	0.55	18.52	0.41	-0.01	-0.02	-0.01	99.51	687.9	798.0	846.8
CH09-40fs 2,1	51.75	0.23	2.31	9.87	0.19	12.80	22.07	0.47	0.00	0.13	99.82	51.34	0.04	1.18	27.72	0.51	18.63	0.46	-0.01	-0.01	0.05	99.90	703.9	814.3	838.9
CH09-40fs 2,2	51.22	0.16	2.04	9.37	0.17	13.06	22.56	0.39	-0.01	0.13	99.10	50.97	0.03	1.28	27.32	0.52	19.32	0.42	-0.03	0.00	0.02	99.85	652.9	755.4	822.3
CH09-40fs 2,3	52.32	0.18	2.08	9.93	0.21	13.00	22.02	0.49	0.00	0.08	100.32	51.49	0.02	1.43	27.76	0.55	19.07	0.39	-0.04	0.00	0.00	100.68	718.3	836.1	835.3
CH09-40fs 2,3	51.94	0.17	2.21	9.84	0.17	12.65	22.06	0.48	0.01	0.09	99.64	50.79	0.03	1.38	27.79	0.50	18.85	0.33	-0.01	-0.02	0.06	99.70	696.6	810.4	826.6
CH09-40fs 2,4	51.25	0.20	2.24	10.22	0.23	13.12	22.26	0.53	-0.02	0.14	100.18	50.91	0.06	1.35	27.56	0.55	19.06	0.41	0.00	0.00	0.02	99.91	684.9	791.5	856.2
CH09-40fs 2,4	51.83	0.15	2.19	10.36	0.19	12.99	21.73	0.50	0.01	0.11	100.05	50.93	0.04	1.39	28.23	0.51	18.65	0.42	-0.03	0.00	0.03	100.18	732.6	852.6	856.5
CH09-40fs 3,1	51.65	0.16	1.95	9.76	0.18	12.95	22.65	0.43	-0.01	0.10	99.82	50.33	0.05	1.32	27.70	0.51	18.80	0.43	0.00	0.01	0.05	99.19	647.2	753.9	822.2
CH09-40fs 3,3	51.94	0.17	2.04	9.58	0.20	13.29	22.62	0.38	0.00	0.11	100.34	51.32	0.04	1.31	27.14	0.49	19.16	0.38	-0.04	0.00	0.03	99.83	676.8	791.9	834.2
CH09-40fs 3,4	51.44	0.18	2.36	9.71	0.18	12.99	22.19	0.50	0.01	0.06	99.62	50.68	0.03	1.24	27.48	0.53	19.15	0.35	-0.01	0.00	0.06	99.52	686.0	793.1	835.0
CH09-40fs 4,1	51.73	0.19	2.10	9.43	0.15	13.38	22.66	0.45	0.00	0.06	100.17	50.90	0.01	1.49	28.05	0.48	18.82	0.44	0.00	-0.01	0.05	100.22	657.0	769.5	836.2

(Continued)

Clinopyroxene Composition - in Weight Percent													Orthopyroxene Composition - in Weight Percent													Calculated Temperatures			
Sample Site, Pair	SiO2	TiO2	Al2O3	FeOt	MnO	MgO	CaO	Na2O	K2O	Cr2O3	Totals	SiO2	TiO2	Al2O3	FeOt	MnO	MgO	CaO	Na2O	K2O	Cr2O3	Totals	BK ^a 1990 T ^b 1998	P ^c 2008					
CH09-40fs 4,1	51.75	0.17	2.32	10.65	0.24	12.93	21.58	0.49	0.00	0.12	100.25	50.87	0.05	1.34	27.77	0.45	18.57	0.46	0.00	-0.02	0.06	99.56	749.7	871.8	875.3				
CH09-40fs 4,2	52.08	0.16	2.14	10.48	0.21	12.89	22.25	0.47	0.00	0.08	100.75	51.15	0.02	1.33	27.83	0.49	18.62	0.40	-0.01	-0.02	0.00	99.82	696.1	807.0	846.9				
CH09-40fs 4,3	51.19	0.15	2.18	10.17	0.19	12.76	21.86	0.45	-0.01	0.05	98.99	50.51	0.02	1.40	27.90	0.58	18.74	0.40	-0.03	-0.01	0.05	99.56	702.6	818.0	838.1				
CH09-40fs 4,4	51.53	0.20	2.12	9.38	0.20	13.31	22.75	0.43	-0.01	0.07	99.96	51.30	0.01	1.43	27.09	0.49	19.06	0.42	0.01	-0.01	0.07	99.88	650.3	755.1	834.9				
CH09-40fs 4,5	51.22	0.23	2.28	9.65	0.18	13.06	22.20	0.41	0.01	0.08	99.33	50.77	0.04	1.24	27.73	0.54	18.60	0.38	0.00	-0.02	0.00	99.28	690.5	801.8	840.5				
CH09-40fs 4,6	51.73	0.11	2.13	10.68	0.14	13.45	21.10	0.37	0.15	0.06	99.94	50.87	0.03	1.20	26.95	0.52	19.15	0.48	-0.01	0.00	0.04	99.23	799.5	927.6	894.7				
CH09-46fs 1,1	51.36	0.23	2.13	10.31	0.26	12.90	21.52	0.42	-0.01	0.05	99.16	50.83	0.04	1.39	26.96	0.53	19.09	0.37	0.00	0.00	0.07	99.26	749.8	866.7	862.4				
CH09-46fs 1,2	51.47	0.17	2.66	9.94	0.21	12.64	21.47	0.43	-0.01	0.12	99.09	50.70	0.04	1.46	27.21	0.45	18.80	0.39	-0.01	-0.02	0.03	99.07	750.7	868.3	858.5				
CH09-46fs 1,3	51.68	0.16	2.09	9.38	0.17	13.21	22.19	0.50	0.00	0.15	99.54	50.82	0.02	1.48	27.22	0.45	19.17	0.41	0.01	-0.01	0.05	99.62	685.7	800.5	846.2				
CH09-46fs 1,4	51.05	0.21	2.32	9.57	0.15	13.07	22.09	0.49	-0.01	0.10	99.05	50.18	0.04	1.52	26.89	0.43	19.28	0.41	0.02	0.01	0.06	98.83	692.0	799.1	854.2				
CH09-46fs 2,1	50.87	0.20	2.41	10.81	0.20	12.73	21.37	0.49	-0.01	0.12	99.18	50.98	0.03	1.21	26.96	0.52	19.43	0.37	0.00	0.00	0.06	99.56	754.8	859.8	875.0				
CH09-46fs 2,3	52.23	0.19	2.13	9.46	0.15	13.35	22.22	0.42	-0.01	0.15	100.30	50.91	0.04	1.39	27.29	0.51	18.68	0.44	0.01	-0.01	0.04	99.31	677.7	785.6	848.4				
CH09-46fs 2,4	51.46	0.25	2.30	9.95	0.17	13.00	21.83	0.43	-0.01	0.12	99.50	50.29	0.05	1.43	27.46	0.50	18.87	0.38	-0.02	-0.01	0.07	99.03	725.0	843.1	854.2				
CH09-46fs 4,1	51.58	0.21	2.13	9.90	0.15	12.97	22.07	0.43	0.00	0.06	99.51	51.38	0.02	1.26	27.25	0.46	18.46	0.77	0.04	0.00	0.03	99.66	706.1	820.7	858.6				
CH09-46fs 4,2	51.41	0.16	2.14	9.16	0.19	13.21	22.66	0.45	0.00	0.09	99.47	50.61	-0.01	1.49	27.52	0.49	18.88	0.37	-0.02	0.00	0.08	99.42	639.4	746.8	821.0				
CH09-55fs 1,1	51.88	0.15	2.19	11.14	0.26	12.46	22.03	0.45	-0.01	0.05	100.61	50.59	0.03	1.51	29.13	0.59	17.82	0.40	-0.02	0.00	0.01	100.05	715.6	843.2	837.3				
CH09-55fs 1,2	52.08	0.18	2.19	10.68	0.25	12.84	22.22	0.40	-0.02	0.07	100.89	50.48	0.02	1.49	29.28	0.59	17.81	0.37	-0.02	0.00	0.02	100.03	689.3	816.3	836.9				
CH09-55fs 1,3	52.08	0.16	2.31	10.87	0.17	12.59	22.11	0.48	-0.01	0.03	100.78	50.75	0.01	1.49	28.82	0.55	17.99	0.41	-0.01	0.00	-0.01	100.00	704.5	826.4	839.3				
CH09-55fs 1,4	51.40	0.15	2.21	10.28	0.21	12.83	22.46	0.40	0.01	0.05	99.99	50.32	0.04	1.47	28.40	0.61	17.99	0.46	0.02	0.00	0.00	99.33	670.9	789.2	831.8				
CH09-55fs 2,1	51.28	0.17	2.22	10.16	0.20	12.50	22.38	0.49	0.00	0.10	99.52	50.59	0.00	1.17	28.41	0.64	18.20	0.40	0.01	-0.01	-0.02	99.41	644.7	755.5	813.0				
CH09-55fs 2,2	50.52	0.25	2.37	11.23	0.21	12.41	21.96	0.49	-0.01	0.07	99.49	50.44	0.01	1.48	28.26	0.56	18.40	0.46	-0.02	0.02	0.01	99.61	693.6	798.3	854.9				
CH09-55fs 2,3	50.83	0.18	2.51	10.92	0.26	12.42	21.80	0.50	0.00	0.03	99.43	50.33	0.05	1.42	27.69	0.56	18.33	0.44	0.02	0.06	0.00	98.91	686.4	791.9	853.3				
CH09-55fs 2,4	52.22	0.18	2.51	11.22	0.21	12.15	21.60	0.52	-0.01	0.06	100.67	51.23	0.08	1.62	28.24	0.56	18.24	0.48	0.01	-0.01	0.04	100.49	758.2	881.3	847.7				
CH09-55fs 3,1	51.20	0.23	2.45	11.42	0.20	12.37	21.50	0.42	-0.02	0.06	99.84	50.57	0.05	1.52	27.87	0.60	18.30	0.41	0.03	0.00	0.05	99.38	748.6	867.8	865.6				
CH09-55fs 3,2	52.06	0.18	2.16	10.11	0.23	12.73	22.35	0.47	-0.01	0.07	100.34	50.56	0.05	1.50	28.54	0.61	18.05	0.39	-0.01	0.00	0.02	99.72	685.0	808.6	817.6				
CH09-55fs 3,3	51.78	0.18	2.47	10.82	0.22	12.15	21.88	0.48	0.00	0.09	100.08	50.29	0.04	1.50	28.77	0.62	17.66	0.44	0.00	-0.02	0.01	99.31	704.1	828.2	827.2				
CH09-68fs 1,1	51.28	0.25	2.74	10.01	0.19	12.31	22.34	0.44	-0.02	0.16	99.69	50.14	0.05	1.65	28.29	0.44	18.29	0.36	-0.04	-0.01	0.13	99.31	688.6	800.3	822.6				
CH09-68fs 1,2	50.79	0.20	2.52	10.43	0.16	12.37	21.93	0.47	-0.01	0.14	99.00	50.53	0.04	1.29	28.35	0.45	18.32	0.37	0.00	0.00	0.07	99.41	689.9	798.4	847.0				

(Continued)

Clinopyroxene Composition - in Weight Percent													Orthopyroxene Composition - in Weight Percent													Calculated Temperatures	
Sample Site, Pair	SiO ₂	TiO ₂	Al ₂ O ₃	FeO ^a	MnO	MgO	CaO	Na ₂ O	K ₂ O	Cr ₂ O ₃	Totals	SiO ₂	TiO ₂	Al ₂ O ₃	FeO ^a	MnO	MgO	CaO	Na ₂ O	K ₂ O	Cr ₂ O ₃	Totals	BK ^c 1990 T ^b 1998	P ^f 2008			
CH09-68fs 1,3	50.83	0.20	2.69	9.69	0.12	12.52	22.08	0.43	-0.01	0.24	98.79	50.86	0.03	1.11	28.38	0.41	18.21	0.41	-0.01	0.00	0.10	99.51	679.9	787.4	842.2		
CH09-68fs 3,1	51.03	0.18	2.39	10.09	0.18	12.79	22.05	0.43	-0.01	0.21	99.33	50.77	0.02	1.42	28.46	0.51	18.29	0.48	-0.02	0.00	0.08	100.00	696.1	814.1	849.3		
CH09-68fs 3,2	51.35	0.20	2.39	9.96	0.20	12.72	21.97	0.42	0.00	0.21	99.42	50.40	0.07	1.56	28.35	0.41	17.95	0.44	-0.03	-0.02	0.08	99.21	703.5	829.0	850.1		
CH09-68fs 3,4	50.87	0.19	2.43	10.32	0.18	12.46	22.37	0.45	0.01	0.15	99.43	50.27	0.08	1.63	28.10	0.43	18.41	0.42	-0.01	-0.01	0.07	99.40	657.9	766.5	838.1		
CH09-68fs 4,1	50.97	0.21	2.58	10.37	0.17	12.29	21.72	0.52	-0.01	0.23	99.04	51.38	0.02	1.39	27.78	0.41	18.63	0.37	-0.01	0.00	0.07	100.04	695.3	802.1	854.3		
CH09-68fs 4,2	51.35	0.22	2.46	10.03	0.18	12.76	22.23	0.41	0.00	0.18	99.81	50.63	0.05	1.52	28.16	0.48	18.23	0.38	-0.04	0.00	0.05	99.47	691.0	808.0	840.1		
CH09-68fs 4,4	51.40	0.17	2.33	10.04	0.17	12.42	22.17	0.49	-0.02	0.14	99.31	50.91	0.03	1.24	28.51	0.42	18.67	0.43	0.00	-0.01	0.08	100.29	703.2	818.9	830.9		






^aBrey and Kohler (1990), ^bTaylor (1998), ^cPutirka (2008)

Appendix G.

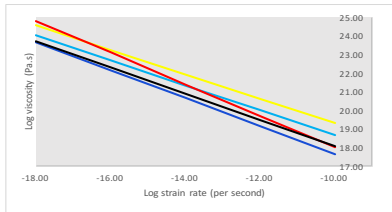
Polyphase Rheology Graphs Calculated through the Mixing Model

Polyphase rheology (black dashed line) plotted against
monophase quartz, plagioclase feldspar, enstatite, and
diopside for all samples

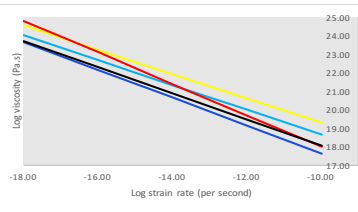
Key:

-  Quartz
-  Plagioclase Feldspar
-  Enstatite
-  Diopside
-  Polyphase Sample

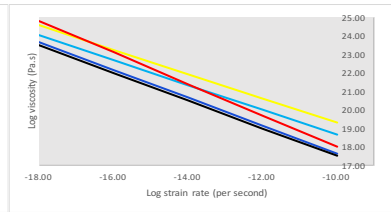
AF09-3A



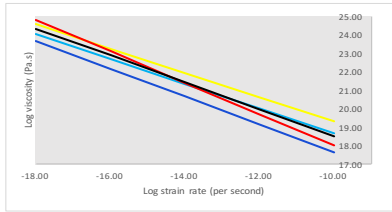
AF09-12



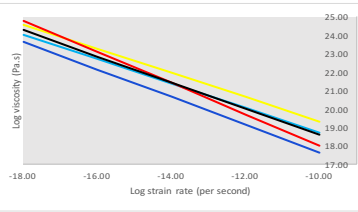
AF09-15



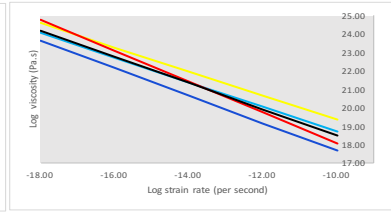
AF09-19



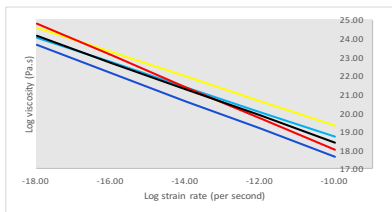
CH09-08A



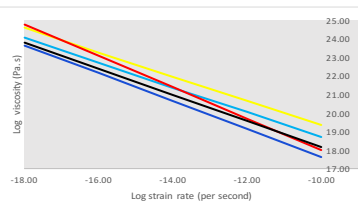
CH09-08B



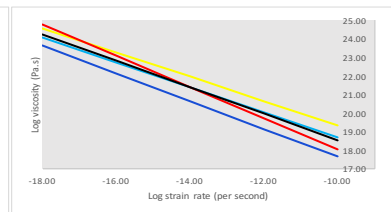
CH09-08C



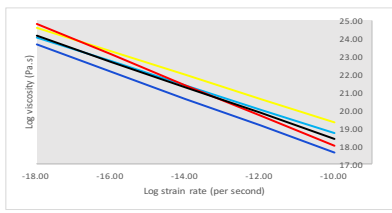
CH09-09A



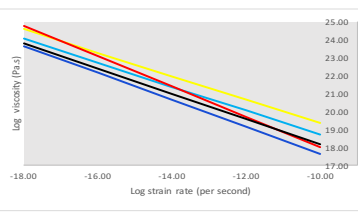
CH09-09B



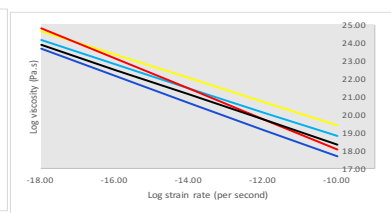
CH09-11ch



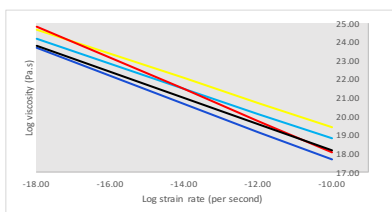
CH09-11fs



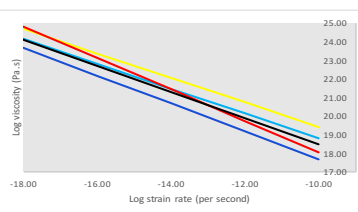
CH09-13ch-1



CH09-13ch-2



CH09-13fs



CH09-16ch

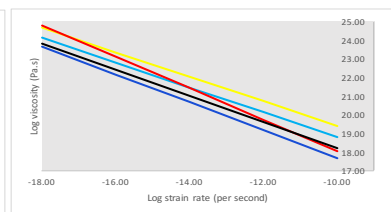







Figure 1 is a log-log plot showing the dependence of Log viscosity (Pa.s) on Log strain rate (per second) for four different temperatures. The x-axis ranges from -18.00 to -10.00, and the y-axis ranges from 17.00 to 25.00. Four lines are plotted, each representing a different temperature, showing a linear decrease in log viscosity with increasing log strain rate.

Appendix H.

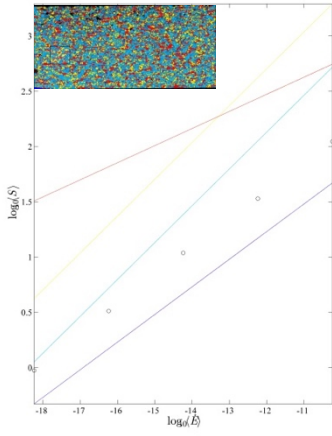
Polyphase Rheology Graphs Generated through the PLC Toolbox

Maps of selected sub-regions chosen for analysis and corresponding graphs of polyphase rheology (black dashed line) plotted against monophase quartz, plagioclase feldspar, enstatite, and diopside for all samples

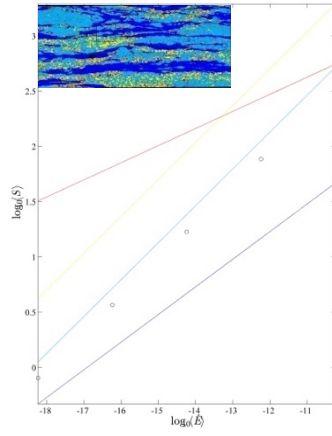
Key:

	Quartz
	Plagioclase Feldspar
	Enstatite
	Diopside
	Polyphase Sample

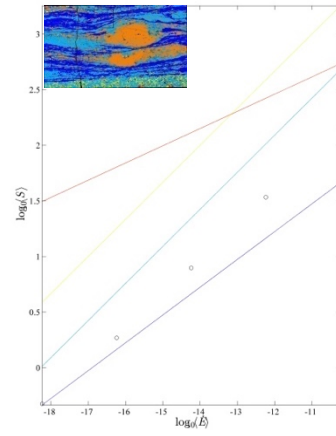
CH09-08A:



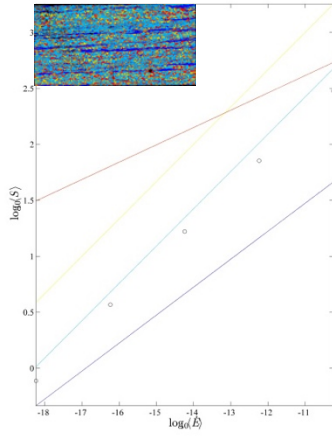
CH09-09A:



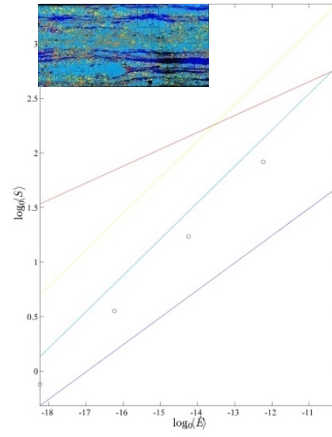
CH09-11ch:



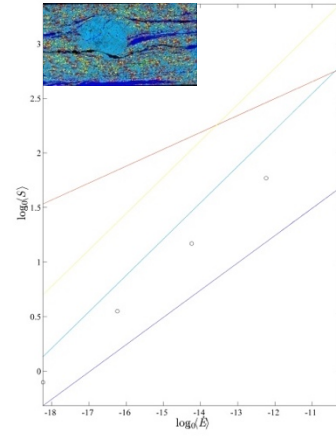
CH09-11fs:



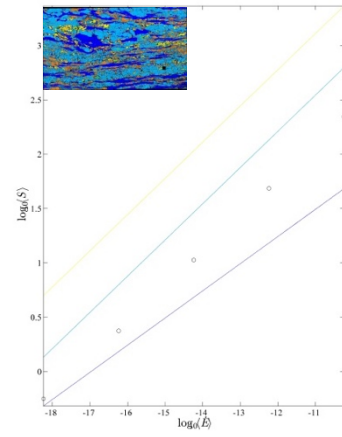
CH09-13ch-1:



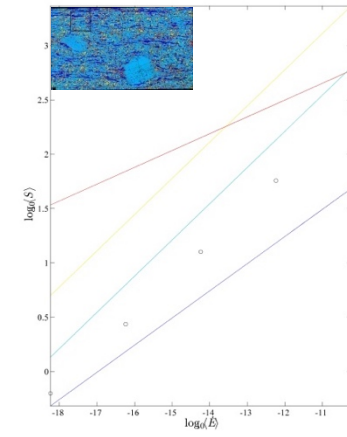
CH09-13fs:



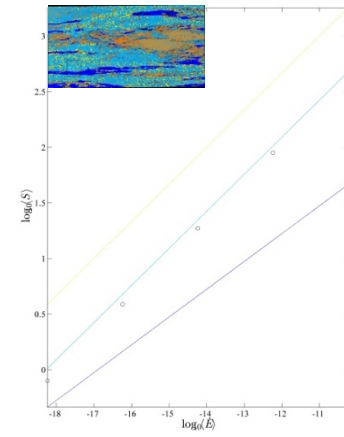
CH09-16ch:



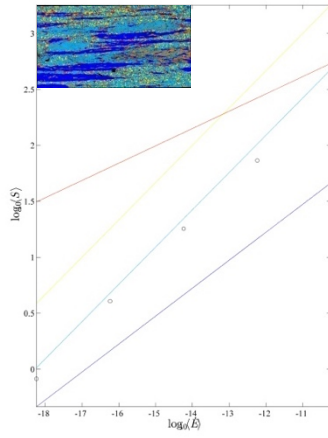
CH09-16fs:



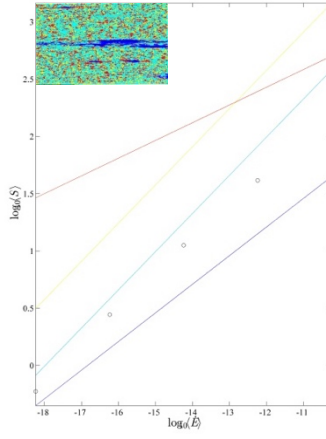
CH09-19ch-1:



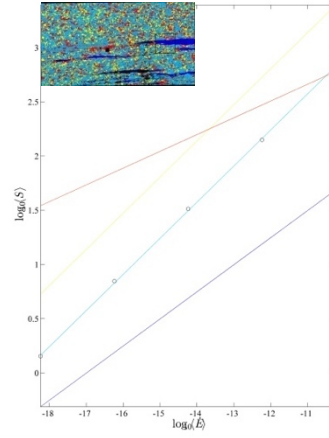
CH09-19fs:



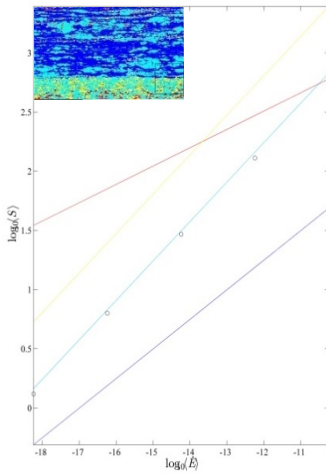
CH09-23fs:



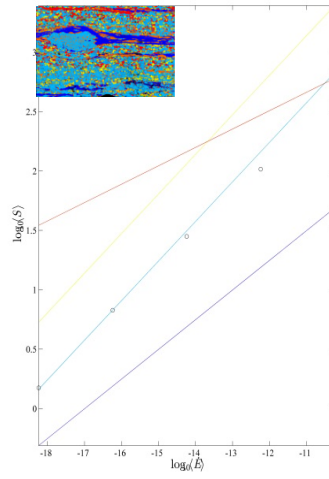
CH09-40fs:



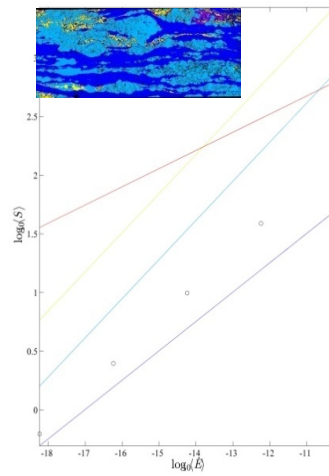
CH09-41ch:



CH09-41fs:



CH09-68ch:



CH09-68fs:

